REPORT DOCUMENTATION PAGE

Form Approved OMB NO. 0704-0188

1. REPORT DATE (DD-MM-YYYY)	2. REPORT TYPE	3. DATES COVERED (From - To)
29-03-2011	Final Report	19-Jul-2006 - 31-Dec-2010

4. TITLE AND SUBTITLE

FIB and CVD Fabrication of Carbon Nanostructures on Diamond and Quartz Substrates

5a. CONTRACT NUMBER
W911NF-06-1-0302

5b. GRANT NUMBER

5c. PROGRAM ELEMENT NUMBER
611102

6. AUTHORS

Dr. Alexandre M. Zaitsev, Dr. Alexander Umantsev, Dr. Anshel A. Gorokhovsky, Vivek Kumar, Searhei Samsonau, Alexandra Bergman, Yuri A. Dziashko, Dr. Zinovy Akkerman

5d. PROJECT NUMBER

5e. TASK NUMBER

5f. WORK UNIT NUMBER

7. PERFORMING ORGANIZATION NAMES AND ADDRESSES

CUNY - College of Staten Island
230 West 41st St.

New York, NY 10036 -

8. PERFORMING ORGANIZATION REPORT NUMBER

9. SPONSORING/MONITORING AGENCY NAME(S) AND ADDRESS(ES)

U.S. Army Research Office
P.O. Box 12211
Research Triangle Park, NC 27709-2211

10. SPONSOR/MONITOR'S ACRONYM(S)
ARO

11. SPONSOR/MONITOR'S REPORT NUMBER(S)
49658-EL-H.3

12. DISTRIBUTION AVAILIBILITY STATEMENT

Approved for Public Release; Distribution Unlimited

13. SUPPLEMENTARY NOTES

The views, opinions and/or findings contained in this report are those of the author(s) and should not contrued as an official Department of the Army position, policy or decision, unless so designated by other documentation.

14. ABSTRACT

Electronic carbon nanostructures have been fabricated on diamond substrates by focused ion beam (FIB) irradiation. Fabrication of planar nanowire/nanodot structures at a scale below 10 nm (e.g. all-carbon single electron transistor with island size of 7 nm) has been shown. FIB-written carbon nanostructures may reveal non-linear conductivity, current injection trough insulating diamond, bistability of current flow, and coulomb blockade at room temperature. Also we developed methods of fabrication of large uniform areas of amorphous

15. SUBJECT TERMS

Focused ion beam, Carbon, Nanostructures, Diamond, Graphene, Chemical sensitivity, Two-dimensional nucleation, Escape time, Chemical vapor deposition, Computer simulation

16. SECURITY CLASSIFICATION OF:			17. LIMITATION OF ABSTRACT	15. NUMBER OF PAGES	19a. NAME OF RESPONSIBLE PERSON
a. REPORT	b. ABSTRACT	c. THIS PAGE			Alexandre Zaitsev
UU	UU	UU	UU		19b. TELEPHONE NUMBER 718-982-2812

Report Title

FIB and CVD Fabrication of Carbon Nanostructures on Diamond and Quartz Substrates

ABSTRACT

Electronic carbon nanostructures have been fabricated on diamond substrates by focused ion beam (FIB) irradiation. Fabrication of planar nanowire/nanodot structures at a scale below 10 nm (e.g. all-carbon single electron transistor with island size of 7 nm) has been shown. FIB-written carbon nanostructures may reveal non-linear conductivity, current injection trough insulating diamond, bistability of current flow, and coulomb blockade at room temperature. Also we developed methods of fabrication of large uniform areas of amorphous carbon and/or graphene films on diamond and quartz substrates using combination of graphitization/CVD deposition/plasma etching processes. Arrays of carbon nanowires/nanodots, amorphous carbon films on diamond and graphene films on quartz have been shown to possess remarkable electronic properties and selective chemical sensitivity. A model of continuum carbon phase transitions has been developed to explain the experimental data. The problem of two-dimensional (2D) nucleation has been approached theoretically using the concept of escape time (phase-transition time) and direct computer simulations. It is shown that the transition state of graphite/diamond phase system gains thermodynamic stability in a closed nano-volume and, in case of 2D nucleation, there is a critical thickness above which the growing layer manifests the stable phase.

List of papers submitted or published that acknowledge ARO support during this reporting period. List the papers, including journal references, in the following categories:

(a) Papers published in peer-reviewed journals (N/A for none)

15. V. Kumar, A. A. Bergman, A. A. Gorokhovsky, A. M. Zaitsev, "Formation of carbon nanofilms on diamond for all-carbon based temperature and chemical sensor application", Carbon 2011; 49(4):1385-1394.
14. A. Umantsev and Z. Akkerman, “Continuum theory of carbon phases”, Carbon, 48 (2010) 8.
13. A. Umantsev, “Thermodynamic Stability of Transition States in Nanosystems”, J. Stat. Phys. 136 (2009) 117.
12. I. A. Dobrinets, A. M. Zaitsev, "Fluorescence Cage - Visual Identification of HPHT-treated Diamonds", Gems and Gemology, Fall 2009, 186-190.
11. A. Bergman, A.M. Zaitsev, Mengbing Huang, A.A. Gorokhovsky, “Photoluminescence and Raman studies of Xe ion - implanted diamonds: dependence on implantation dose.” J. of Luminescence, 129 (2009) 1524-1526.
10. A. Umantsev and Z. Akkerman, “Continuum theory of amorphous carbon nanostructures”, IEEE Sensors Journal, 8 (2008) 1041.
9. A. M. Zaitsev, "On the way to mass-scale production of perfect bulk diamonds", Proceedings of the National Academy of Sciences, 105 (2008) 17591-17592.
8. B. Deljanin, D. Simic, A. M. Zaitsev, M. Epelboym, J. Chapman, I. A. Dobrinets, A. Wideman, N. Del Re, E. Deljanin, T. Midletton, A. De Stefano, "Characterization of Pink Diamonds of Different Origin: Natural from Argyle, Irradiated, HPHT treated, Treated with multi-process, Coated and Synthetic", "Diamond and Related Materials", Vol. 17, (2008) 1169-1178.
7. A. M. Zaitsev, A. M. Levine, S. H. Zaidi, "Temperature and Chemical Sensors Based on FIB-Written Carbon Nanowires", "IEEE Sensors Journal", Vol. 8, (2008) 849-856.
6. A. Umantsev, “Modeling of intermediate phase growth”, J. Appl. Phys. 101 (2007) 024910.
5. A. Umantsev, “Identification of material parameters for modeling of phase transformations”, Phys. Rev. B 75 (2007) 024202.
4. A. Umantsev, “Thermal Effects in Phase Transformations: A General Approach”, MRS Proceedings, (2007) 979-HH02-01.
3. A. Umantsev, “Thermal Effects in Phase Transformations: A review”, Physica D, 235 (2007) 1.
2. A. M. Zaitsev, A. M. Levine, S. H. Zaidi, "Carbon Nanowire-Based Temperature Sensor", Physica Status Solidi (a), 204 (2007) 3574-3579.
1. A. A. Bergman, A. M. Zaitsev, A. A. Gorokhovsky, "Polarization of Luminescence and Symmetry of the Xe Center in Diamond", J. of Luminescence, Vol. 125 (2007) 92-96.

Number of Papers published in peer-reviewed journals: 15.00

(b) Papers published in non-peer-reviewed journals or in conference proceedings (N/A for none)

Number of Papers published in non peer-reviewed journals: 0.00

(c) Presentations

32. S. V. Samsonau, Y. Deshko, A.A. Gorokhovsky, A.M. Zaitsev, “Graphene Films Grown on Insulating Substrates”, APS March Meeting 2011

31. I. A. Dobrinets, A. M. Zaitsev, “Recognition of HPHT treated Diamonds”, Proceedings of the Diamond Conference 2010, Warwick, 10-14 Jily 2010, p. 25-1 – 25-4

30. V. Kumar, S. V. Samsonau, A. M. Zaitsev, „Chemical Sensitivity of Carbon Nanofilms on Diamond and Quartz“,Proceedings of the Diamond Conference 2010, Warwick, 10-14 Jily 2010, p. 21-1 – 21-3.

29. A. Umantsev, “Field-Theoretic Approach to Nanostructures”
“Heterogeneous Nucleation and Microstructure Formation” International Summer School, University of Bayreuth, Germany, 2010

28. S. Samsonau, A. M. Zaitsev, "Carbon Nanofilms on Insulating Substrates for Electronic Applications", Gotham-Metro Condensed Matter Meeting, Spring 2010

27. S. V. Samsonau, A. L. Exarhos, M. E. Turk, J. Cai, J. M. Kikkawa, Y. Deshko, A.A. Gorokhovsky, A.M. Zaitsev, “Graphene Films Grown on Insulating Substrates, Meeting “Electronic Properties of Graphene: 2010", Princeton Center for Theoretical Science

26. S. V. Samsonau, A. L. Exarhos, M. E. Turk, J. Cai, J. M. Kikkawa, Y. Deshko, A.A. Gorokhovsky, A.M. Zaitsev, Graphene Films Grown on Insulating Substrates’, Gotham-Metro Condensed Matter Meeting, New York, Fall 2010

25. V. Kumar, A. A. Bergman, A. A. Gorokhovsky, A. M. Zaitsev, "Temperature and chemical sensors based on carbon nanofilms", ACS National Meeting, Fall 2010

24. A. Umantsev, Telluride Science Research Center, Telluride, Colorado, July 1, 2010

23. Nasdala, L., Grambole, D., Wildner, M., Zaitsev, A., Goetze, J., Kempe, U., Hanchar, J.M. "Radiation-induced defect centers: Luminescence and optical absorption study of helium-irradiated diamond and zircon." The AGU Joint Assembly, Toronto, Canada, May, 2009

22. A. Umantsev, Fall Meeting of the Materials Research Society, Boston MA, December 1, 2009

21. A. Umantsev, “Continuum Theory of Carbon Phases”
Computational Materials Science Network, “Dynamics and Cohesion of Materials Interfaces and Confined Phases under Stress”, Sixth Project Coordination Meeting, George Mason University, VA, 2009

20. V. Kumar, A. A. Bergman, A. A. Gorokhovsky, A. M. Zaitsev, "Carbon nanofilms on diamond for sensor applications", NanoDDS, Fall 2009

19. V. Kumar, A. A. Bergman, A. A. Gorokhovsky, A. M. Zaitsev, "Temperature and chemical sensors based on carbon nanofilms", GMCMM, New York Academy of Sciences. 2009.

18. A. Umantsev, “Continuum Method of Simulation of Phase Transformations in Materials”, Thirty-third Annual Meeting of Society of Industrial and Applied Mathematics Southeast Atlantic Section University of South Carolina, Columbia, SC, 2009

17. A. Bergman, A. M. Zaitsev, M. Huang, A. Gorokhovsky, "Light emitting diodes on ion - implanted diamond for sensing applications", platform presentation at The 2008 International Symposium on Spectral Sensing Research (ISSSR-2008), Hoboken, NJ, June 23-28, 2008

16. A. M. Zaitsev "Carbon Nanostructures Made by Focused Ion Beams on Carbonaceous Substrates", The 40th Middle Atlantic Regional Meeting (MARM), May 17–21, 2008, Bayside, NY.

15. L. Nasdala, A.M. GiglerI, M. Wildner, D. Grambole, A.M. Zaitsev, J.W. Harris, W. Hofmeister, H.J. Milledge, S. Satitkune, "Alpha-radiation damage in diamond", Goldschmidt 2008 - Annual Meeting on Geochemistry, July 13 - 18 in Vancouver, Canada

14. A. Umantsev, “Thermal Effects of Phase Transformations:

Connections to Biology and Medicine" "Phasefield-Simulations: Materials Science meets Biology and Medicine" Max Planck Institute for the Physics of Complex Systems, Dresden, Germany, 2008

13. A. M. Zaitsev, "Optical spectroscopy of diamond", Annual Research Workshop and PhD student course "Emission and absorption spectrosocopy: Basics and applications in the Earth sciences", Institute of Mineralogy and Crystallography, University of Vienna, Austria, March 3, 2008.

12. V. Kumar, "Polymeric solar cells", Graduate Center, The City University of New York, Summer 2008

11. V. Kumar, "Photocatalytic activity of titanium oxide", The City University of New York, Spring 2008

10. A. Umantsev, "Thermodynamic Stability of Transition States"
Computational Materials Science Network Princeton University, NJ, 2008

9. A. Umantsev, "Continuum Theory of Amorphous Carbon Nanostructures"
College of Staten Island, CU New York, 2008

8. A. M. Zaitsev, A. M. Levine, S. H. Zaidi, "Temperature Sensor Based on FIB-written Carbon Nanowires", 2007 Nanoelectronic Devices for Defense and Security (NANO-DDS), accepted as a "Platform Presentation", Crystal City, Virginia, 18-21 June 2007.

7. S. H. Zaidi, A. M. Zaitsev, "Characterization of a Diamond-based Nanowire Temperature Sensor", - 22nd International Congress on Instrumentation in Aerospace Simulation Facilities, June 10 – 14th 2007, Asilomar Conference Center, Pacific Grove, California.

6. A. M. Zaitsev, A. M. Levine, I. Zilberman, M. Natenzon, S. H. Zaidi, "Design and Development of a Diamond-based Nanowire Temperature Sensor ", 45th Aerospace, Sciences Meeting and Exhibit, Reno, Nevada, 8 - 11 Jan 2007, AIAA-2007-1265

5. A. Umantsev, "Thermal Effects in Phase Transformations"
Institute for Material Physics in Space, German Research Laboratory (DLR, 2007

4. A. Umantsev, "Modeling Intermetallic Phase Growth"
EuroMat 2007, September 10-13, Nuremberg, Germany, 2007

3. A. Umantsev, "Mathematical Modeling of Soldering Reaction"
Annual Meeting of the Computational Materials Science Network, New York, NY, 2007

2. A. Umantsev, EuroMat 2007, September 10-13, Nuremberg, Germany, September 12, 2007

1. A. Umantsev, 2007 NANO-DDS, Washington, DC, June 21, 2007

Number of Presentations: 32.00

Non Peer-Reviewed Conference Proceeding publications (other than abstracts):

Number of Non Peer-Reviewed Conference Proceeding publications (other than abstracts): 0

Peer-Reviewed Conference Proceeding publications (other than abstracts):

Number of Peer-Reviewed Conference Proceeding publications (other than abstracts): 0

(d) Manuscripts

1. S.V. Samsonau *,1, A.A. Gorokhovsky et al. 1, A.M. Zaitsev, "Graphene films grown on insulating substrates", submitted to Rapid Research Letters, Phys. Stat. Sol. 2011.

2. A. Umantsev, "FIELD THEORETIC METHOD IN PHASE TRANSFORMATIONS", Springer-Verlag, Lecture Notes in Physics, 2011.

Number of Manuscripts: 2.00

Patents Submitted

Patents Awarded

Awards

A. Umantsev, Advisory Board Service Recognition Award, Engineering Academy, Jack Britt High School, 2009

A. Umantsev, STEM Undergraduate Research Program Award, Fayetteville State University, April 26, 2008

Graduate Students

NAME	PERCENT_SUPPORTED
Vivek Kumar	0.50
Searhei Samsonau	0.50
Alexandra Bergman	0.50
Yuri Dziashko	0.20
FTE Equivalent:	**1.70**
Total Number:	**4**

Names of Post Doctorates

NAME	PERCENT_SUPPORTED
Zinovy Akkerman	0.20
FTE Equivalent:	**0.20**
Total Number:	**1**

Names of Faculty Supported

NAME	PERCENT_SUPPORTED	National Academy Member
Alexander Zaitsev	0.20	No
Alexander Umantsev	0.20	No
Anshel Gorokhovsky	0.10	No
FTE Equivalent:	**0.50**	
Total Number:	**3**	

Names of Under Graduate students supported

NAME	PERCENT_SUPPORTED
Igor Zilberman	
Ajda Oziurt	
Mike Natenzon	
Mohammad Durrani	
Thomas Jose	
Sia Gocheva	
Walter Smith	0.10
Brandon Kizer	0.10
FTE Equivalent:	**0.20**
Total Number:	**8**

Student Metrics

This section only applies to graduating undergraduates supported by this agreement in this reporting period

The number of undergraduates funded by this agreement who graduated during this period:	6.00
The number of undergraduates funded by this agreement who graduated during this period with a degree in science, mathematics, engineering, or technology fields:.....	7.00
The number of undergraduates funded by your agreement who graduated during this period and will continue to pursue a graduate or Ph.D. degree in science, mathematics, engineering, or technology fields:.....	6.00
Number of graduating undergraduates who achieved a 3.5 GPA to 4.0 (4.0 max scale):	4.00
Number of graduating undergraduates funded by a DoD funded Center of Excellence grant for Education, Research and Engineering:	0.00
The number of undergraduates funded by your agreement who graduated during this period and intend to work for the Department of Defense	2.00
The number of undergraduates funded by your agreement who graduated during this period and will receive scholarships or fellowships for further studies in science, mathematics, engineering or technology fields:	0.00

Names of Personnel receiving masters degrees

NAME

Total Number:

Names of personnel receiving PHDs

NAME

Total Number:

Names of other research staff

NAME	PERCENT_SUPPORTED

FTE Equivalent:

Total Number:

Sub Contractors (DD882)

Inventions (DD882)

5 **Method of Production of Carbon Films**

Patent Filed in US? (5d-1) Y

Patent Filed in Foreign Countries? (5d-2) N

Was the assignment forwarded to the contracting officer? (5e) N

Foreign Countries of application (5g-2):

5a: A. M. Zaitsev

5f-1a: College of Staten Island

5f-c: 2800 Victory Blvd.

Staten Island NY 10314

5a: S. Samsonau

5f-1a: College of Staten Island

5f-c: 2800 Victory Blvd.

Staten Island NY 10314

5 **Temperature and Chemical Sensors Based on Focused Ion Beam (FIB) – Written Carbon Nanowires**

Patent Filed in US? (5d-1) Y

Patent Filed in Foreign Countries? (5d-2) N

Was the assignment forwarded to the contracting officer? (5e) N

Foreign Countries of application (5g-2):

5a: A. M. Zaitsev

5f-1a: College of Staten Island

5f-c: 2800 Victory Blvd.

Staten Island NY 10314

Scientific Progress

Technology Transfer

FIB and CVD Fabrication of Carbon Nanostructures on Diamond and Quartz Substrates

Final report

Proposal # 49658-EL-H, Agreement # W911NF-06-1-0302 (CUNY RF #47145-00-01)

PI: Dr. Alexandre M. Zaitsev (College of Staten Island of the City University of New York)

Co-PI: Dr. Alexander Umantsev (Fayetteville State University)

Other participants: Dr. Anshel A. Gorokhovsky (CSI), Dr. Zinovy Akkerman (FSU)
Vivek Kumar (CSI),Searhei Samsonau (CSI), Alexandra Bergman (CSI),
Yuri. A. Dziashko (CSI)

March, 2011

Abstract

Electronic carbon nanostructures have been fabricated on diamond substrates by focused ion beam (FIB) irradiation. Fabrication of planar nanowire/nanodot structures at a scale below 10 nm (e.g. all-carbon single electron transistor with island size of 7 nm) has been shown. FIB-written carbon nanostructures may reveal non-linear conductivity, current injection trough insulating diamond, bistability of current flow, and coulomb blockade at room temperature. Also we developed methods of fabrication of large uniform areas of amorphous carbon and/or graphene films on diamond and quartz substrates using combination of graphitization/CVD deposition/plasma etching processes. Arrays of carbon nanowires/nanodots, amorphous carbon films on diamond and graphene films on quartz have been shown to possess remarkable electronic properties and selective chemical sensitivity. A model of continuum carbon phase transitions has been developed to explain the experimental data. The problem of two-dimensional (2D) nucleation has been approached theoretically using the concept of escape time (phase-transition time) and direct computer simulations. It is shown that the transition state of graphite/diamond phase system gains thermodynamic stability in a closed nano-volume and, in case of 2D nucleation, there is a critical thickness above which the growing layer manifests the stable phase.

Key words:

Focused ion beam, Carbon, Nanostructures, Diamond, Graphene, Chemical sensitivity, Two-dimensional nucleation, Escape time, Chemical vapor deposition, Computer simulations

PART I, EXPERIMENTAL

I.1. FIB-Written Carbon Nanostructures

I.1.1 Introduction

It is known that the ion irradiation at doses exceeding a certain amorphization threshold converts many carbonaceous materials into amorphous carbon, which may possess relatively high electrical conductance. This effect is especially pronounced in diamond which, when in pristine state, is a highly insulating material. The dose threshold of conversion of diamond into amorphous carbon is very sharp. Therefore, the interface between the conductive ion-amorphized carbon and the insulating non-amorphized diamond is sharp too and, when the ion irradiation is performed with a well focused ion beam, may be as narrow as a few nanometers. Thus, using an ion beam focused at nanoscale, there is opportunity to make well-defined conductive carbon nanostructures (e.g. nanowires and nanodots) on insulating diamond substrates.

The present report gives the account on systematic studies of electronic properties of the FIB-written carbon nanostructures on diamond substrates. It has been shown that the current flow in the FIB-written nanostructures is essentially non-linear and strongly affected by the effects of charge carrier injection, bistability and coulomb blockade. As such the FIB-written carbon nanostructures may be used as switching nanoelectronic devices and nanosensors.

I.1.2. Experimental

Highly polished polycrystalline CVD diamond films (optical grade, according to the classification of CVD diamond materials used by the company Element6) and single crystal free standing CVD diamond films (optical grade) were used as the carbonaceous substrates in this research. All diamond samples were of type IIa with the nitrogen content in the 1 ppm range.

Carbon nanowire and nanodot structures were fabricated at room temperature using Micrion 2500 Focused Ion Beam System providing a 30 keV Ga^+ ion beam in a vacuum of about 8×10^{-8} mbar (Fig. 1.1). The ion beam current during the fabrication (irradiation) of the nanostructures may vary in the range from 10 pA to 1 nA depending on the irradiation dose and the size of the nanostructures. The ion beam writing of the structures was performed with the ion doses in the range from 10^{13} to 10^{17} ion/cm^2.

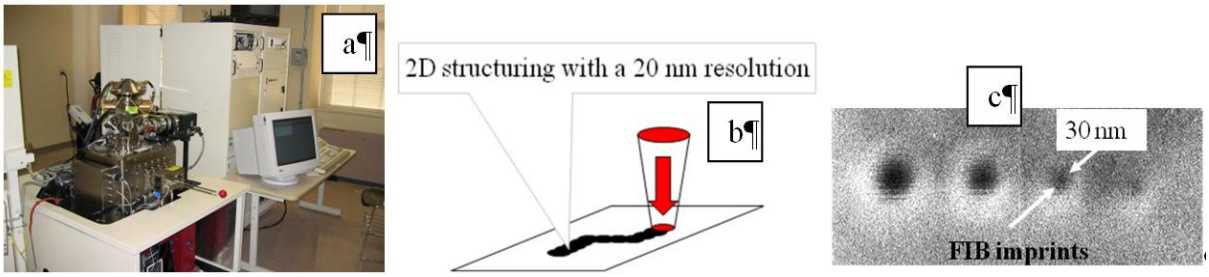

Fig. 1.1. (a) Micrion 2500 FIB instrument used for ion beam writing of carbon nanostructures on diamonds substrates. (b) Principle of FIB-writing of conductive carbon nanostructures on insulating diamond surface. The size of the conductive area primarily depends on the diameter of the ion beam focused on the diamond surface. (c) Imprints left by

a 30 keV, 10 pA focused ion beam on diamond surface after exposure for 30, 15, 5 and 0.5 seconds. Size of the amorphized area strongly increases with the exposure time.

After the ion irradiation and the measurements of the structures in the as-irradiated state the samples were annealed to convert the radiation-induced amorphous carbon into graphite. The annealing was performed at temperatures from 300 to 1400°C in a vacuum of 10^{-5} mbar for 10 min at each annealing step in a home-made all-graphite furnace purposely designed for contamination-free high temperature treatment of carbon materials (Fig. 1.2a).

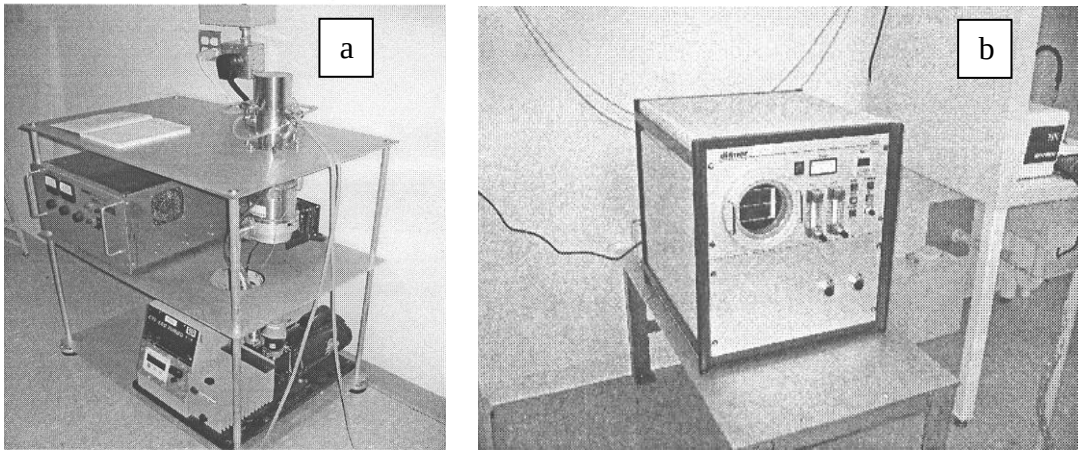

Fig. 1.2. (a) High temperature all-graphite vacuum furnace installed in CSI/CUNY. (b) Plasma System PICO-UHP-RF installed in CSI/CUNY.

Cleaning of the substrates and removal of the surface graphitization after high temperature annealing was performed by combination of plasma treatments in oxygen, argon and water vapor using PICO-UHP-RF Plasma System with a chamber 05-04-27 SP (Fig. 1.2b).

The plasma etching has been found to very effective method of cleaning of the as-irradiated and annealed carbon nanostructures on diamond substrates. Usually a few minutes etch at a pressure of 0.2 mbar and RF power 50 W was enough to completely remove any conductive contaminations from the diamond surface. In some cases, the annealed samples were cleaned by heating at a temperature of 300°C in oxygen-containing atmosphere. In Fig. 1.3) one can see the rate of the removal of the conductive layer by heating of diamond in dry air.

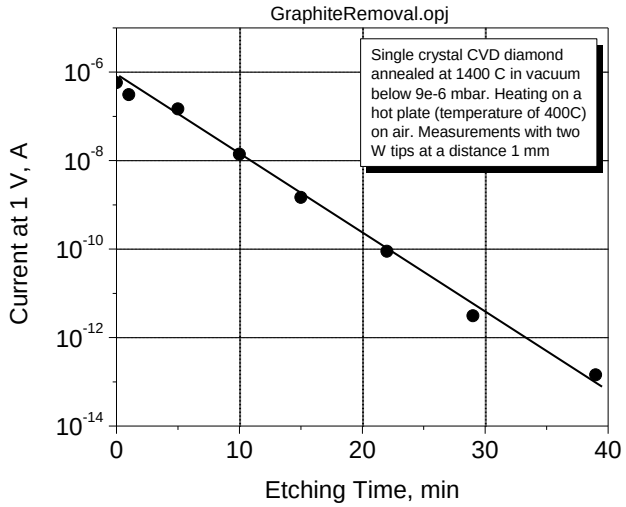

Fig. 1.3. Reduction of surface conduction of a single crystal CVD diamond Film annealed at 1400°C in vacuum below 9×10^{-6} mbar during heating on a hot plate (temperature of 300°C) in dry air. Measurements with two tungsten tips placed at a distance of 1 mm.

Scanning focused ion beam over diamond surface in a controlled way one can create patterns with high optical (transparent diamond versus opaque amorphous carbon) and/or electrical contrast (insulating diamond versus conductive amorphous carbon) and fabricate this way optical and/or electronic micro/nano structures (Fig. 1.4).

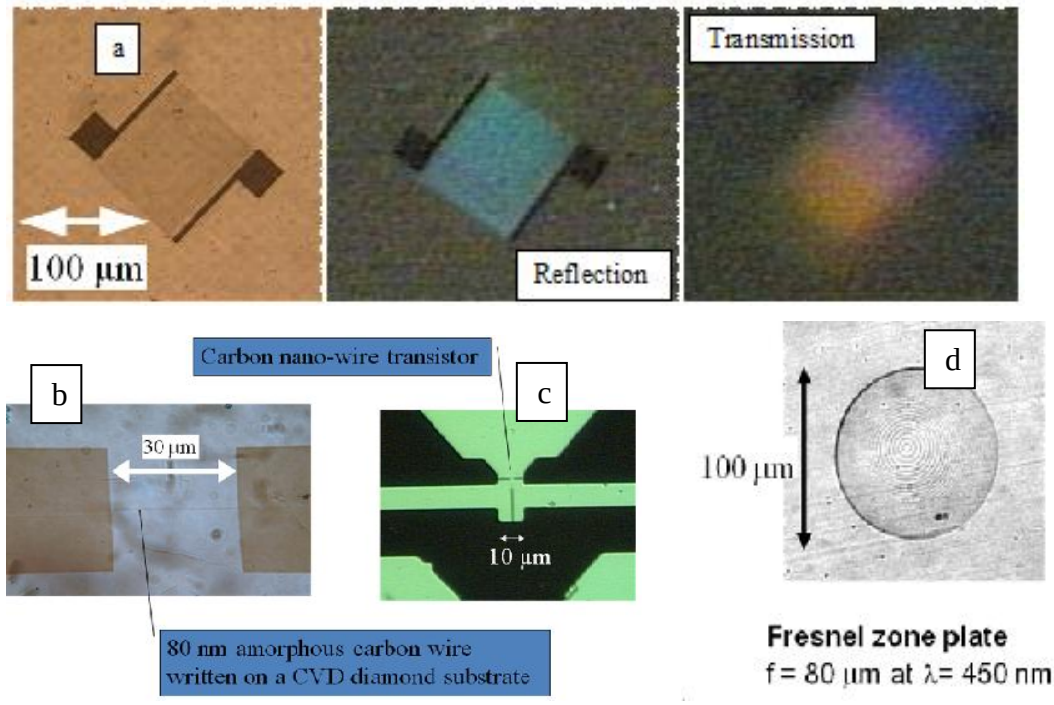

Fig. 1.4. Examples of nano/micro structures made on diamond surface by focused ion beam: (a) Diffraction micrograting made of carbon nanowires. Diffraction of light on the grating is shown in regimes of reflection and transmission; (b) Conductive carbon nanovire

drawn between two contact pads; (c) Carbon nanowire transistor made of three nanowires; (d) Asymmetric Fresnel microlens.

Electrical measurements of the FIB-written structures were performed using a micromanipulator setup equipped with a miniature hot plate (temperature measurements and control via a controller with a K-type thermocouple) and Keithley-237 or Keithley-4200-SCS source-measurement instruments. To provide electrical connections to the structures, tungsten tips were directly applied to the FIB-irradiated contact pads. In some cases macroscopic contacts of conductive silver paint were put on the edges of the FIB-written structures. The silver paint contacts were mostly used for the measurements of the 0.5×0.5 mm^2 nanowire arrays (see below).

Raman measurements of the carbon nanowire structures were performed at room temperature using a confocal micro-Raman spectrometer Jobin-Yvon T 64000 installed in CSI/CUNY. The Raman spectra were taken with Ar laser excitation at wavelength 488 nm. The power of the laser beam on the sample surface did not exceed 5 mW.

I.1.3. Electrical Measurements

I.1.3.1 Single Nanowire Structures

Electrical properties of FIB-written carbon nanowires were studied on the single nanowire structures shown in Fig. 1.5.

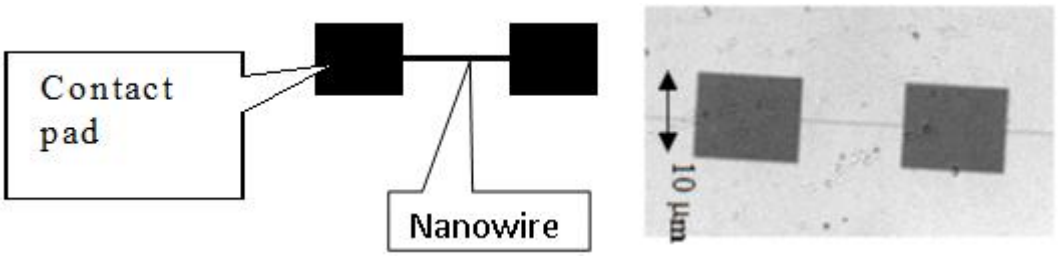

Fig. 1.5. Scheme of single nanowire structures and optical microscopy image of one of the structures. The nanowire width is of 80 nm.

Every single nanowire structure comprised individual nanowire made by linear scan of the focused ion beam and two contact pads made by rectangular scanning of the ion beam over areas 10×12 μm^2. The width of the nanowires was determined primarily by the diameter of the ion beam, which could vary from 20 to 100 nm. The nanowire length in different structures may vary from 0.5 to 50 μm. Typically the nanowire length was 10 μm.

The nanowire depth is determined by the penetration depth of Ga^+ ions into diamond substrate. This value was not measured directly but calculated using SRIM code, widely used for simulation of the depth distribution of the ion-implanted ions and the ion-induced damage. In this project, simulations of the damage induced in diamond by 30 keV Ga^+ ion beam at different doses were performed. Typically the ion dose accumulated in in diamond during writing of nanowires was in the order of 10^{16} cm^{-2}. This dose well exceeds the amorphization threshold of diamond, which, depending on the ion energy, ion beam focus and the ion beam current, may range from 5×10^{14} to 3×10^{15} cm^{-2} [2, 3]. The simulated depth distribution of the

ion-induced damage is shown in Fig. 1.6. It is seen that the distribution of the defects can be traced down to a depth of 28 nm. However, taking into account the critical concentration of the primary vacancies 10^{22} cm^{-3}, which is required to provide the ion-induced amorphization of diamond [4], the depth of the amorphized layer spreads down to 20 nm only.

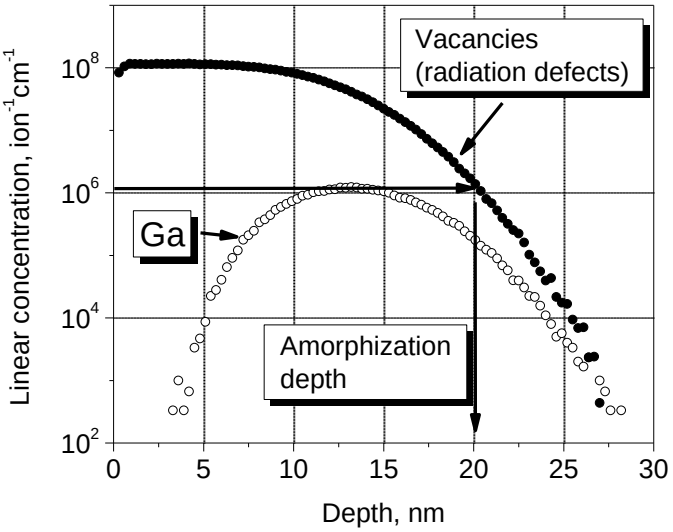

Fig. 1.6. SRIM code simulation of the depth distribution profile of primary vacancies created in diamond by 30 keV Ga^+ ions in diamond at a dose of 10^{16} cm^{-2} (full circles). The vertical arrow shows the depth of the amorphized (graphitized after annealing) layer. The depth distribution of the implanted Ga ions (open circles) is shown for reference. For the dose 10^{16} cm^{-2}, the minimum linear concentration of radiation defects per ion, which is required for the critical volume defect concentration of 10^{22} cm^{-3}, is 10^6 cm^{-1}.

Since the irradiation-induced amorphozation strongly depends on the irradiation dose, the conductance of carbon nanowires is also dose dependent. The evolution of the conductance of an FIB-written carbon nanowire with the increase in the ion irradiation dose is shown in Fig. 1.7. It is seen that the conductance of the as-irradiated nanowire emerges at doses above a certain threshold of 3×10^{15} cm^{-2}. The conductance gradually increases with the dose and comes to saturation at doses above 10^{17} cm^{-2}. After annealing, the nanowire exhibits much greater conductance manifesting the conversion of the ion-induced amorphous carbon into graphite. The dose threshold of the conductance onset becomes much sharper after annealing and the conductance saturation is attained at a dose of 5×10^{17} cm^{-2}.

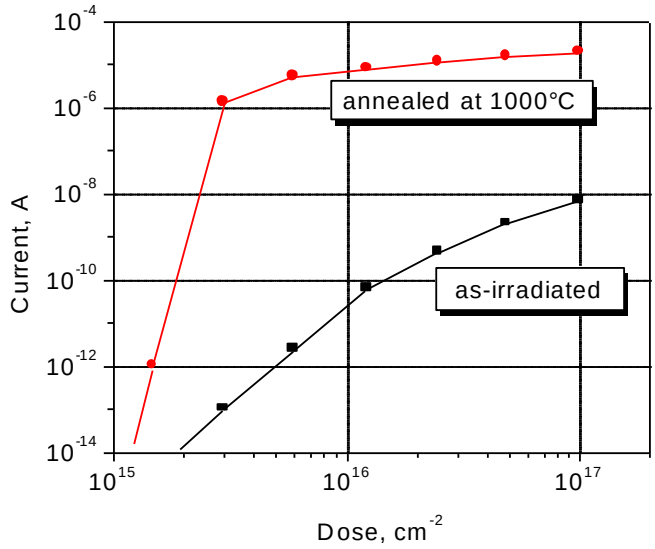

Fig. 1.7. Current in an individual 15 μm long nanowire in a single nanowire structure under 1 V bias versus ion irradiation dose: (squares) - as irradiated, (circles) - after annealing at 1000°C.

The increase in the nanowire conductance with the annealing temperature is shown in Fig. 1.8. The conductance grows fast with temperature increase and comes to saturation at temperatures above 600°C, revealing complete conversion of the amorphous carbon into graphite. After annealing, carbon nanowires may become several orders of magnitude more conductive as they are in the as-irradiated state.

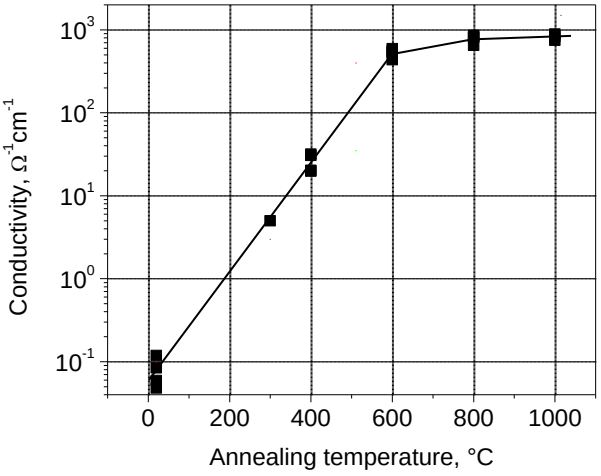

Fig. 1.8. Conductivity of several single carbon nanowires made at a dose of 10^{16} cm^{-2} (well above the graphitization threshold) versus annealing temperature.

It is remarkable that the conductivity of the FIB-written nanowires depends on their length. This effect was reported previously and has been confirmed in the present research. Fig. 1.9 shows the conductance of 30 nm wide nanowires of different length after annealing at different temperatures. It is seen that especially pronounced non-linear behavior is observed after annealing at a temperature of 800°C. After such an annealing, the nanowires with length of a few microns are almost non-conductive and they acquire good conductivity when their

length is reduced below one micron. This effect is considerably reduced after annealing at higher temperatures, though a weak nonlinearity remains even after 1200°C annealing.

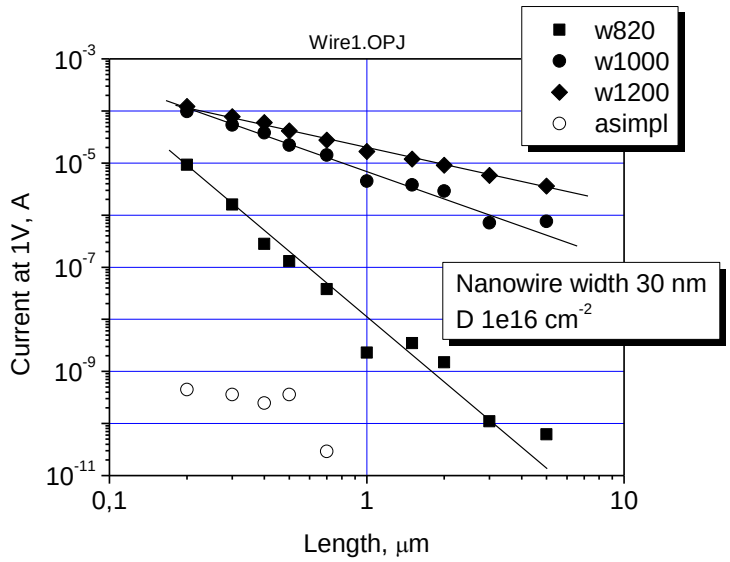

Fig. 1.9. Conductance of FIB-written carbon nanowires of different length in as-irradiated state and after annealing at 820, 1000 and 1200°C. The ion dose accumulated in all nanowires is about 10^{16} cm^{-2}.

I.1.3.2 Broken Nanowire Structures

The broken nanowire structures were made of two in-line nanowires written with a gap between their ends (Fig. 1.10). The gap width varied from 40 nm to 1 μm. These structures were used to study the efficiency of charge carrier injection between the nanowires through insulating diamond.

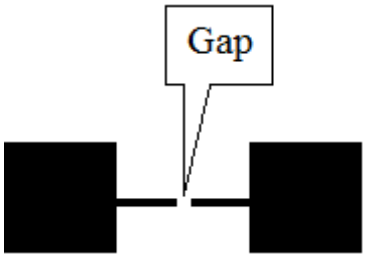

Fig. 1.10. Schematic of broken nanowire structure.

The results of the electrical measurements performed on the broken nanowire structures are shown in Fig. 1.11. Current-Voltage curves of the structures with 200 and 100 nm gaps are very nonlinear revealing an injection character of the current. The characteristics of the 40 nm gap structures, in contrast, were ohmic and almost identical to those taken on the continuous nanowire structures. Thus one can conclude, that the current injection through a 40 nm gap is very high and such a gap does not provide insulation between FIB-written carbon nanowires.

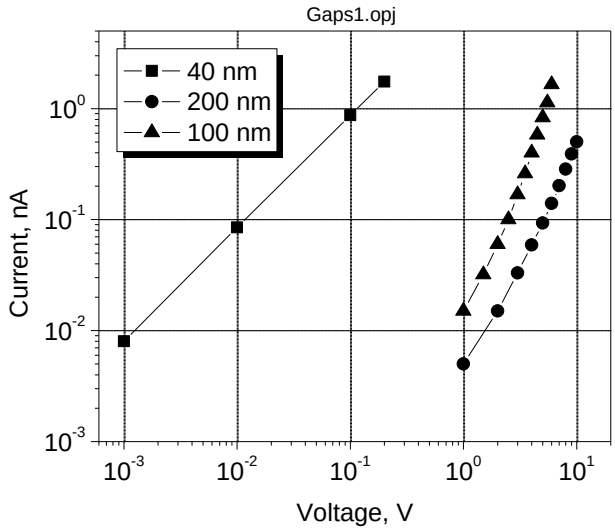

Fig. 1.11. Current-Voltage characteristics of the broken nanowire structures with gaps 40, 100 and 200 nm. The nanowire width is of 50 nm.

To increase the injection current between nanowires and to measure the broken nanowire structures at low voltages the nanowire width was increased to 1 micron. The current-voltage curves of the 1 micron wide carbon wires separated by a 100 nm gap are shown in Fig. 1.12.

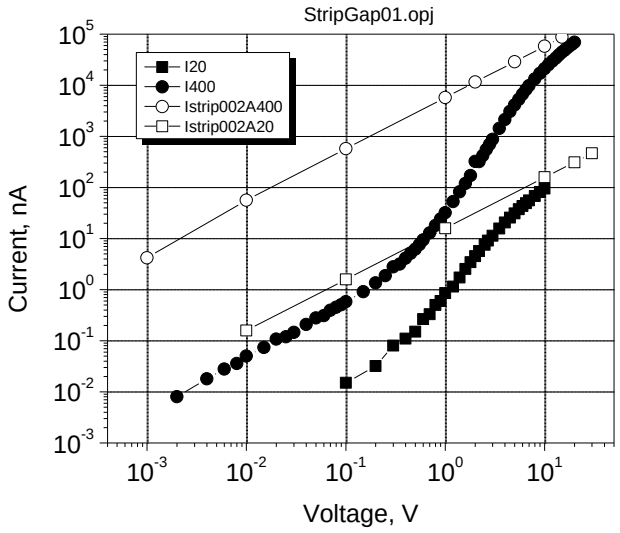

Fig. 1.12. Current-voltage characteristics of broken nanowire structures with 1 micron wide nanowires and 100 nm gap (full symbols). The characteristics are compared with those measured on continuous 1 micron wide wires (open symbols). As-irradiated state (squares); after annealing at 400°C (circles).

The dependence is ohmic at low voltages and becomes superlinear at voltages above of 0.5 V. At higher voltages above 10 V the I-V curve becomes again linear and approaches the dependence of the continuous nanowire. This behavior may be explained by residual radiation defects in the nominally non-irradiated gap, which provide low ohmic conductance at low voltages. At high voltages the injection becomes more efficient than the ohmic conductance

and the current-voltage curve rises superlinearly. At voltages above 10 V the injection efficiency becomes very high and does not limit any more the total current. The limiting factor in this case is the conductance of the nanowires themselves. As a result, at high voltages, the I-V curve of the broken nanowire structure approaches the linear I-V dependence of the continuous nanowire.

The evolution of the injection between the nanowires in the broken nanowire structures with annealing temperature is shown in Fig. 1.13. It is seen that the injection efficiency increases with annealing, the increase is especially pronounced for wider gaps. This behavior is explained by the temperature-induced conversion of amorphous carbon into graphite and lowering the injection barrier in the non-irradiated gap. Besides, the residual radiation defects in the gaps anneal out, the concentration of deep traps in the gaps reduces, the gaps become more structurally perfect. All these transformations may also stimulate the injection of the charge carriers.

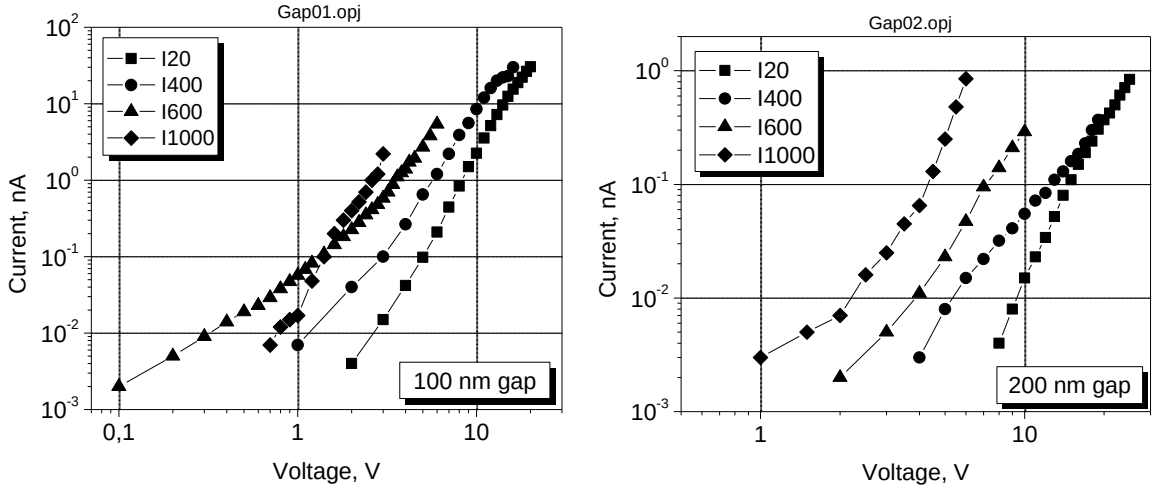

Fig. 1.13. Current-Voltage characteristics of the broken nanowire structures for the gaps 100 and 200 nm measured in the as-irradiated state and after annealing at temperatures 400, 600 and 1000°C.

The I-V curves measured on the structures with gaps 200 nm and below were identical when measured with increasing and decreasing voltage. In contrast, greater gaps revealed a hysteresis in their I-V curves: the greater gap the stronger hysteresis (Fig. 1.14).

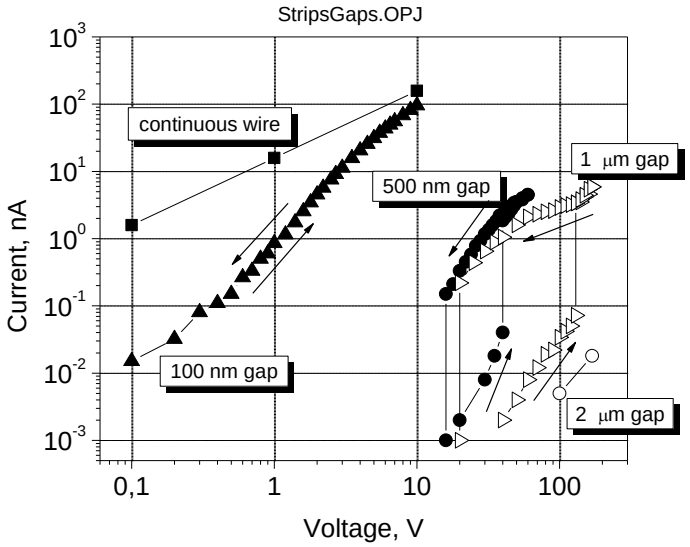

Fig. 1.14. Current-Voltage curves of the broken nanowire structures with gaps 0.1, 0.5, 1 and 2 μm measured after annealing at 600°C. The structures with gaps 0.5 μm and greater reveal injection at high voltages and pronounced hysteresis.

Similar to thin nanowires, the injection efficiency through the gaps in 1 micron wide wires also increases with annealing temperature (Fig. 1.15). The hysteresis equally becomes more pronounced with annealing.

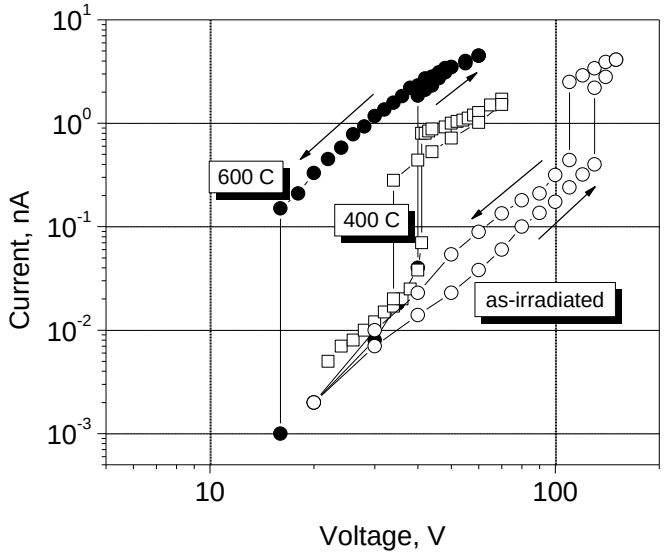

Fig. 1.15. I-V curves of a broken nanowire structure with 0.5 μm gap taken in as-irradiated state and after annealing at 400 and 600°C.

The observed hysteresis of the broken nanowires can be explained as a manifestation of S-type current-voltage curves of a unipolar diode, the i-zone of which contains deep traps. This type of characteristics is very common for unipolar diamond p-i-p diodes made by boron ion implantation. The theory of this effect has been well developed. S-type I-V curves in the

carbon nanowire structures is an interesting result showing, that the broken nanowires may be used as devices for nanoelectronic generators.

I.1.3.3 Single Nanodot Structures

Single nanodot structures were made of the broken nanowire structures by additional irradiation of single dots in the middle of the non-irradiated gaps (Fig. 1.16). The primary goal of studies of current flow in the nanodot structures was the observation of coulomb blockade effects at room temperature. Since the size of the FIB-written nanodots can be as small as 10 nm, one may expect that the capacitance of such nanodots placed close to terminals of carbon nanowires may be as small as 10^{-18} F. Thus the effects of single electron charging may be observable at room temperature. The results of the measurements of the broken nanowire structures revealed that 40 nm non-irradiated gaps between the nanowires are not really isolating. Therefore the minimum gap for the nanodot structure was expected to be made twice as much, that is about 100 nm. Taking this consideration into account the nanodot structures with the gaps of 100 and 200 nm were fabricated and studied.

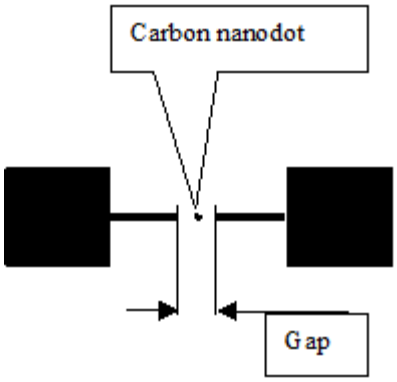

Fig. 1.16. Single nanodot stucture. Nanodot is made in the middle of the gap between two nanowires.

Typical room temperature current-voltage characteristics of the nanodot structures are shown in Figs. 1.17 and 1.18. The I-V curves are superlinear and resemble those obtained on the broken nanowire structures. The nanodots made at small doses do not influence considetably the I-V curves measured on the as-irradiated structures or after annealing at temperatures up to 500°C. The nanodots made with higher doses were found to increase the current in the structure as if their presence just reduces the gap size. However, in a structure with nanodot made with a dose of 1×10^{16} cm^{-2} the current injection was unexpectedly reduced several times.

After annealing at temperatures above 1000°C, behavior of the structures changes considerably. The structures become much more conductive and the presence of the nanodots drastically changes the current injection. The high dose nanodots bridge the gap between the nanowires resulting in perfectly ohmic I-V curves, which coincide with that taken from the continuous nanowires. However, the structure with the nanodot made at the lower dose reveals a drastic decrease in the current. It looks like the presence of the nanodot blocks the injection between the terminals of the nanowires.

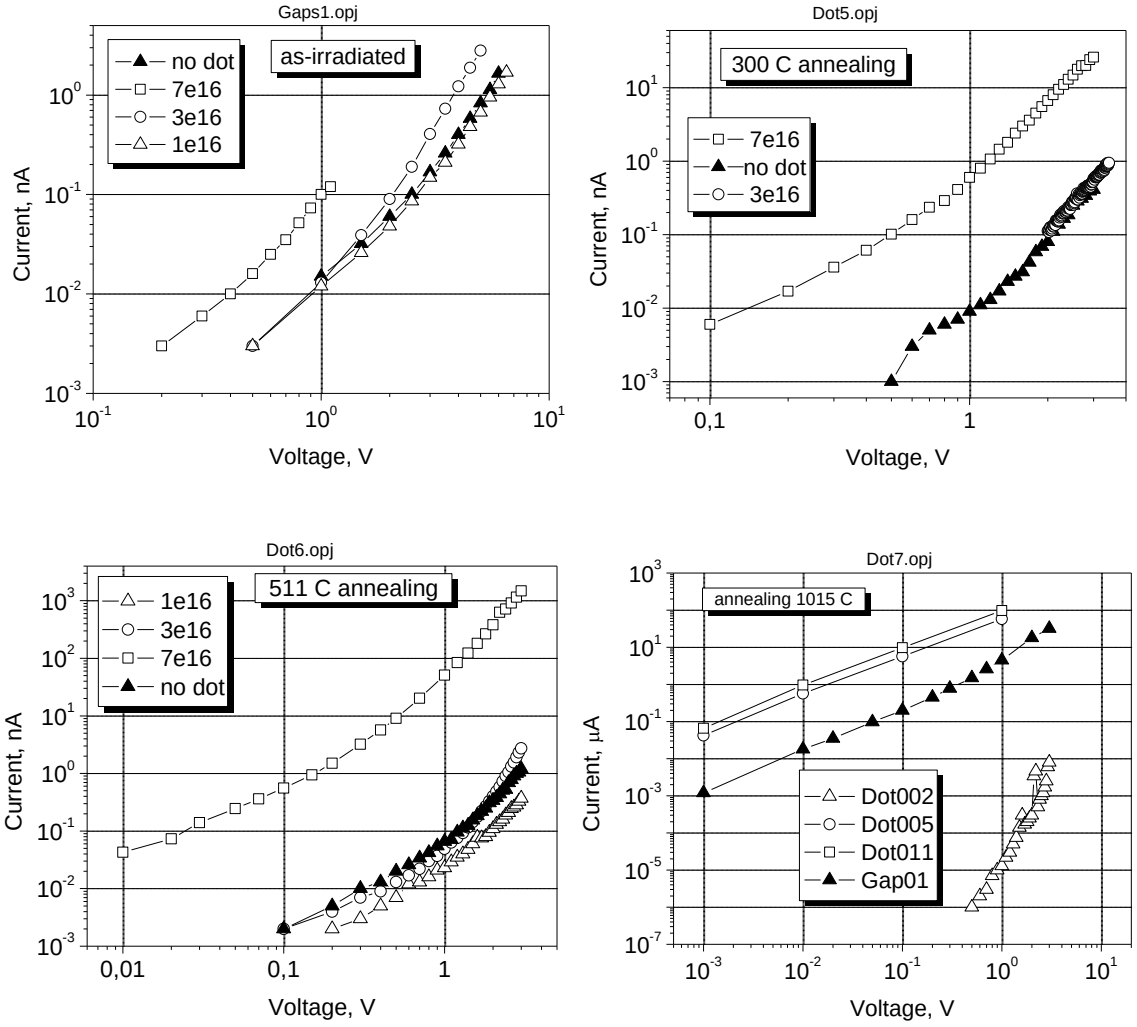

Fig. 1.17. Current-voltage characteristics of 100 nm gap single nanodot structures with the nanodots made with ion doses 1×10^{16}, 3×10^{16} and 7×10^{16} cm^{-2}. The structures were measured in as-irradiated state and after annealing at 300, 511 and 1015°C.

Similar behavior was observed on the single nanodot structures with 200 nm gaps (Fig. 1.18). The as-irradiated structures revealed gradual increase of the current with increase of the nanodot size (increase in the nanodot dose). However after 600°C annealing the small nanodots blocked the current injection in the structures.

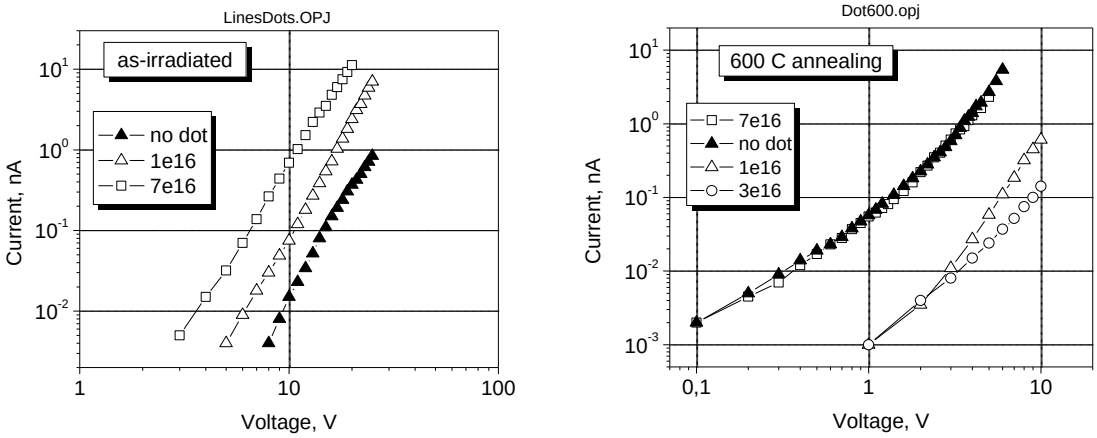

Fig. 1.18. I-V curves of 200 nm gap single nanodot structures with nanodots made at doses 1×10^{16}, 3×10^{16} and 7×10^{16} cm^{-2}. The measurements were performed on the as-irradiated structures and after annealing at 600°C.

We believe that the observed decrease in the injection current in the annealed nanodot structures is caused by a coulomb blockade mechanism. To have a better insight in this effect careful measurements of I-V curves of some structures were performed (Fig. 1.19).

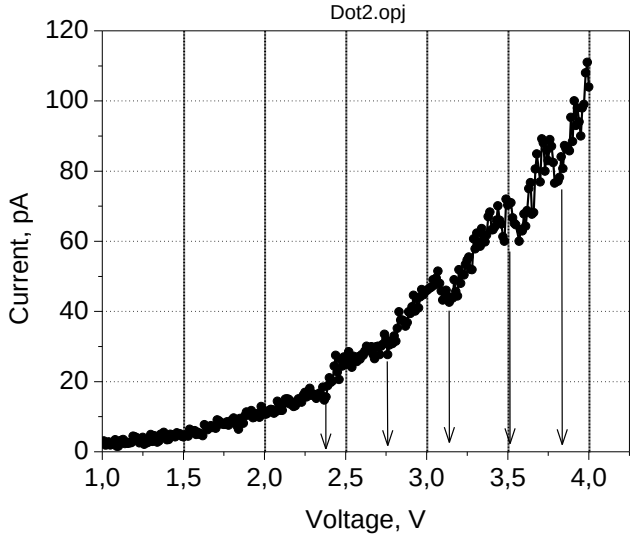

Fig. 1.19. Current-voltage curve of a 200 nm gap nanowire structure with a 20 nm nanodot made at a dose of 3×10^{16} cm^{-2}. The structure was measured after annealing at a temperature of 1000°C.

Almost all the measured structures revealed a rather noisy behavior, which, however was modulated with more or less visible oscillations. These oscillations were equidistant in voltage scale with the period ranging from 0.1 to 0.5 V for different structures. This value is quite consistent with the single electron charging energy of a carbon nanodot in diamond with its rather low dielectric constant. In order to estimate the capacitance C of the FIB-written nanodot it can be approximated by a sphere of diameter d. Then $C = 2\pi\varepsilon_o\varepsilon d$, and for d = 20 nm we obtain

$C = 8\times10^{-18}$ F. When charging such a nanodot with a single electron, its potential would increase by 20 mV. The experimental value, however, is an order of magnitude greater averaging 200 mV. This discrepancy one could explain assuming that the real size of the electrically conductive FIB-written carbon nanodot is some 10 times smaller than the ion beam diameter seen on the diamond surface as the imprint. This assumption is quite plausible for the ion doses used for fabrication of carbon nanostructures (about 10^{16} cm^{-2}), which are several orders of magnitude lower than those required to sputter a visible spot on diamond surface (about 10^{20} cm^{-2}).

I.1.3.4 Carbon Nanodot Chain Structures

The scheme of the structures with carbon nanodot chains is shown in Fig. 1.20. Two sets of structures were fabricated. One set included the structures with gaps ranging from 40 to 200 nm in which one, two and three nanodots were imbedded equidistantly. Another set comprised 500 nm gap structures with many nanodots uniformly placed one from another at distances from 5 to 60 nm.

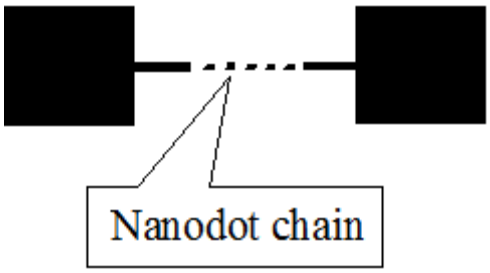

Fig. 1.20. Carbon nanodot chain structure is made as a broken nanowire structure with a gap large enough to accommodate several isolated nanodots.

Neither of these structures exhibited noticeable conductance at a bias of 1 V when in the as-irradiated state. The onset of the conductance was observed only after annealing at temperature of 500°C. The nanodot chain structures of the first set exhibited conductance when the gaps between the nanodots were 40 nm and less. The current flowing in these structures under 1 V bias was very unstable and this instability was especially pronounced in the structures with three and more nanodots. Fig. 1.21 shows the combined results of the conductance of the nanodot chain structures of the first set. It is seen that the structures become suddenly conductive, when the gap between the nanodots is reduced down to 40 nm.

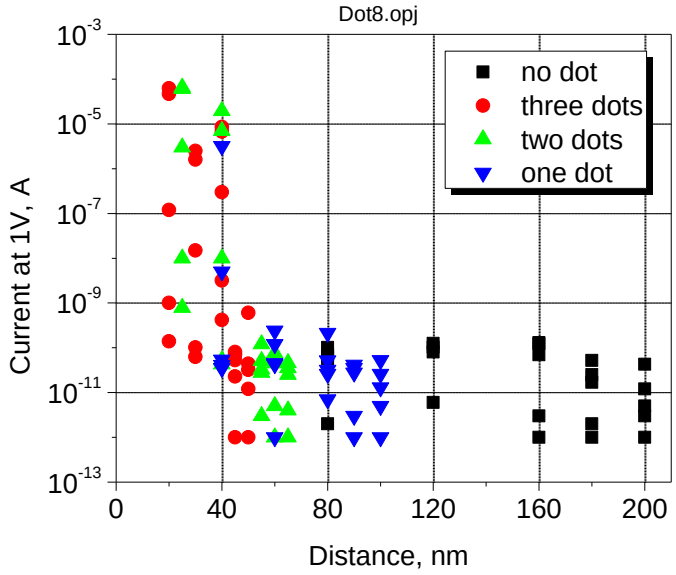

Fig. 1.21. Conductance of the nanodot chain structures measured at a bias of 1 V versus the distance between the nanodots. The measurements were performed on as-irradiated structures and after annealing at 400, 600, 800 and 1000°C. Conductance of the broken nanowire structures with the equal gaps between the nanowires is shown for reference.

In contrast to the first set of the structures, the second set of the structures with long nanodot chains revealed conductance only when the gaps between the dots were about 10 nm and less (Fig. 1.22). Only one structure with dots made by relatively high dose of 10^{17} cm^{-2} reveal conductance for the gaps of 20 nm.

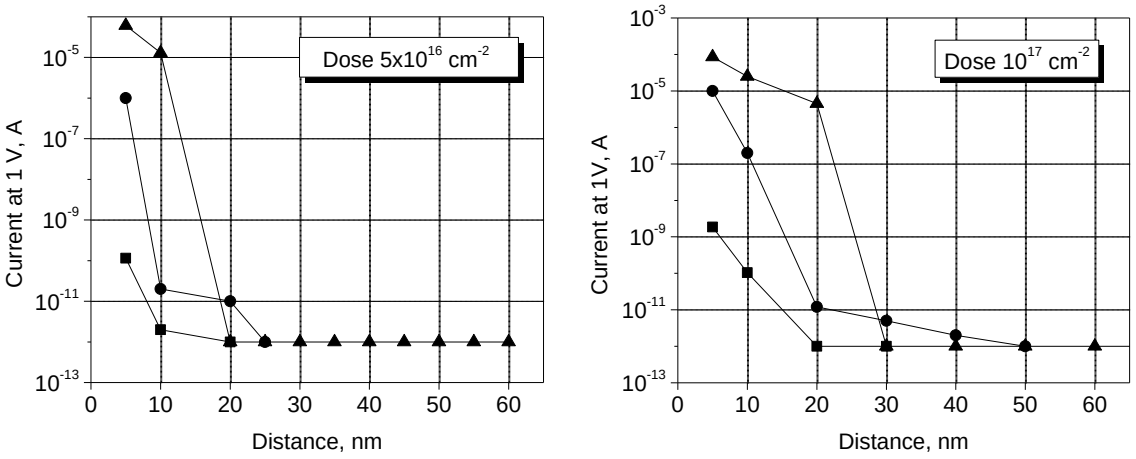

Fig. 1.22. Conductance of the long chain nanodot structures made with ion doses of 5×10^{16} cm^{-2} and 10^{17} cm^{-2}. (■) - as-irradiated, and after subsequent annealing at temperatures 500°C (●) and 1000°C (▲).

The conductance of the long chain structures could not be initiated even after annealing at 1000°C, when the complete transformation of amorphous carbon in graphite occurs. It is remarkable, that some structures were tested at a bias up to 30 V, which resulted an electric

field of 10^6 V/cm in the gaps. Nevertheless, even this high electrical field could not generate current in the long chain structures. These results strongly support the idea of the coulomb blockade which controls the electron transport in the FIB-wrirren nanodot-nanowire structures.

I.1.3.5 Nanowire array structures

Two types of nanowire array structures were fabricated and measured (Fig. 1.23).

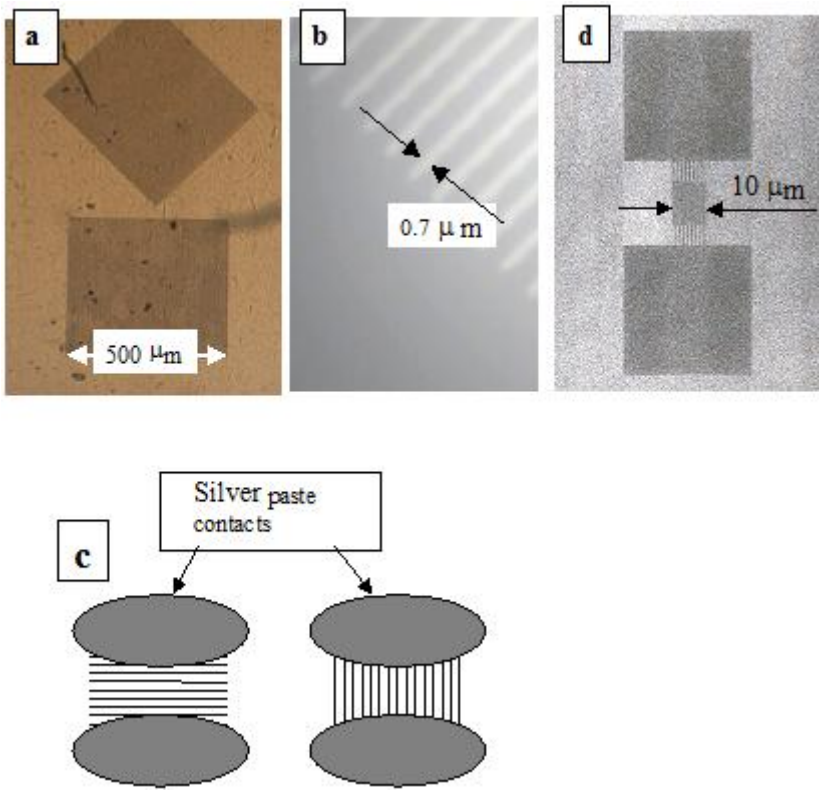

Fig. 1.23. (a) Polycrystalline CVD diamond film substrate with two 500 μm carbon nanowire structures. (b) A fragment of one of the 500 μm structures showing individual nanowires. Note that the gap between the nanowires is not graphitized and transparent. (c) Scheme of application of silver paste contacts for the current measurements perpendicular and along the nanowires in the 500 μm structures. (d) FIB image of the interdigital carbon nanowire structure. Overlapping area of two interintruding nanowire combs is about 10×10 μm^2.

The structures of the first type were made as arrays of parallel carbon nanowires written with a repetition period of 2 microns. Each structure of this type covered an area of 500×500 μm^2 (Fig. 1.23a). Each nanowire was made by linear scan of the ion beam. The structures of another type were made as two interdigital comb arrays penetrating one into another with an overlapping area of 10×10 μm^2 (Fig. 1.23d). The repetition distance between the nanowires in the overlapping area was 500 nm. Each nanowire comb was connected to a contact pad made by uniform scanning of the ion beam over area of 30×30 μm^2. After annealing, the width of the nanowires in the big 500 μm structures was about 0.7 μm (as seen in optical microscope). Thus the insulating diamond gap between the nanowires was about 1.3 μm. The nanowires of the small 10 μm structure had the width of 200 nm (as seen in the FIB image). In this case the

insulating diamond gap between the adjacent nanowires in the interdigital area was about 300 nm.

The nanowire aray structures were characterized in a temperature range from 30 to 250°C in open air. The variations in the current versus applied bias and temperature were measured. The big 0.5 mm structures were biased in two directions: along nanowires and perpendicular to them (Fig. 1.23c). As expected, the conductance along nanowires was high and perfectly ohmic (Fig. 1.24), while that measured in the perpendicular direction was much lower and superlinear at high voltages. The current-voltage characteristics taken at room temperature in the perpendicular direction follow a power dependence with the scaling exponent increasing from 1 to 4 as the voltage increases to 10 V. This behavior resembles that observed in [2], where the conductance through narrow gaps of the non-graphitized diamond between two Ga^+ ion irradiated areas was discussed in term of an electron injection in a heterojunction (graphite)-(diamond). This injection model is used in the present work too. Indeed, as the structures reveal no visible shortcircuits between the nanowires and the non-graphitized diamond gaps between the nanowires are fully transparent, the possibility of formation of conductive areas, which could bridge the nanowires, should be excluded. Equally, the observed conductance cannot be explained by a slight irradiation of the diamond gaps between the nanowires, which is expected after the exposure to a focused ion beam, which is always surrounded by a low intensity halo. Even assuming that the gaps were irradiated with a dose sufficient to provide a conductance in the as-irradiated state, the following annealing at high temperature in vacuum removed the irradiation damage and restore the insulating properties of diamond.

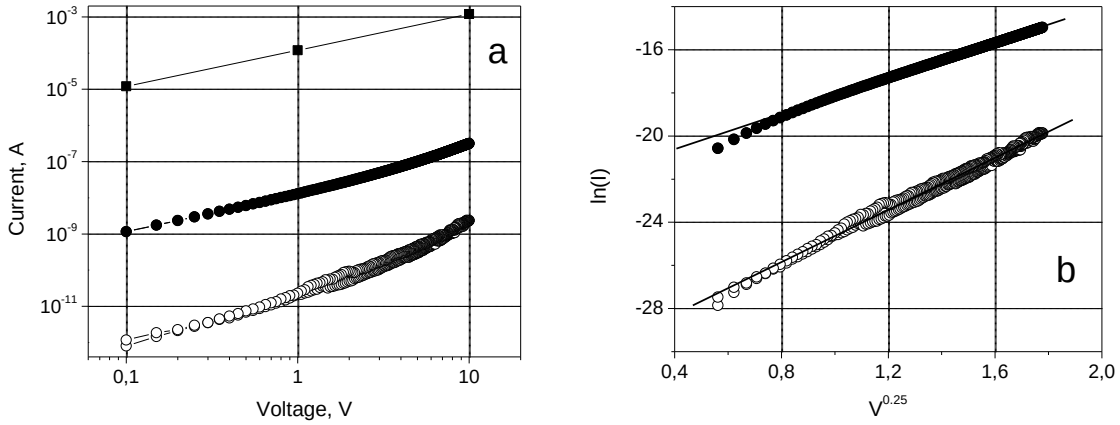

Fig. 1.24. (a) Curent-Voltage characteristics of a 0.5 mm nanowire array structure measured along nanowires at room temperature (full squares) and perpendicular to nanowires at room temperature (open circles) and at a temperature of 210°C (full circles). (b) *I-V* curves taken perpendicular to the nanowires and presented as a function $\ln(I) = f(V^{0.25})$: at room temperature (open circles) and at a temperature of 210°C (full circles).

The experimental *I-V* curves can be well explained by the Pool-Frenkel emission model developed for diamond *p-i-p* unipolar diode [5]. In this case the *I-V* curve follows an exponential dependence:

$$I \sim \exp\left[\frac{e}{kT}\left(\left(\frac{2e^3 N_T}{\left(\varepsilon\varepsilon_0\right)^3}\right)^{0.25} V^{0.25} - \varphi_T\right)\right],$$

where e is the electron charge, k is the Boltzmann constant, N_T is the concentration of deep traps in the gap between nanowires, T is the absolute temperature, ε and ε_0 are relative dielectric constant of diamond and the absolute dielectric constant of vacuum respectively, V is the applied voltage and φ_T is the potential of the deep traps. Using this relation, the concentration of the deep traps N_T controlling the current injection can be estimated from the slope of the dependence $\ln(I) = f(V^{0.25})$. It was found $N_T = 1.2\times10^{16}$ cm^{-3} and 0.3×10^{16} cm^{-3} for room temperature and 210°C respectively. The concentration of deep traps in the order of 10^{16} cm^{-3} is consistent with the expected residual radiation damage of the gaps between the nanowires produced by a focused ion beam, which is always surrounded by a halo. The reduction of this concentration with the temperature increase is explained by the rise of the Fermi level, filling the traps and, consequently, reducing their effective concentration.

The current-voltage characteristics of the small 10 μm structure also shows a superlinear dependence, revealing injection nature of the conductance between the nanowires (Fig. 1.25). Similarly to the big 500 μm structure, the the *I-V* curve of the 10 μm structure can be well fitted by a linear dependence when presented in coordinates $\ln(I) = f(V^{0.25})$.

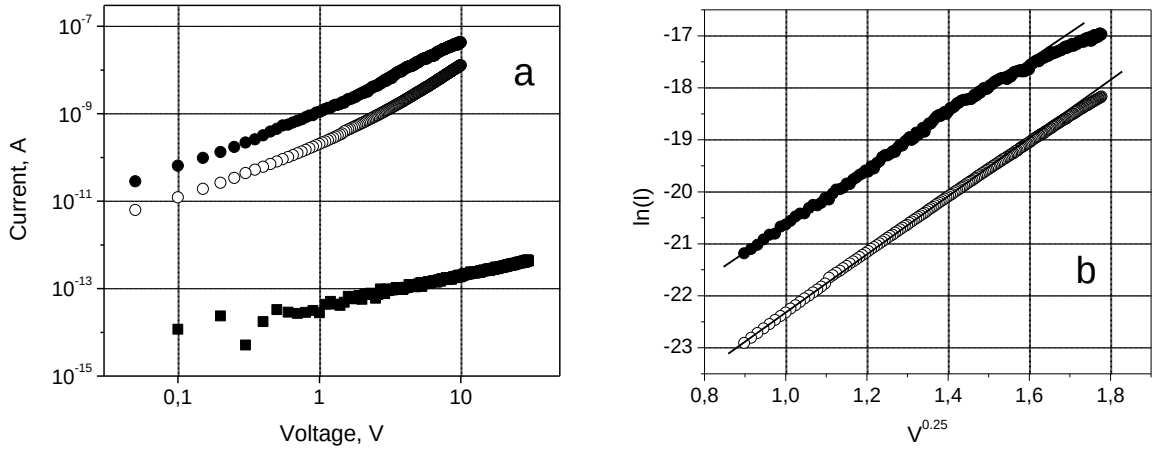

Fig. 1.25. (a) Current-voltage characteristics of the small 10 μm nanowire array structure taken at room temperature (open circles) and at a temperature of 100°C (full circles). Conductance over the non-irradiated intact surface of the diamond substrate measured close to the structure is very low and is shown for reference (full squares). (b) *I-V* curves of the picture (a) but presented in coordinates $\ln(I) = f(V^{0.25})$.

I.1.4 Raman Characterization

Raman measurements of the FIB-written carbon nanostructures were performed on nanowire grids. The data was compared with that obtained on homogenously irradiated contact pads. Since the diameter of the laser beam used in the measurements was about 1 μm several nanowires of the grid were excited simultaneously giving a reasonably strong signal (Fig. 1.26).

The Raman spectra are shown in Fig. 1.26. Qualitatively there is no difference between the spectra taken from nanowires and contact pads. The main feature is a broad asymmetric band with a maximum at 1550 cm^{-1} and two bands at 400 and 700 cm^{-1}. A little difference is that the maximum of the main band measured on the nanowires is shifted towards greater wavenumbers by about 20 cm^{-1}. These three bands are well known in Raman spectra of the ion-irradiated diamonds. The 1550 cm^{-1} band is the I-band ascribed to the ion irradiation induced amorphous carbon, which is formed in the as-irradiated diamonds. The 400 and 700

cm^{-1} bands are believed to originate from the acoustical phonons of the distorted diamond lattice. A striking peculiarity, however, is the persistence of the I-band after annealing at 1200°C. It is well known, that in diamond after regular ion irradiation with macroscopic ion beam this band stands annealing up to 500°C and at higher temperatures it splits in two distinct narrower G-band and D-band with maxima at 1600 cm^{-1} and 1350 cm^{-1} respectively. Such a transformation was also reported for diamonds after 100 keV Ga^+ ion FIB irradiation with a 100 nm diameter ion beam and subsequent annealing at 1300°C (see Fig. 1.26). This surprising difference in not still fully understood. However it can be assumed that the stable I-band manifests the formation of an amorphous carbon phase stable at high temperatures. In the following theoretical part we speculate that such a phase can be formed at nanoscale. Thus based on the experimental results we assume that the dimension of the size of the volume where the stabilization of the carbon amorphous phase can occur is of 10 to 30 nm. This is value a few times less than the size of the minimum volume, which could be attained with the 100 keV Ga^+ ion FIB irradiation (above 100 nm).

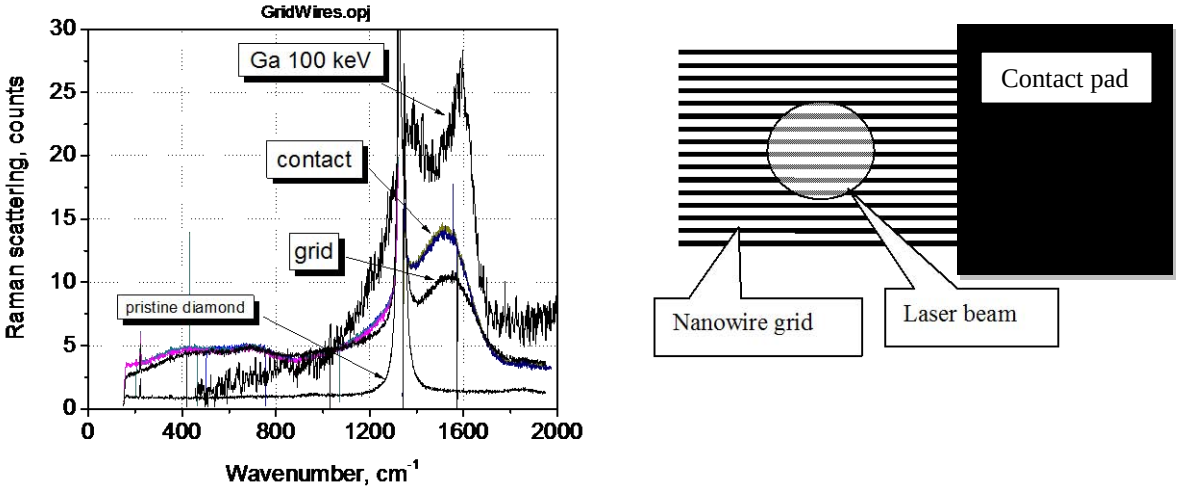

Fig. 1.26. Scheme of the laser beam excitation of the nanowire grid during the Raman measurements and the spectra obtained on nanowire grid and contact pad after annealing at 1200°C. The spectra are compared with those measured on diamond irradiated with 100 keV Ga^+ focused ion beam after high temperature annealing and pristine diamond substrate.

In order to check the influence of crystallographic orientation of carbon nanowires on their atomic structure, two sets of FIB-written carbon nanostructures were prepared for Raman measurements on high quality CVD diamond films oriented in (100) plane: (i) 5×5 μm^2 arrays of 30 nm nanowires written at different angles with respect to the crystallographic directions of the substrate, and (ii) 5×5 μm^2 arrays of 30 nm nanodots. The structures were made with different ion doses in the range from 10^{13} to 10^{16} cm^{-2}. Thus there were structures made with doses below and above the graphitization threshold, which was found to be at a dose of 10^{15} cm^{-2}. Raman spectra of the structures were taken on the as-irradiated structures and after subsequent annealing at temperatures up to 1400C.

There was no difference in Raman spectra of the nanowire structures written in different directions. Thus it was concluded that the internal atomic structure of the nanostructures did not depend on the orientation of the diamond substrate. The nanowire structures exhibited similar Raman spectra to those obtained on the nanodot structures (Fig. 1.27).

Raman spectra clearly indicate formation of amorphous carbon at doses below the graphitization threshold (a broad structureless band at 1600 cm^{-1}) and formation of disordered graphite at doses above the graphitization threshold (three bands at 1300, 1580 and 1620 cm^{-1}). It is remarkable that the FIB-induced amorphous carbon remains stable to a temperature of 1000C. This high temperature stability of the amorphous carbon confined at nanoscale had been predicted and explained theoretically (see below). It is also interesting that the Raman spectra of non-graphitized (amorphous) nanodots exhibit some narrow lines at 1500, 1640 and 1770 cm^{-1}, which are believed to originate from major radiation defects of highly damaged diamond. The graphitized area, as expected, remain unchanged to temperatures 1400C.

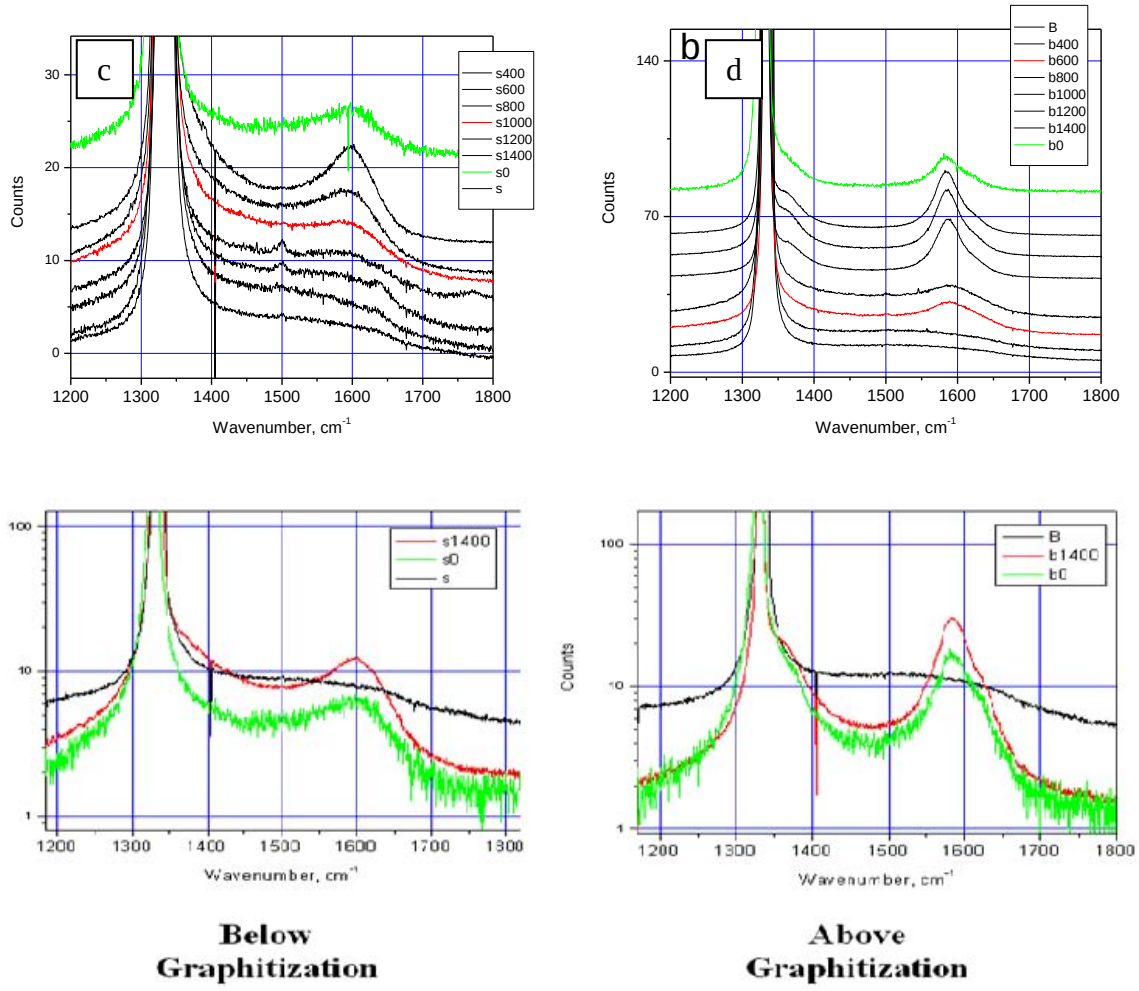

Fig. 1.27. Raman spectra of arrays of 30 nm carbon nanodots made with doses below (a) and above (b) the graphitization threshold. The spectra were taken on as-irradiated structures and after annealing in vacuum at temperatures indicated in inserts. (c) and (d) show the most characteristic Raman spectra of amorphous carbon and graphitized carbon.

I.1.5 Temperature sensitivity of the nanowire array structures

The temperature dependence of the conductance of the big 500 μm structure measured along the nanowires and perpendicular to them is shown in Fig. 1.28. The current along the nanowires is much greater than that flowing in the perpendicular direction and exhibits almost no change with temperature. In the contrast, the current measured perpendicular to the nanowires I (T) reveals an order of magnitude increase with the temperature rising from 40 to 140ºC. To explain this temperature-induced increase in current the experimental I (T) curve

was simulated by two dependencies [6]: (i) the Mott's law of variable range hopping ($I = I_0\exp(T/T_0)^{0.25}$), and (ii) the dependence of activation of charge carriers over an energy barrier ΔE ($I = I_0\exp(-\Delta E / k_B T)$. It was shown that the Mott's law well described the electrical conductance of diamond damaged above the graphitization threshold [7]. Sine the irradiation of gaps between the nanowires was much below the graphitization threshold in the present case, we have to exclude the variable range hopping mechanism. The energy activation mechanism is characteristic of the near-neighbor hopping conductance or injection currents, which are very feasible in hetrostructures. The second reason, because of which we have to exclude the Mott's mechanism, is too high conductance between the nanowires, which requires to assume too high concentration of the charge carriers (concentration of the electrically active defects) in the non-graphitized gaps. Since the resistance of the structures at a temperature of 200°C is about of 2.5 MΩ, we have to assume that the specific resistivity of the nongraphitized gaps is in the order of 10^3 Ωcm. This value is much greater that 10^8 Ωcm expected for diamond after an ion irradiation with a sub-threshold dose and a subsequent annealing at 1200°C [7].

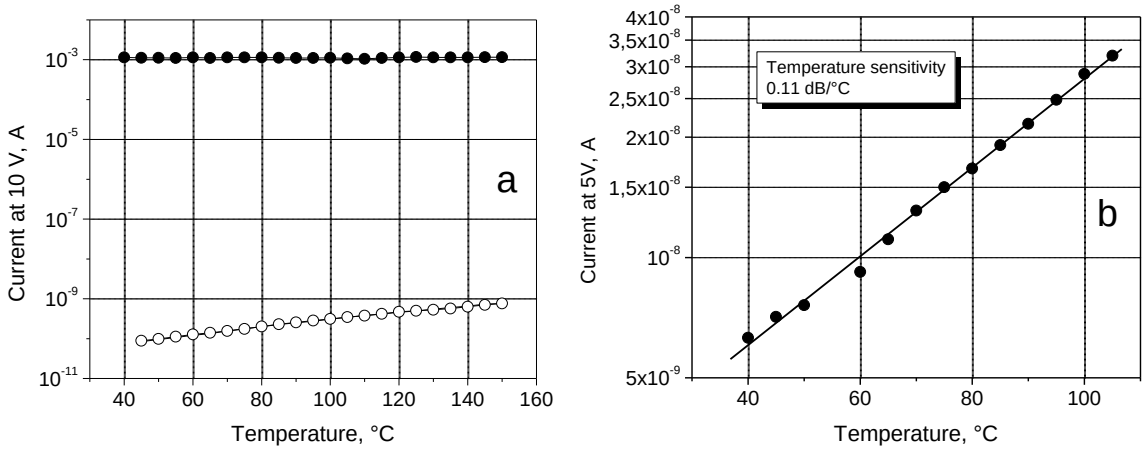

Fig. 1.28. a) Comparison of the temperature-induced current variation of the 0.5 mm sensor along nanowires (full circles) and perpendicular to nanowires (open circles) with temperature in the range from 40°C to 150°C. b) Current of the small 10 μm sensor versus temperature at a bias of 5 V.

The small 10 μm nanowire array structure, similarly to the big 500 μm structures, also exhibited a good temperature sensitivity with almost exponential increase in current versus temperature (Fig. 1.28b). Note that the conductance of the small structure is much greater than that of the big one because of the shorter gaps between the nanowires and, consequently, much higher injection efficiency.

The temperature dependence of the current flowing through the structure, when presented as Arrhenius plot, is perfectly linear indicating a definite activation energy controlling the charge carrier injection between the carbon nanowires (Fig. 1.29). The activation energy was measured on the big structures and was found to be 0.25 eV. This is an optimal value for the activation energy of a resistive temperature sensor working at moderate temperatures. It allows both rather high temperature sensitivity and acceptable ohmic resistance. In the nanowire sensors the activation energy of conductivity is comparable to that characteristic of *p*-type semiconductive diamond temperature sensors. However, the advantage of the FIB-written carbon nanowire sensor is the absence of any electrically active impurities and doped semiconductive areas. The temperature response of the carbon nanowire sensors is reasonably

high having a value of 0.1 dB/°C.

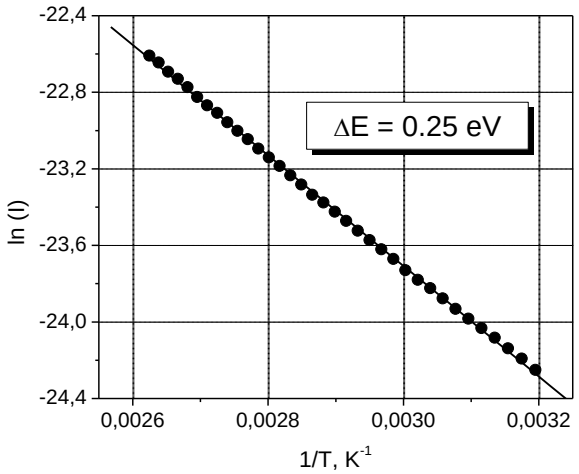

Fig. 1.29. Current-Temperature dependence measured on big 500 μm nanowire array structure and presented as Arrhenius plot. Linear fit of the experimental points is shown with the line. The activation energy derived from this plot is 0.25 eV.

A positive technological feature of the carbon nanowire temperature sensors is rather high intrinsic conductivity of the FIB-written carbon nanowires, which is commonly in the order of 10^3 Scm^{-1}. For some nanowires of a submicron length the conductivity may even exceed 10^4 Scm^{-1} [3]. This feature solves the problem of electrical contacts and leads connecting the sensor with outside circuit. It is important to note that the conductivity of the annealed FIB-written nanowires does not depend noticeably on temperature (at least from room temperature to 200°C), which is similar to the behavior of graphite with its low TCR of about 5×10^{-4} K^{-1} [8], or 5×10^{-3} dB/°C. Thus the reading of a carbon nanowire sensor is not affected by the temperature dependence of its leads and interconnections.

Another advantage of the carbon nanowire sensors is their blindness to visible light. We did not notice any measurable changes in the sensor reading under an intense illumination with white light.

Though possessing several important advantages the novel carbon nanowire temperature sensors have their own specific limitations. For instance, when operating in the open air they remain stable only at temperatures below 400°C. At higher temperatures the ion-induced amorphous carbon and graphite may oxidize and this oxidation destroys the sensor structure. To avoid this, a protective layer is required at elevated temperatures. We assume that a CVD diamond film grown over the sensor structure could serve well as a protective coating. Such a coating could extend the temperature range of the sensor up to 1000°C. At temperatures above 1000°C another limitation specific for diamond-based device comes in play. It is the spontaneous graphitization of diamond surface, which can be noticeable at temperatures of 1000°C and above even in good vacuum or in an inert atmosphere.

Rather high resistance of the present carbon nanowire temperature sensors (1 GΩ and above at room temperature) should not be a problem once the geometry of the sensor is optimized. The main parameter determining the resistance of the nanowire structure is the width of the gap between the nanowires. Since the current injection increases with the reduction of the gap exponentially one may expect much greater currents and, hence, much lower resistance for sensors with short gaps. Figs. 1.11 through 1.15 illustrate the increase in

the injection current between FIB-written nanowires with the reduction of the gap between them. A 200 nm gap reveals good insulating properties. Reduction of the gap to 100 nm may increase the injection by a few orders of magnitude yet keeping the current considerably lower than that that observed for two contacting nanowires. A 40 nm gap reveals the current between the nanowires close to that measured for the directly contacting nanowires. From these results we can conclude that the minimum gap between the nanowires in the nanowire-grid structures may be as short as 100 nm. Simple calculations show that for such a short gap the total resistance of the sensor may be attained as low as 1 kΩ.

I.1.7 Chemical sensitivity of FIB-written nanostructures

I.1.7.1. Chemiocal sensitivity of nanowire array structures

Chemical sensitivity of the arrays of FIB-written carbon nanowires was discovered when we noticed their response to human breathing (Fig. 1.30a). The structures were very sensitive revealing response to a regular human breathing at a distance up to 1 m. The analyte resulting in the increase in the current flowing through the sensor during breathing was found to be mainly water vapor. In order to check it tiny droplets of different liquids were brought to sensor to a distance of 1 centimeter. The sensor exhibited immediate response to such an exposure exhibiting a maximum sensitivity for water (Fig. 1.30b). The chemical response of the sensor is very fast. It reacts in seconds to the appearance of a droplet and to its removal. Interesting, that the sensor reveals positive response (increase in current) to water and alcohol, but negative response to toluene (decrease in current). Thus we can expect that the sensor may possess a certain chemical selectivity.

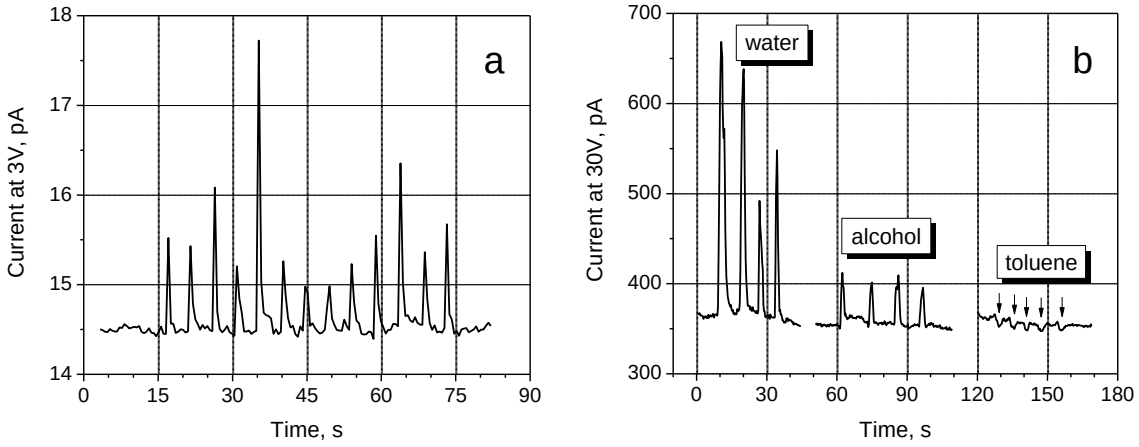

Fig. 1.30. (a) Response of a big 500 μm sensor to breathing of a person sitting in front of it at a distance of 70 cm. (b) Response of the sensor to droplets of different liquids rapidly brought to a distance of 1 cm to the sensor and then rapidly retracted. Note the current increase for water and alcohol but decrease for toluene.

At present we are not in a position to give a detailed explanation of the chemical sensitivity of the FIB-written carbon nanowire structures. Though, as for a preliminary model, we adhere to one used in [9]. In this work *p-i-M* diodes were fabricated using CVD deposition of boron-doped diamond film followed by the growth of a thin film of nominally undoped insulating diamond. On the upper surface of the undoped diamond a film of a metal-catalyst was deposited. Such a diode, when immersed in an atmosphere with admixture of the analyte gas, exhibited considerable change of its *I-V* curve. The authors explained the sensitivity of

these diodes by the penetration of the analyte molecules or their fragments to the *i-M* interface and change of the energy barrier of the *i-M* junction. In the present case of the carbon nanowire structures we assume that the analyte molecules adsorb on the surface of the insulating diamond gaps between the nanowires and change the energy barrier height of the graphite-diamond junctions, stimulating (or suppressing) this way the current injection between the nanowires (Fig. 1.31).

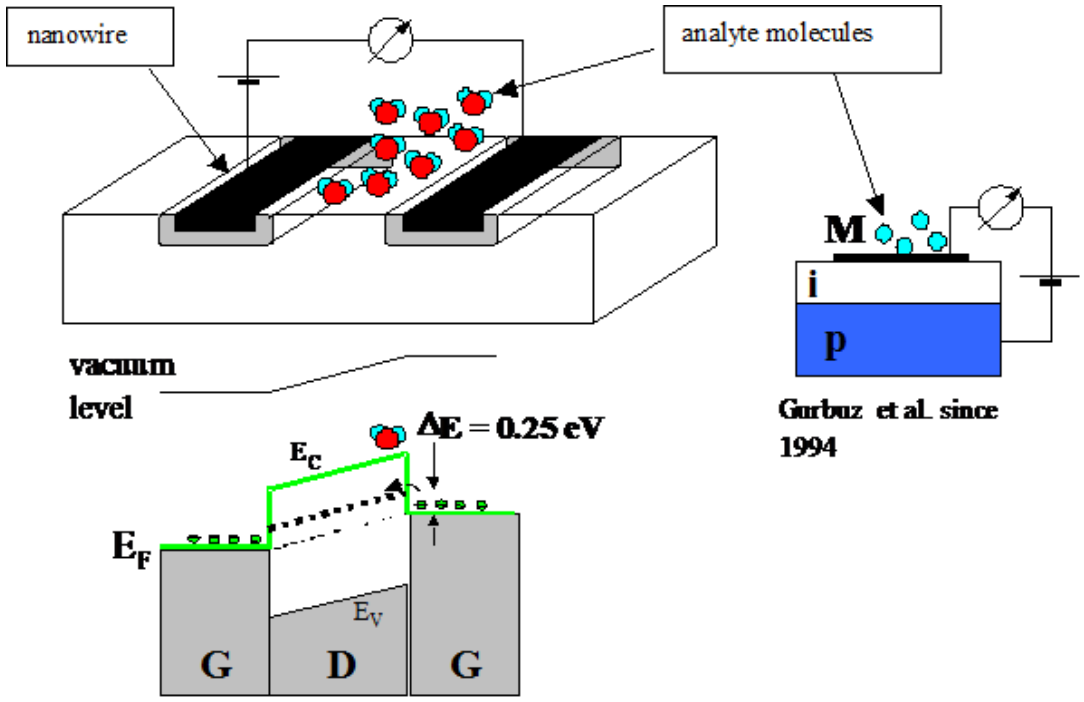

Fig. 1.31. Graphite-diamond-Graphite heterostructure working as a chemically controlled transistor. The energy barrier between two carbon nanowires is changed by the potential of the analyte molecules changing the current through the structure.

I.1.7.2. Arrays of Carbon Nanodots for Sensing Applications

Arrays of carbon nanodots were fabricated on diamond surfaces and their temperature and chemical sensitivity was tested. The arrays were made as squares of different size ranging from 500×500 μm^2 to 5×5 μm^2 (Fig. 1.32). Size of nanodots in the arrays varied from 30 to 700 nm depending on the array size.

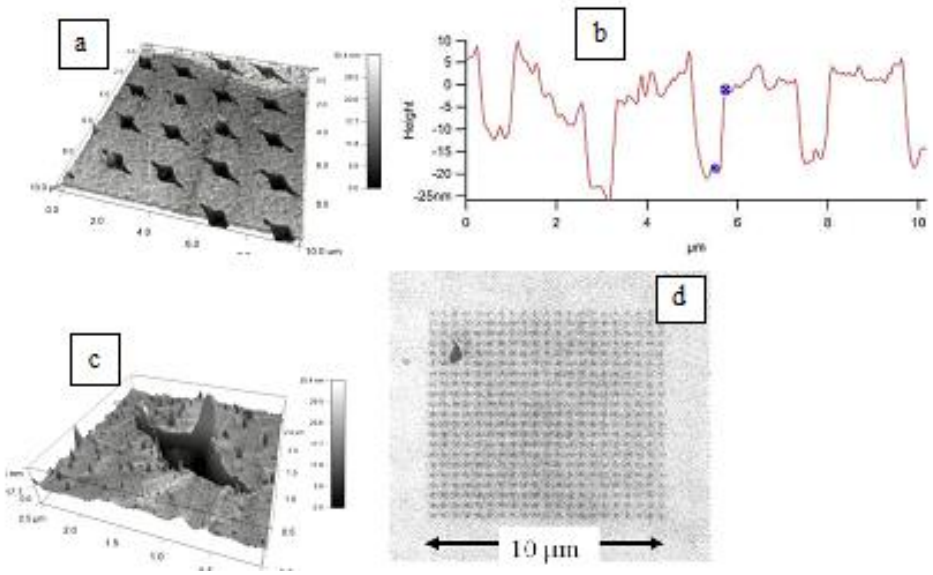

Fig. 1.32. (a) AFM image of a fragment of a 500×500 µm^2 nanodot array, which exhibited highest chemical sensitivity. The 700 nm nanodots were made at high ion dose. (b) Cross-section of the array surface showing profiles of nanodots. (c) Image of an individual nanodot. (d) FIB-written carbon nanodot array for chemical sensing applications.

The nanodots made with high ion doses were sputtered partially and had shape of pits, the depth of which depended on the dose. For the array shown in Fig. 3 the ion dose exceeds 10^{17} cm^{-2} and was high enough to sputter the diamond substrate to a depth of 15 nm.

Chemical sensitivity of the nanodot arrays was tested in a way analogous to that used for carbon nanowire arrays. Pairs of contact pads of silver paste were deposited on two opposite sides of the arrays and the current was measured between the contact pads at a bias varing from 1 to 30 V. Current-Voltage characteristics were superlinear implying injection character of the current flow. In general the nanodot structures revealed lower currents as compared with the nanowire structures of similar size. However, the chemical sensitivity was superior to that observed on the nanowire arrays. Typically the carbon nanodot structures showed an order of magnitude change of current when exposed to water vapor.

I.1.8. FIB-Written Single Electron Transistors

In the reporting year we developed a new approach of fabrication of single electron transistor structures on diamond surface with highly focused ion beams. Modern FIB instruments are powerful tool used for nanostructuring of various materials with ultimate accuracy of a few nanometers and high reproducibility. One of the novel directions in this research is the fabrication of conductive carbon nanowire-nanodot structures on insulating diamond substrates, which reveal highly non-linear behavior. We showed that these structures could operate as temperature and chemical nanosensors. The uniqueness of the combination of diamond material and FIB irradiation is the radiation-induced conversion of insulating diamond into conductive carbon under ion beam exposure with doses above a critical one, known as the graphitization dose. The dose dependence of this phase conversion is very steep and this peculiarity allows making graphitized areas considerably smaller that the nominal diameter of the ion beam. Fig. 1.33 shows an example of this effect where an ion beam with

nominal diameter of 700 nm can graphitize areas as small as 70 nm if the irradiation is performed at the threshold of the graphitization dose.

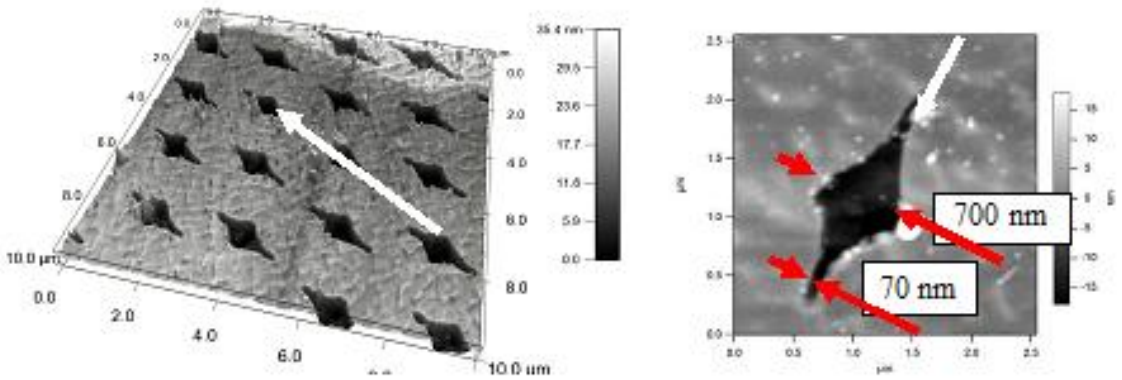

Fig. 1.33. (a) AFM image of graphitized areas on diamond surface irradiated with 2 nA focused ion beam scanned in pixel-like regime. The white arrow shows the direction of FIB scan. (b) AFM image of individual graphitized pixel. White arrows show the direction of beam scan. The exposure time during the scan is first increasing attaining maximum in the middle of the scan (the maximum width of the graphitized area) and then decreasing. The red arrows show the width of the graphitized area: 700 nm in the center (maximum exposure) and 70 nm at the beginning and the end of the scan where the exposure was minimum.

The FIB instrument Micrion 2500 installed in CSI can reproducibly generate ion beams with nominal focus down to 30 nm, what, in principle, allows graphitizing on diamond surface areas as small as a few nanometers in diameter. However, since Micrion 2500 is a single beam FIB tool, it is not suitable for fabrication of complex structures with ultimate accuracy. To do so, dual beam FIB systems must be utilized. The modern FIB instruments are capable of reproducible generation of ion beams with focus size down to 5 nm. These instruments are dual beam systems capable of ion beam nanostructuring with simultaneous monitoring of the fabrication process with electron beam working in SEM regime. Thus, using the dual beam FIB instruments, the size of the conductive graphitized areas on diamond substrates can be made as small as a few nanometers and the conductive areas can be placed in a predetermined position with accuracy of a few nanometers. In order to improve the conductivity contrast between the irradiated graphitized conductive and non-irradiated insulating diamond areas, additional metal deposition on the top of the graphitized areas can be done simultaneously with the irradiation.

In preliminary experiments performed with a Quanta 3D FEG DualBeam System at FEI company in Portland, Oregon, we have fabricated nanowire-nanodot structures using threshold graphitization with simultaneous platinum deposition on highly polished diamond substrates. The nanodots, as small as 10 nm, were placed between nanowire terminals (Fig. 1.34). The nanowires were made at an ion beam exposure twice exceeding the graphitization dose. The doses accumulated in the nanodots were slightly above the graphitization dose with little decrease in dose from (a) to (c). The effective size of the electrically conductive area of the nanodot depicted in (c) is expected to be below 10 nm.

These structures have been conceived as in-plane single-island single electron transistors capable of operation at room temperature. To our knowledge, this is the first demonstration of a reproducible fabrication of single-island single electron transistor structure with a resolution

of a few nanometers. Though the "visual" size of the nanowires and nanodots may seem quite big ranging in tens of nanometer, the actual size of conductive areas can be considerably lower. To prove it, the electrical conductance of the nanowires made of overlapping nanodots were fabricated and their conductance was measured as a function of the distance between the nanodots (Fig. 1.35).

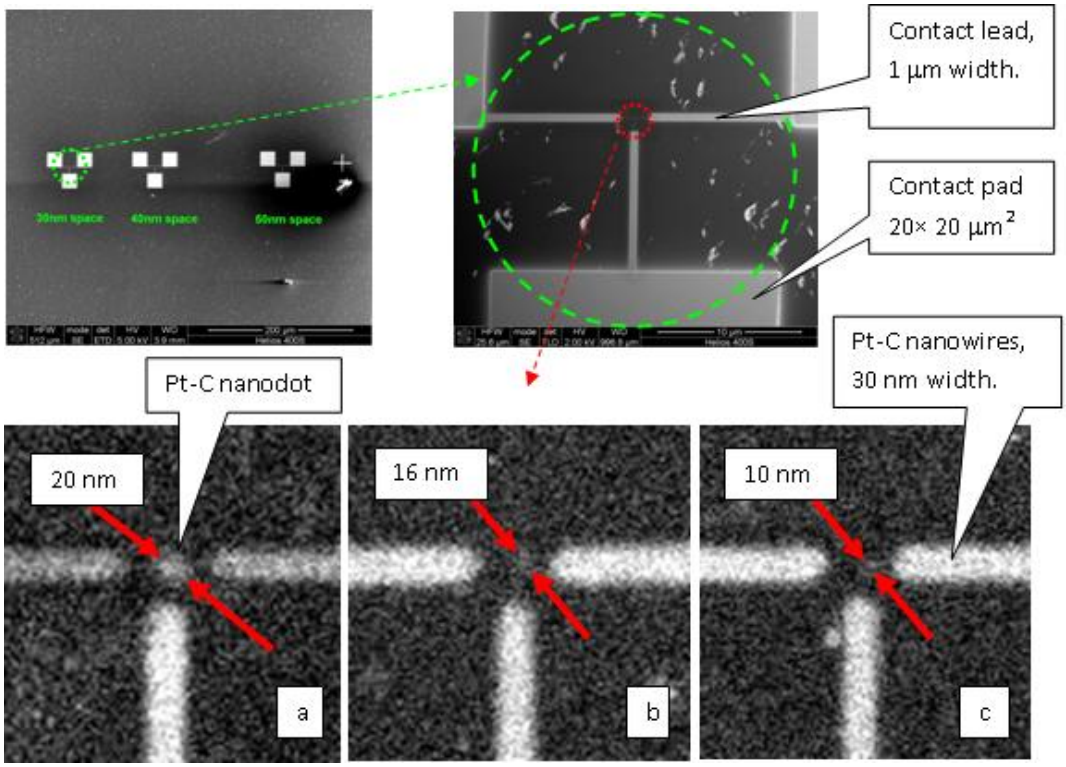

Fig. 1.34. SEM images of nanowire-nanodot single-electron transistors made on diamond surface with Quanta 3D FEG DualBeam instrument. The size of the graphitized and Pt covered areas as well as the ion beam currents used are: probe pads - 20 um x 20 um, 460 pA; leads - 10 um x 500 nm, 1.5 pA; nanowires - 1um x 30 nm, 1.5 pA. Three transistor structures were deposited with nominal spacing between the ends of nanowires and nanodot of 50, 40 and 30 nm.

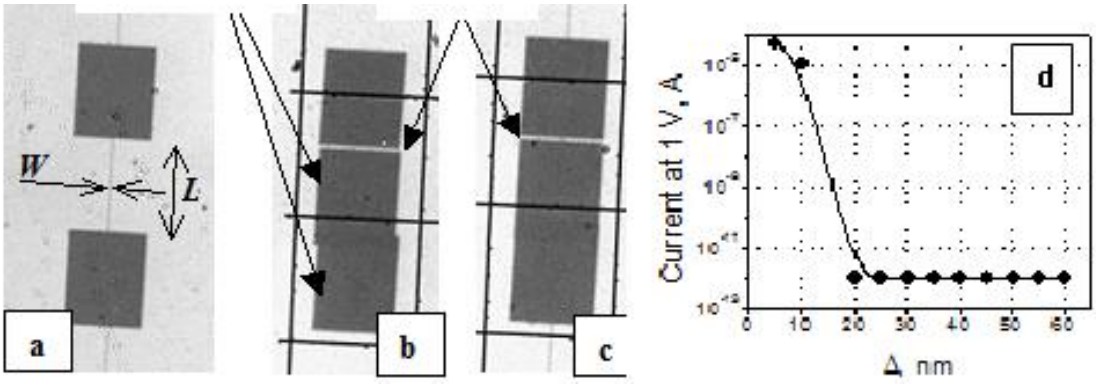

Fig. 1.35. (a) Schematic picture of a manowire made as a chain of nanodots attached to two rectangular electrical contact pads. (a) 10 micron long carbon naowire; (b) two contact

pads placed at a distance of 500 nm; (c) short carbon nanowire of a length of 500 nm. (d) Room temperature conductance of a nanowire made of separate carbon nanodots versus the distance Δ between the nanodots.

It has been found that though the "visual" width of the nanowire ("visual" diameter of the nanodots) was about 80 nm, the ohmic conductance in the nanowire appeared when the distance between the nanodots was 10 nm and below (Fig. 1.35d). Thus we believe that the size of the electrically active nanodot does not exceed 10 nm.

I.2. Carbon Nanofilms on Diamond Surface

Temperature and chemical sensors have widespread applications in industry and scientific research. Though there are varieties of effective temperature sensors available, realization of selective and practical chemical sensors is still an area of hot pursuit. This encourages the exploration of novel sensing materials and design of sophisticated sensor structures. Recent developments in nanotechnology have helped considerably in achieving these objectives. Mainly, metal-oxides [10], conducting polymers [11], carbon nanotubes (CNTs) [12-20] and their composites [21-23] have been tried for chemical sensing applications. Metal-oxide based sensors have been known for a long time. They are particularly successful in detecting different gases/vapors at a sub-ppm concentration with reasonable stability. However, their high operating temperature (over 300°C) poses a serious restriction on their employability. In contrast, the sensors, which are based on conducting polymers and carbon nanotubes, work at room temperature. They also provide additional benefit of modification of the active material to help to achieve chemical selectivity [24-26]. The main drawback with the use of conducting polymers is their low response and low stability. Concerning carbon nanotubes, their ability to detect sub-ppm concentrations of gases is remarkable. However, the recovery time of the carbon nanotube based sensors has been found to be very long (~10 hours) and, in order to reduce this time, a special procedures (e.g. ultraviolet light illumination) are required [19]. It may also be noted that only single wall carbon nanotubes (SWNTs): individual [12] and thin films [15-20]; perform reasonably well. Additionally, performance will depend upon type of SWNT, which may be metallic, or semiconducting depending on their geometry [27], with semiconducting SWNT showing greater response [15, 19]. Response from a SWNT film is averaged over different types of tubes present and is hence lower. MWNTs show much lower response and have been tried as composites with metal oxides and polymers [21-23]. Thus, technological hurdle imposed by the difficulty in obtaining pure SWNTs of desired geometry and the long recovery time are the challenges still to be met on the way of development of effective gas sensors based on carbon nanotubes.

Carbon nanowires made on diamond by focused ion beam (FIB) have been reported as alternative to CNT based sensors [30, 31]. It has been previously shown that the FIB irradiation of diamond surface is a flexible and reproducible technology of fabrication of two-dimensional structures composed of conductive carbon nanowires and nanodots [28, 29]. However, high cost of the FIB-based technology may be a disadvantage preventing from commercial application of the FIB-written carbon nanosensors. More recently, graphene, a 2-D form of carbon; has also been shown to perform well for even sub-ppm level detection of different gases [33, 34]. However, utilization of graphene as sensing material faces similar challenges as faced by its application in other areas; viz. large area graphene synthesis, stability and purity.

Like other nanomaterials, carbon nanofilms provide advantage of having large active surface area to volume ratio, which is one of the reasons for CNTs/carbon nanowires to perform as gas sensing material. In this respect, amorphous conductive carbon nanofilms which lack order in their material structure can be useful for sensor application for their easy preparation. This is especially true, if exact reproducibility of the sensor devices is not sought. Amorphous carbon film based ammonia sensors and moisture sensitive sodium or potassium doped carbon films were previously reported [35-39]. However, not much attention has been paid to carbon films as sensor material for other vapors or gases. Among numerous methods available to synthesize conductive amorphous carbon films, graphitization of diamond surface at high temperatures is of special interest [30-42]. The as-grown carbon films on diamond can further be etched by plasma etching to obtain desired chemical sensitivity. This provides a unique natural combination of two carbon materials with complementary electronic properties: conductive amorphous carbon nanofilm and perfectly insulating diamond substrate. Thus carbon nanofilm on diamond may be considered as a natural basis for development of all-carbon sensors, which could be promising for biological and medical applications. Here, we are reporting the results of study on temperature and chemical sensing properties of carbon nanofilms on diamond.

I.2.1. Preparation of Carbon Films on Diamond Surface

Superior chemical sensitivity of the nanodot structures has lead us to development of a more practical method of fabrication of carbon nanodot structures on diamond surface. The FIB irradiation, though being very controllable and precise, is an expensive method and, because of this, not very practical.

A novel method of fabrication of carbon nanodot arrays on diamond surface without application of FIB irradiation was proposed. The idea was to graphitize thin layer of diamond surface by heating it at high temperature in vacuum with subsequent partial removal of the formed graphitic layer in an oxygen-containing plasma. Important, that the diamond surface in this case must be not very smooth but possess some moderate roughness in the range of 20 to 100 nm. In this case the graphitized surface is not flat but has a shape of corrugated sheet. When exposed to plasma such a layer will be etched away nonuniformly because of the different orientation of its surface with respect to the plasma discharge. This way an irregular pattern of graphitic (amorphous carbon) islands of nanoscale size can be formed over the whole sample surface (Fig. 2.1).

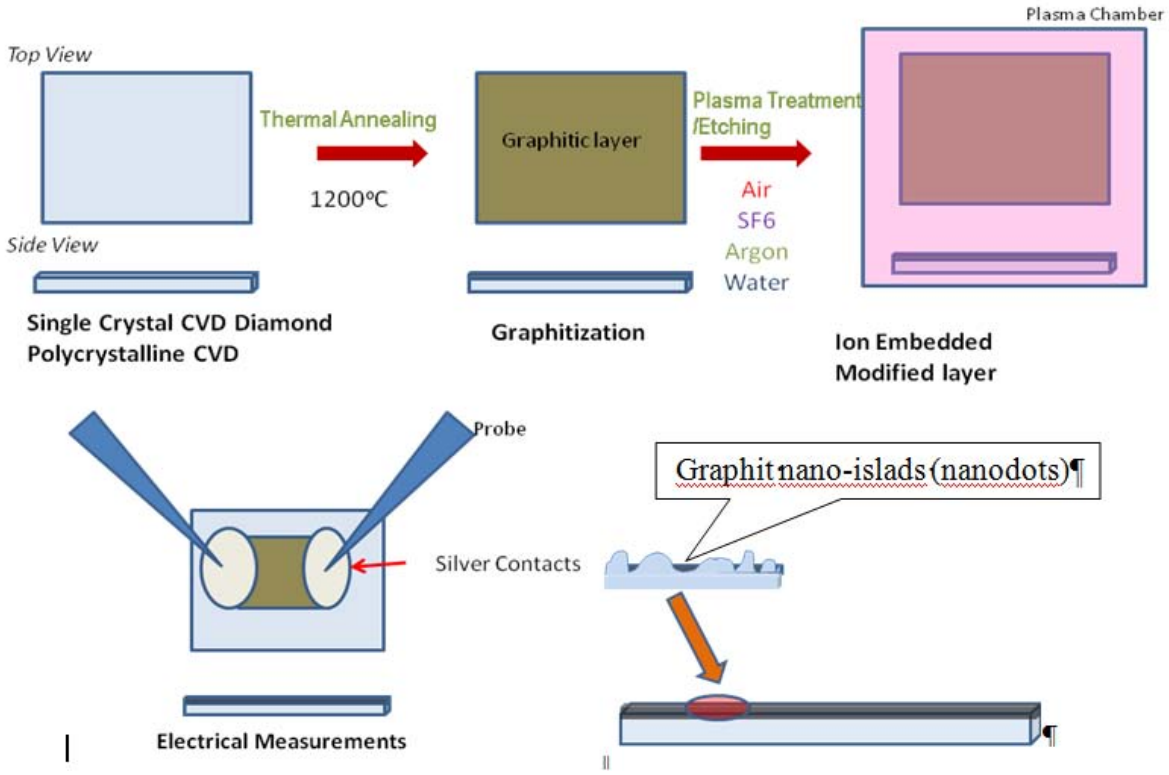

Fig. 2.1. Procedure of fabrication of random arrays of carbon nanodots on diamond surface using using high temperature graphitization followed by oxygen plasma etching. Varying the thickness of the graphitized layer and the plasma etching rate and time one can well control the average size of the graphitic nano-islands and separation between them.

The surface graphitization of the diamond samples was performed by heating at temperatures in the range from 1100 to 1400C in vacuum ranging from 10^{-6} to 10^{-1} mbar. The higher the temperature and the lower the vacuum the thicker was the graphitized film. The thickness of the graphitic layer might vary from a few nanometers (when grown in a high vacuum at a temperature below 1200C) to a few hundred nanometers (when grown in low vacuum at a temperature of 1400C).

Carbon nanofilms were grown on diamond samples using high temperature annealing in vacuum or inert atmosphere. Polished, optical grade single crystal and polycrystalline diamond plates of size 2.5×2.5×0.5 mm^3 grown by chemical vapor deposition were used for this purpose (supplied by Element6). Initial surface roughness of the samples was below 30 nm (specification of Element6). The crystallographic orientation of the surfaces of the single crystal samples was (100). Before annealing, the diamond samples were ultrasonically cleaned in acetone. Annealing was performed in steps at different temperatures in the range 700 - 1400°C for 10–30 minutes at each step. At temperatures above 1000°C, a conductive gray film of carbon started to form on the sample surface.

Vacuum annealing was performed at two different levels: about 3×10^{-5} mbar and 3×10^{-2} mbar, which we further refer as high vacuum (HV) and low vacuum (LV). For the annealing in gaseous atmospheres, a Sentronic furnace with horizontal alumina tube was used. Inert atmospheres were produced by purging the tube with ultrapure argon or nitrogen at a flow rate of 1 L/min. The growth of carbon nanofilms was monitored by of in-situ electrical conductance measurements using specially designed and fabricated high temperature ceramic sample holder with self-adjusting graphite electrodes (Fig. 2.2).

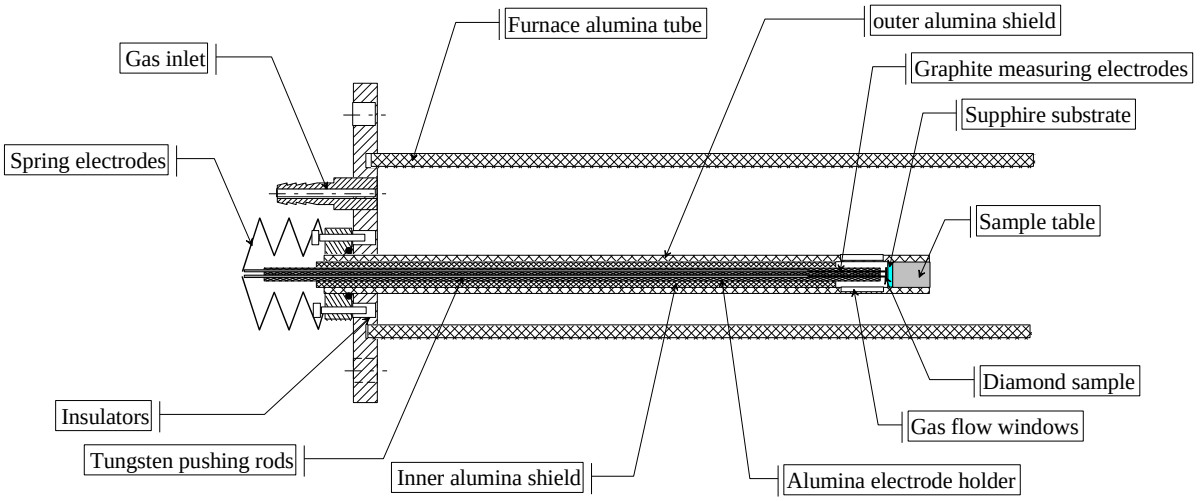

Fig. 2.2. Design of ceramic holder with self-adjusting graphite electrodes for in-situ electrical measurements of carbon nanofilms growing at high temperatures.

The ceramic holder was thoroughly tested for leakage currents at high temperatures. It was found that at all growth temperatures the leakage currents were at least three orders of magnitude below the currents induced in measured diamond samples. Thus the leakage currents did not affect the measurement results.

I.2.2 Growth Temperature

Fig. 2.3 shows surface conductance of a diamond sample on successive steps of high vacuum annealing at different temperatures. Some samples showed a considerable increase in conductance after annealing at temperatures below 800°C and a decrease after annealing at higher temperatures. The origin of this increase is still not clear. However, since it is sample dependent, it cannot be ascribed to surface graphitization. A sharp irreversible rise in conductance at around 1000°C observed on all samples indicates the onset of conversion. The conductance rapidly increases with further temperature increase. A visibly light gray film of fairly high conductance is obtained after annealing at 1300°C.

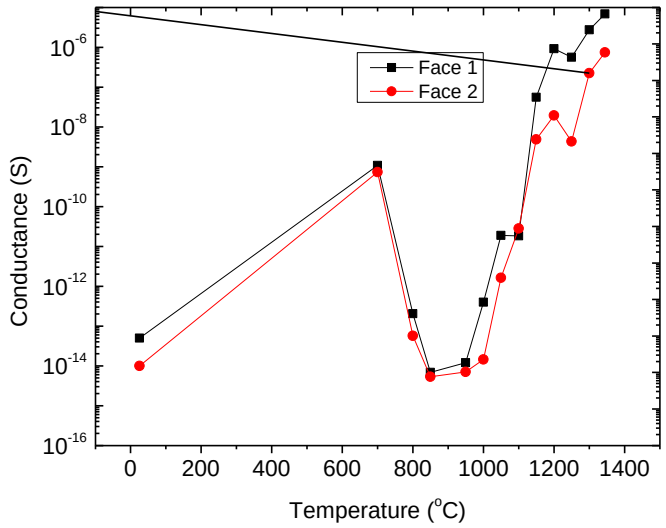

Fig. 2.3. Room temperature surface conductance of two faces of a diamond single crystal plate on successive annealing steps at different temperatures in high vacuum. The sample was annealed for 15 minutes at each temperature.

In order to find the temperature of the onset of the surface conversion in inert gas, in-situ measurements of the surface conductance were performed in the Sentronic furnace filled with nitrogen. Fig. 2.4 shows the change in conductance of single crystal diamond samples during heating and subsequent cooling. It can be clearly seen that the conductance induced by heating at a temperature of 1000°C and above is stable and retains after cooling. All curves exhibit also a broad conductivity maximum at temperatures 600 - 700°C, which, we believe, is of the same origin as that shown in Fig. 2.3.

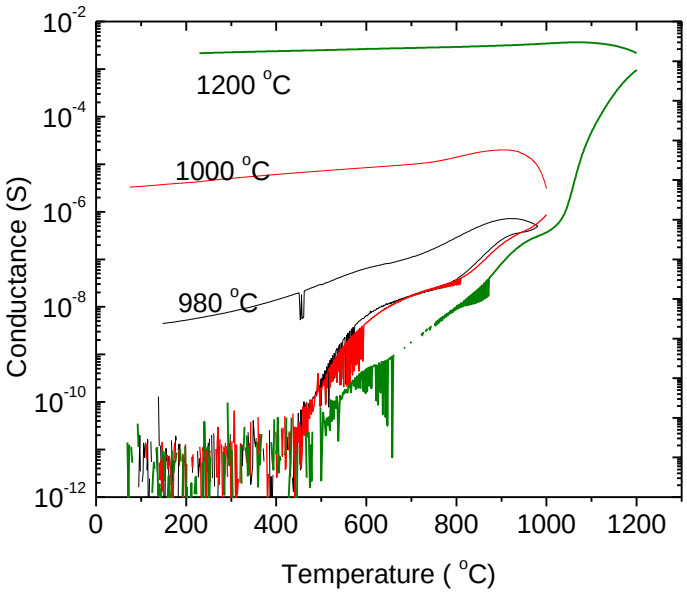

Fig. 2.4. In-situ measurement of surface conductance of diamond samples during the processes of heating and cooling in N_2 atmosphere with different maximum temperatures (indicated on the graph). For each process, the samples were kept at the maximum temperature for 15 minutes. Rate of cooling/heating was 5°C/min.

In order to verify the continuous growth of the graphitized layer at maximum temperature, an experiment was run to the maximum temperature of 990°C with a prolonged hold at this temperature for 3 hours. The results are presented below in Fig. 2.5 and 2.6.

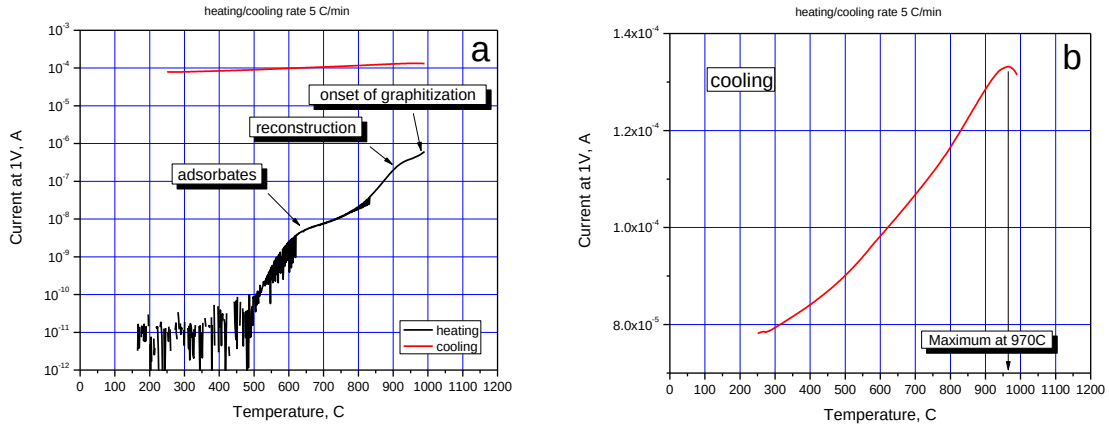

Fig. 2.5. (a) Electrical conductance of (100) diamond surface during heating/cooling processes at a rate of 5 °C/min. Two steps of the conductance increase due to adsorbates and reconstruction is clearly seen. (b) The conductance dependence during cooling presented in linear scale exhibits maximum at 970°C, which is the temperature of the graphitization onset.

The conductance during the temperature growth revealed pronounced increases at 500-600°C and 800-900°C and the onset of the third increase due to graphitization at temperatures above 970°C (Fig. 2.5a). During the holding at 990°C, the conductance increased first exponentially with time for about 30 minutes and then linearly (Fig. 2.6). The exponential growth of the conductance could be an artifact because of a still slightly growing temperature at the sample. The linear increase shows that the thickness of the conductive layer grew uniformly with time. During the cooling, the conductance continued to increase with the temperature drop down to 970°C and then gradually decreased.

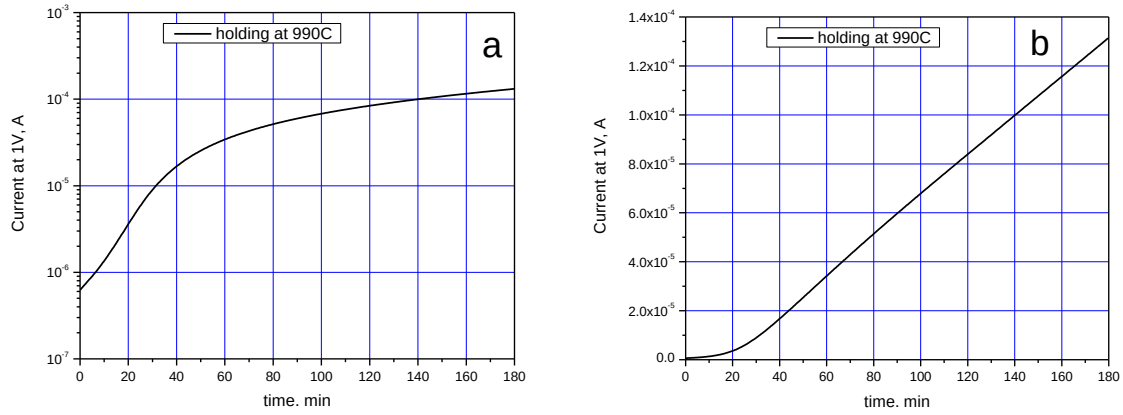

Fig. 2.6. Conductance of the graphitized diamond surface during holding at temperature 990°C for 3 hours presented in logarithmic (a) and linear (b) scales. During first 30 minutes the film exhibited exponential increase in conductance; afterwards the conductance increase versus temperature became linear.

The temperature of 970°C for the graphitization onset has been fairly well described theoretically as the temperature where the driving force of the graphitization and the height of the energy barrier of conversion of diamond into graphite attain equal values (see below the theoretical part).

I.2.3 AFM and Electrical Characterization

Sheet conductance of thin films grown in high vacuum at temperature 1200°C for 15 min varied in the range 10^{-5} - 10^{-4} S. Thick films obtained in low vacuum showed conductance in the range 10^{-4} - 10^{-3} S. The conductance of the carbon films was also found to be influenced by the quality/type of the diamond samples. The films obtained on polycrystalline diamonds showed lower conductance at about 10^{-6} S.

The thickness of the films grown at temperature 1200ºC for 30 minutes in high vacuum was found to be about 10 nm, while that obtained at the same conditions but in low vacuum was about 100 nm (Fig. 2.7). Taking into account these thicknesses, specific resistivity of the films was calculated to be in the range 10^{-3}–10^{-4} Ωm. This value, much higher than that of graphite (8×10^{-6}–15×10^{-6} Ωm), indicates the amorphous/discontinuous nature of the films.

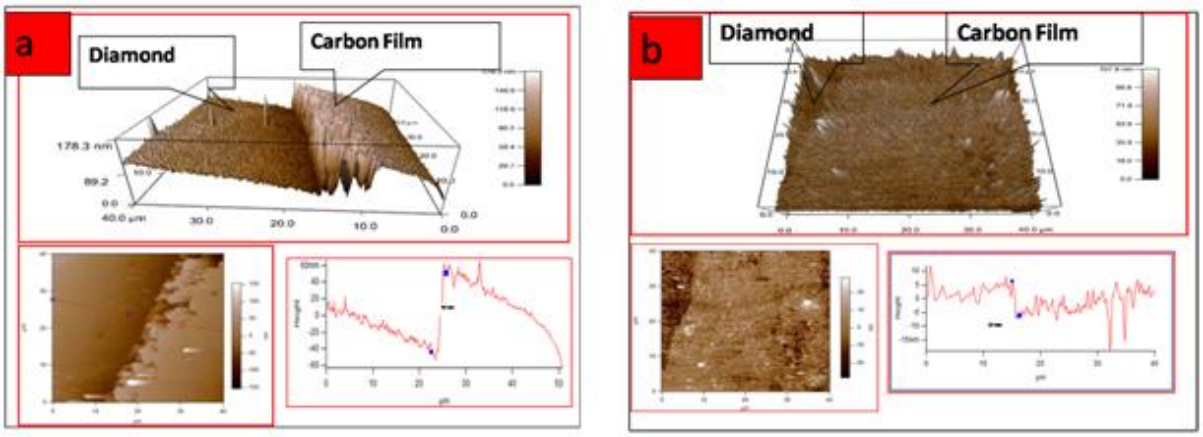

Fig. 2.7. AFM image (tapping mode) of edge of the carbon films grown on diamond surface by heating at 1200°C for 15 min in (a) low vacuum, and (b) high vacuum. Surface profiles are taken along the red lines shown on images.

The change in conductance of the carbon nanofilms exposed to plasma etching is shown in Fig.2.8. Plasma etching reduces conductance implying partial removal of conductive carbon. The change in conductance of thick films, grown in low vacuum, exhibits two distinctive regions. At the initial stages of etching (Region I), the conductance drops linearly with etching time, and then it reduces exponentially (Region II). A residual conductance is observed in the end on prolonged exposure (Region (III). Thin films, grown in high vacuum, show the exponential drop of conductance from the very beginning of the etching (Fig. 2.8c).

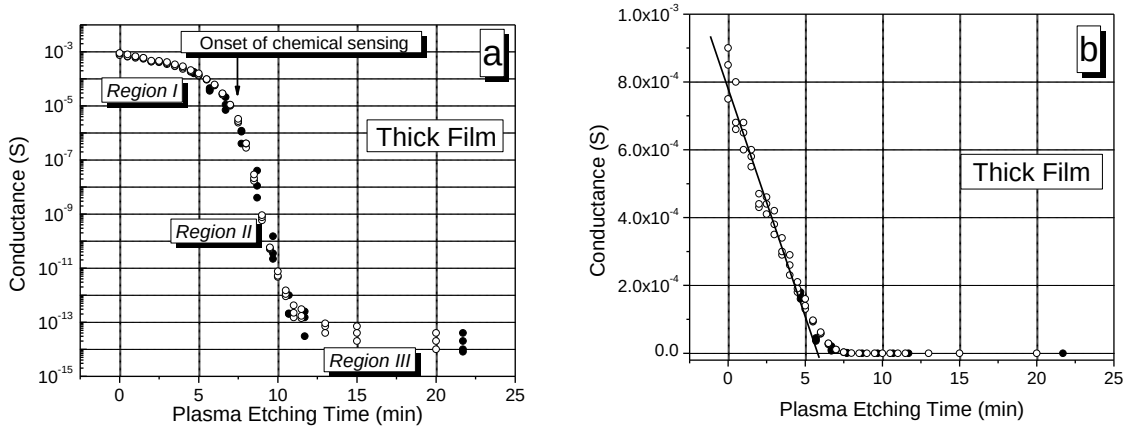

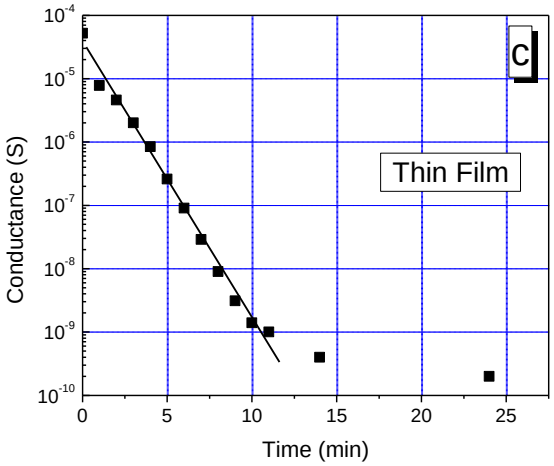

Fig. 2.8. Change in conductance of the carbon films on diamond surface versus time of treatment in air plasma: (a, b) thick film, (c) thin film. Thick film exhibits linear decrease in conduction at the initial stages of etching and exponential afterwards, whereas thin film shows exponential decrease from the very beginning of etching. The reduction of conductance of thick film is shown both in logarithmic (a) and linear (b) scales to highlight the ranges of exponential and linear drops.

The decrease in conductance with time of plasma etching is attributed to successive removal of the conductive layer from diamond surface. We speculate that after the film was largely removed, there might have been some conductive carbon still trapped between the surface features as also indicated by a residual surface conductance, resulting into formation of a random array of isolated carbon nanodots (Fig. 2.9).

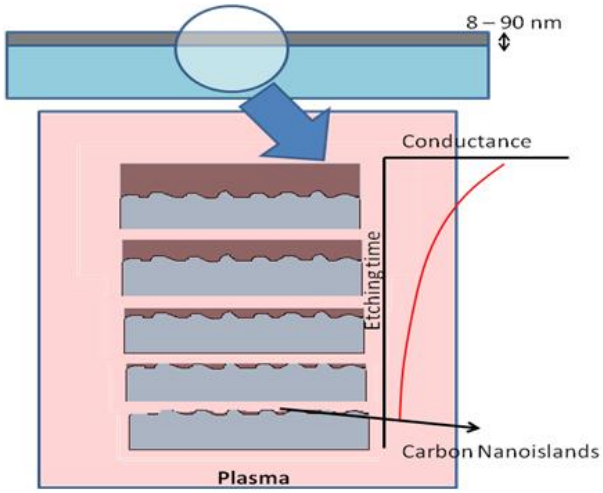

Fig. 2.9. Cartoon depicting the transformation of carbon film on diamond surface during exposure to plasma. A discontinuous random array of carbon nanoislands on diamond surface is assumed to be formed after prolonged exposure.

I.2.4 Raman Characterization

In order to gain more insight into nature of the carbon nanofilms grown on diamond surface, Raman spectra were measured on as-graphitized diamond surface and after successive plasma etching (Fig. 2.10). The characteristic D and G bands at wavenumbers 1350 and 1590 cm^{-1} indicate the presence of amorphous carbon. As the films are etched by plasma and their thickness decreases, both bands become broader and shift one towards

another eventually merging into one weak broad band at a wavenumber of 1450 nm. We speculate that with plasma etching, the carbon nanofilms become increasingly amorphous.

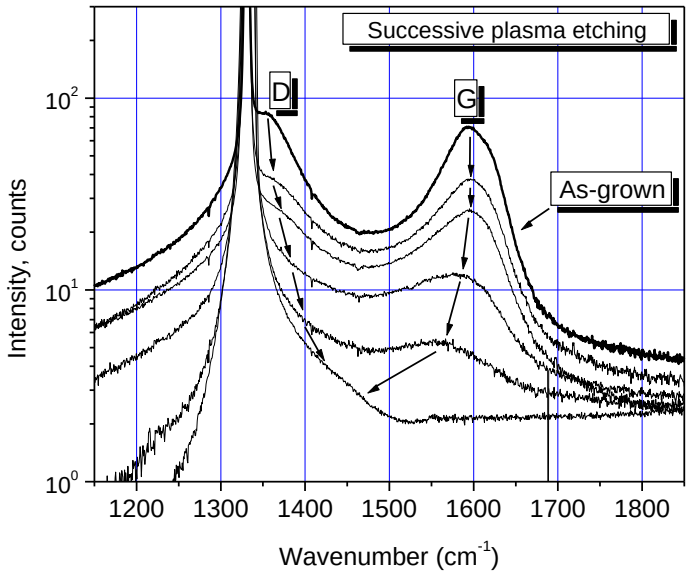

Fig. 2.10. Raman spectra of thin carbon nanofilm as-grown and after several steps of successive plasma etching. Each etching step was about 1 minute.

I.2.5. Temperature Sensitivity

Conductance of the carbon nanofilms of varying thicknesses, obtained by plasma etching, was studied for its temperature sensitivity Fig. 2.11. The conductance of all films increased with heating with no permanent change in conductance. The magnitude of the temperature-induced increase in conductance depended considerably on the film thickness. The conductance of as-grown thick films remained high and almost temperature independent, while that of the as-grown thin film was lower and showed slight increase with temperature. Depending on the plasma power, it may take up to 30 minutes of plasma exposure to reduce the conductance of the thick film by three orders of magnitude and thus to make it comparable with that of the as-grown thin films. The plasma etched thick film was found to be nearly as sensitive to temperature as the as-grown thin film. The etched thin film (1.5 min of plasma exposure) showed nearly 3 times increase in conductance on heating from room temperature (0.18 μS) to 150ºC (0.43 μS). Further etching for another 1.5 min causes further reduction the overall conductance level and increase in the temperature sensitivity. On continued etching, the conductance was lowered down to 10^{-10} S and its temperature change raised to one order of magnitude.

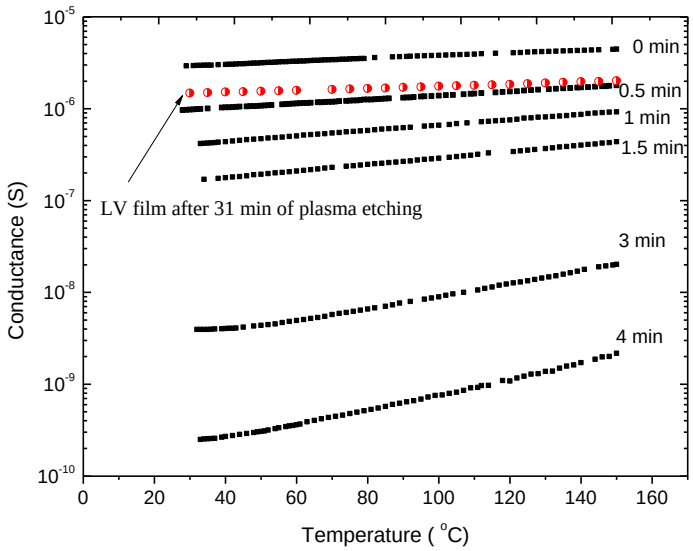

Fig. 2.11. Temperature dependence of conductance of a thin carbon nanofilm: as-gown (upper curve) and after plasma etching for times indicated in the graph. Change in conductance of a thick carbon film after 31 min of plasma etching is also included for comparison (red curve).

The temperature sensitivity was examined in terms of the models of the temperature activation via energy barrier E_a, and variable range hopping [44-48]. The temperature activation via energy barrier is approximated by simple dependence:

$$G(T) = G_o \exp(-E_a/kT), \quad (1)$$

where T is the absolute temperature, k is the Boltzmann constant, E_a is the activation energy and G_o is a constant. The conductance shows increasingly exponential dependence as film is etched by plasma. However, for very thin films, the observed trend significantly deviates from the exponential dependence over the temperature range (Fig. 2.12a). Empirically, this deviation may be described by the change in activation energy with temperature. Fig. 2.12b shows that for plasma etched films the activation energy changes almost exponentially on heating, while it remains almost constant for as-grown films.

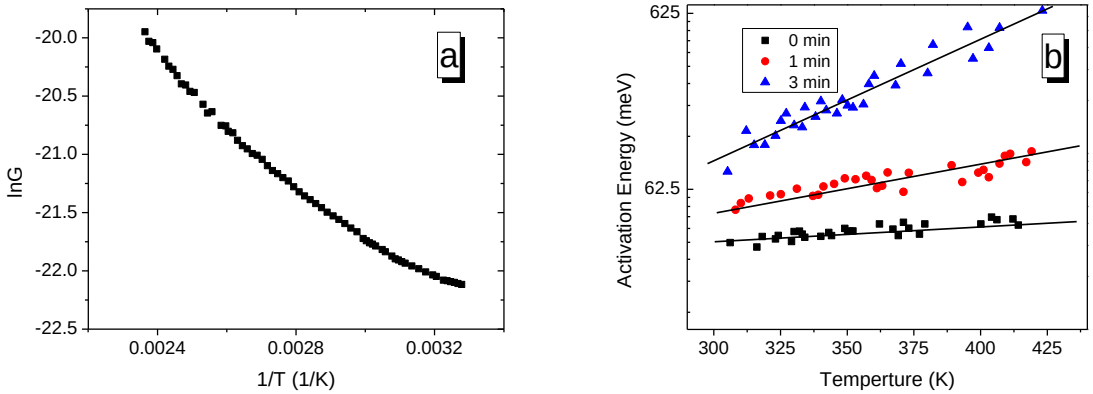

Fig. 2.12. (a) Logarithm of conductance of a plasma etched thin carbon nanofilm (4 min of plasma etching at a moderate power level) as a function of T^{-1}. (b) Temperature dependence of activation energy for as-grown thin film and plasma etched films. The dependence is increasingly exponential on plasma etching (increased slope of best-fit line on logarithmic scale).

The simulation of the temperature sensitivity based on the Variable-Range-Hopping model has been performed using the relation:

$$G(T) = G_o \exp(-T_o/T)^{1/4}, \quad (2)$$

where T_o is the hopping temperature and G_o is the conductance prefactor. However, when we plot conductance G on logarithmic scale vs. $T^{-1/4}$, there is only minor improvement in the fit over the simple form given by [Eq. 2], at least for the very thin films (Fig. 2.13a). Thus, the mechanism of charge transfer via hopping through the random nanoislands doesn't apply here very well.

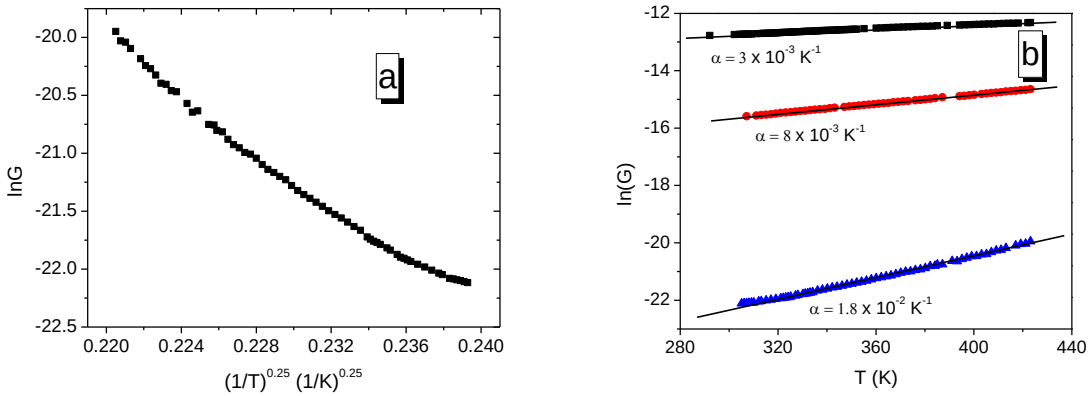

Fig. 2.13. (a) - Logarithm of conductance of a thin plasma etched film as a function of $T^{-1/4}$. (b) –Comparison of temperature dependences of conductance of as-grown, intermediate and thin plasma etched films as a function of T. The intermediate and thin plasma etched films were obtained by 1.5 min and 4 min plasma etching respectively.

Instead, we found that the temperature change in conductance shows the best fit when simulated by dependence:

$$G(T) = G_o \exp(\alpha T), \quad (3)$$

where α is an empirical constant (slope of the best fit line), which increases on plasma thinning, for both as-grown and plasma etched films (Fig. 9b). Same dependence was observed on carbon nanostructures made on diamond surface by irradiation with focused ion beam. More studies are needed to understand this particular behavior.

I.2.6 Chemical Sensitivity

Chemical sensitivity of carbon nanofilms was measured in a home-made chamber, which allowed to measure resistance of the films when exposing them to a gas atmosphere of a set composition. In the present communication, the response of the carbon films to a mixture of an inert gas with water and acetone vapors is discussed. The water and acetone vapors were produced by bubbling dry nitrogen/argon gas through the respective liquids. The vapors were further diluted by mixing with another flow of dry nitrogen/argon gas at different flow rates in order to vary the vapor concentration. The concentration ranges were thus limited by the vapor pressure of acetone and water at room temperature. The vapors were introduced into the measuring chamber with the carbon film in pulses of 100 seconds duration. A constant total gas flow (inert gas + vapor) of about 800 mL/min was maintained throughout. The chamber was purged with pure dry inert gas for about 10 min prior to the start of the measurements.

Thin carbon nanofilms, and especially those obtained after plasma etching, revealed appreciable chemical sensitivity for different gaseous analytes. Fig. 2.14 shows the response transients and sensitivity (the relative change in conductance; $\Delta G/G_o$) of plasma etched films on exposure to varying concentrations of water and acetone vapors. The films with different levels of conductance are compared. Response to water steadily increases with increase in the water vapor concentration (Fig. 2.14a, 2.14c). The sensitivity of as-grown film to water vapor is only 0.1 at the maximum vapor concentration (1.5%). However, after plasma etching, the sensitivity of the film to the same vapor concentration increases to 2.5.

Response to acetone vapor is different as compared to water (Fig. 2.14b, 2.14d). Firstly, it is much less than that to water. Acetone could produce same sensitivity of 2.5 only at a vapor concentration of 14%. Secondly, thick films revealed almost constant sensitivity of 0.02 independent of the acetone vapor concentration. Thirdly, sensitivity of thin plasma etched films was not monotonous and exhibited a maximum at a certain vapor concentration (Fig. 2.14d).

The recovery time of the film conductance after the supply of the analyte vapor into the chamber has been shut down was about 1 minute. Though the reported results are for acetone and water vapors, we have found similar response and recovery time for vapors of alcohol, NO_2 and NH_3. Such a sort recovery time is remarkable when compared to that of carbon nanotubes, which may be as long as 10 hours and an ultraviolet illumination is required to decrease it to a few minutes [27].

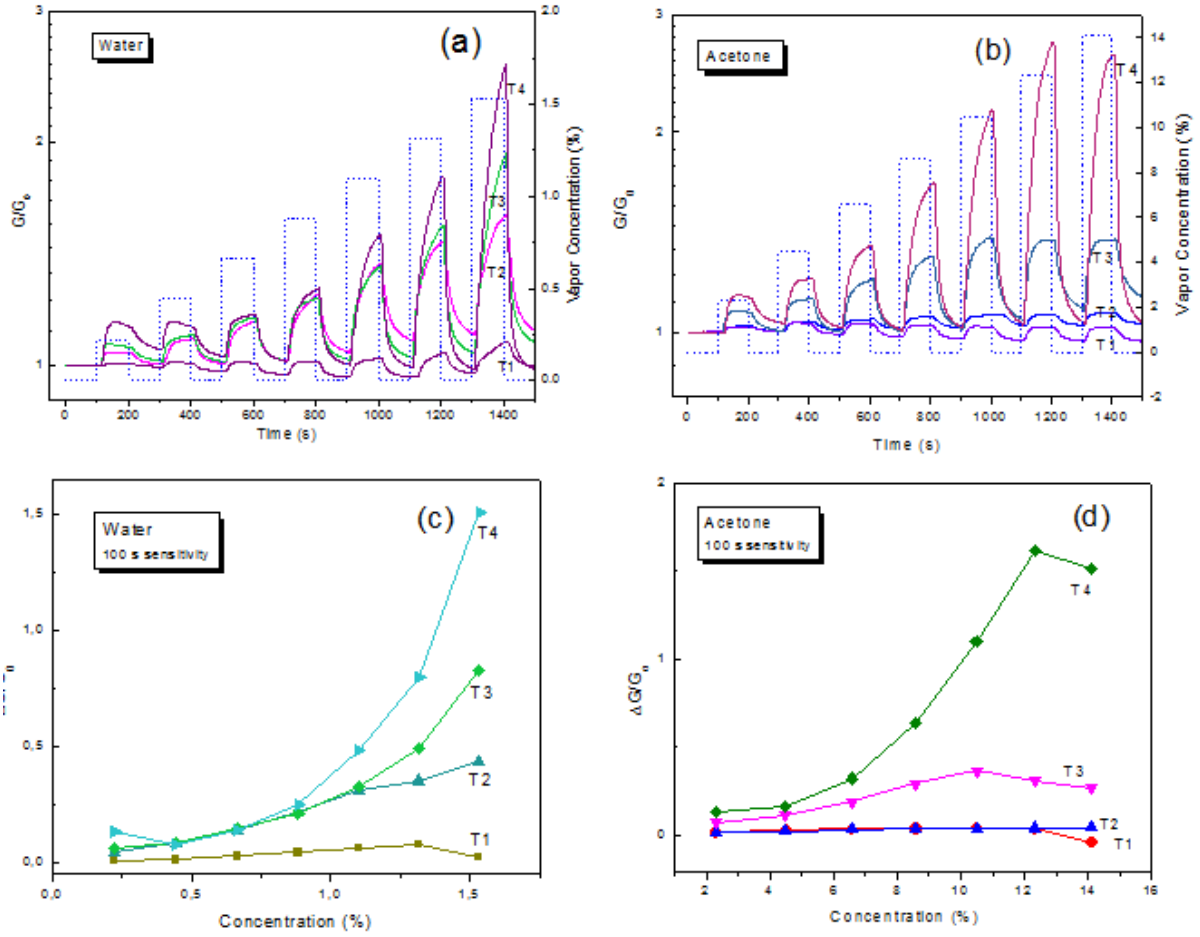

Fig. 2.14. Response of plasma etched carbon films on diamond, on exposure to varying concentrations of water and acetone vapors in dry argon gas. Response transients for vapors

of (a) water and; (b) argon. Relative sensitivity at the end of 100 s exposure to vapors of (c) water and; (d) acetone. Curves T1, T2, T3 and T4 correspond to the films with conductance 2.1 x 10^{-7}S, 1.9 x 10^{-8} S, 1.9 x 10^{-9} S and 3.1 x 10^{-10} S respectively; obtained by successive plasma etching. The dotted line shows the concentration cycles of analytes injected into measuring chamber with 100 s duration pulses.

Chemical sensitivity of carbon nanofilms treated by plasma etching increases with time of etching and, concequently, with reduction of the film conductivity considerably. Fig. 2.15 shows that the decrease of the film conductance from by 6 orders of magnitude results in the increase of chemical response by two orders of magnitude.

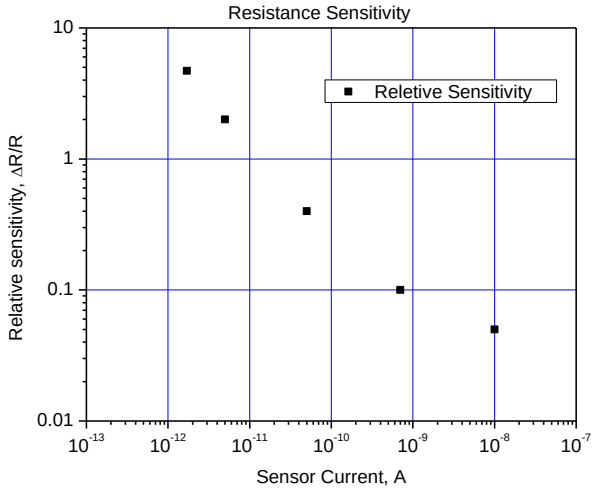

Fig. 2.15. Relative chemical sensitivity of thin carbon nanofilms grown in N_2 atmosphere at a temperature of 1000ºC versus their conductance.

Chemical sensitivity of some carbon nanofilms grown in gaseous atmospheres can be very high considerably exceeding their temperature sensitivity. As a result, these films may have pronounced negative response to temperature when measured in open air with high level of humidity (Fig. 2.16).

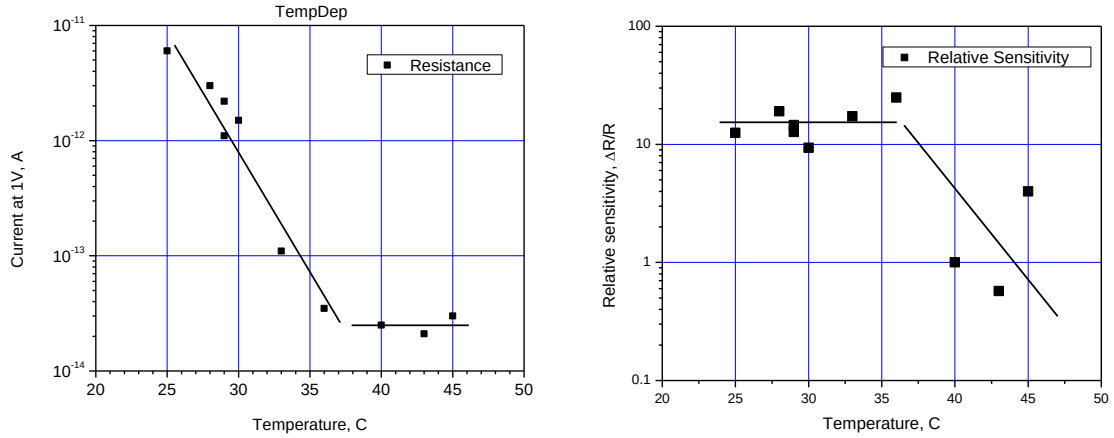

Fig. 2.16. Conductance (a) and relative chemical sensitivity (b) of highly chemically sensitive carbon nanofilms with temperature.

This effect is explained by evaporation of the water adsorbate from the films surface at elevated temperatures (in this case at temperatures over 35ºC). Since these films have strong positive response to water vapor, the removal of water from their surface causes considerable decrease in conductance. The temperature point at which the complete removal of the water adsorbate occurs is clearly seen on the sensitivity-temperature dependence (Fig. 2.16b): to a temperature of 35ºC the relative response remains constant and at higher temperatures it deceases drastically.

Since the physical size of the carbon nanofilm chemical sensors can be very small (ultimately down to a few tens of nanometers), they can be used for the measurements of small objects. As an example, we measured relative density of water vapor surrounding a water droplet of a diameter of 1 mm using a carbon nanofilm sensor with an active area of a size of 100 microns. The water droplet was placed on the tip of a needle of micromanipulator and was moved precisely around the sensor. The sensor response, as a water droplet is approached and withdrawn, is shown in Fig. 2.17.

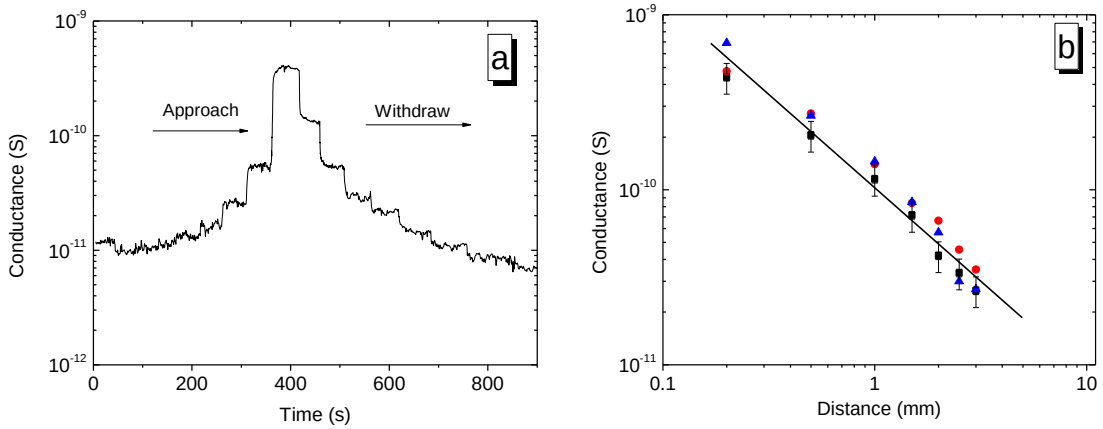

Fig. 2.17. (a) Change in conductance of a thin carbon nanofilm as a 1 mm diameter droplet of water is approaching and withdrawing the film in steps. The maximum distance is about 10 mm (the lowest conductance), and the minimum distance is a fraction of millimeter (maximum conductance). (b) The conductance of a thin carbon nanofilm versus distance between the water droplet and the carbon nanofilm sensor. The conductance increase is inversely proportional to the distance.

The conductance of the films remained ohmic at different levels of exposure to chemical analytes. Fig. 2.18 shows that the linear current-voltage characteristic of a carbon film does not alter as it is exposed to water vapor produced by a water droplet bought to the film surface at distances from 0.1 to 8 mm. This observation shows that the analyte vapor adsorbed of the carbon nanofilm surface does not form any energy barriers, which could result in current injection and non-linear current-voltage characteristics. Instead, the analyte molecules just increase/reduce concentration of charge carriers in the film. This behavior resembles the performance of a chemical field-effect transistor where the controlling gate voltage is created by the molecules adsorbed on the surface of conductive channel.

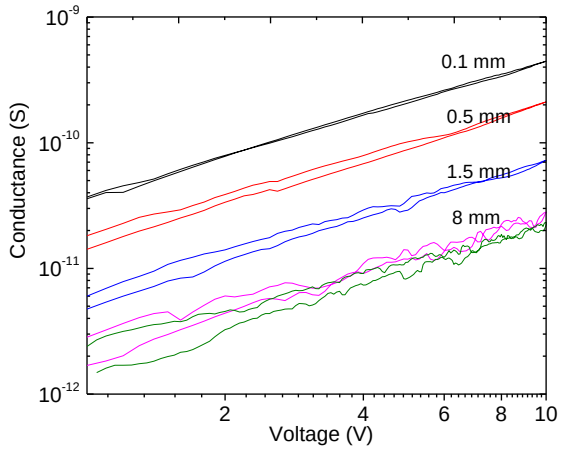

Fig. 2.18. Current-Voltage characteristics of a thin carbon nanofilm in the presence of a 1 mm diameter water droplet placed at distances specified.

Unlike thermal sensitivity, which results from the thermal activation of the charge carriers, chemical sensitivity is based on chemical modulation in the conductance at the surface. Though, the exact mechanism of this effect is still not clear, obviously the conductance change starts with the adsorption of analyte molecules at the film's surface (Fig. 2.19).

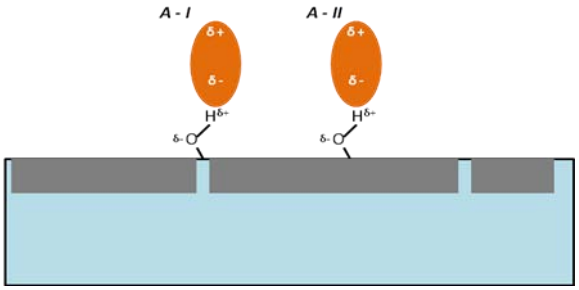

Fig. 2.19. Adsorption of dipolar molecules on a diamond surface containing plasma-etched carbon nanofilms, at different adsorption sites. A-I: Adsorption at the bare diamond surface separating conductive carbon structures, A-II: Adsorption at the area containing conductive carbon.

The sensitivity would then depend upon extent and nature of the molecular interaction with the film's surface. Observed higher response to water indicates greater interaction of water molecules with the surface probably through hydrogen bonding with surface sites containing groups like hydroxyl. On oxygen plasma etching (a known technique for modification of different carbon surfaces [51-56]), additional adsorption sites may be introduced on the surface. This causes an increase in the number of interacting molecules and enhancement of sensitivity. The as-grown films, which do not have enough coverage of adsorption sites show almost constant sensitivity on increase in water vapor concentration, whereas, etched films show almost exponential behavior (Fig. 2.20). In contrast, sensitivity to acetone, which does not form hydrogen bonds, is much lower. Also, unlike water, acetone does not cause the exponential increase on increasing vapor concentration at least for the intermediate plasma etched films.

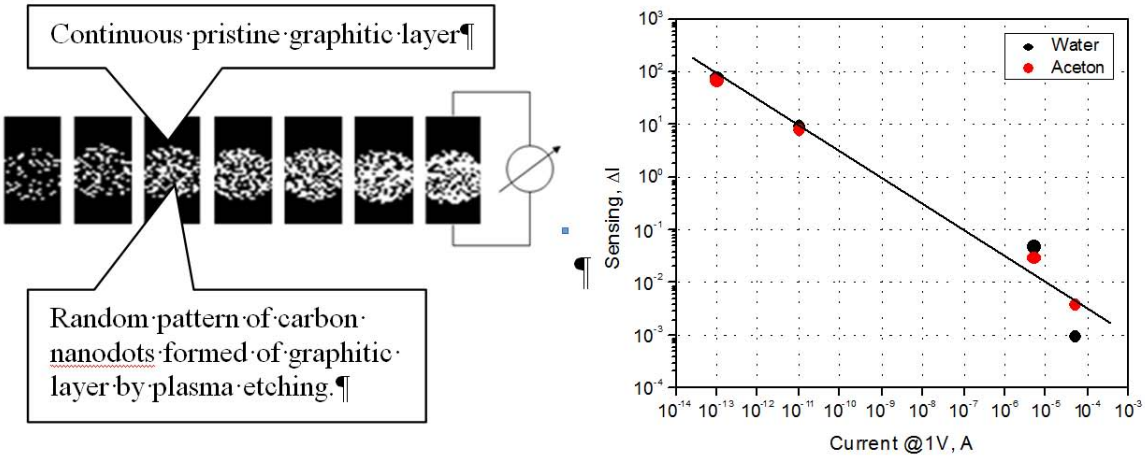

Fig. 2.20. (a) Change of conductance of graphitized diamond surface exposed to water and acetone vapor as a function of remaining conductance after etching in air plasma. Thick films with high conductance (current in the range 10^{-5} A) show vanishingly weak chemical response (current change of 10^{-3}). Instead, after etching the films exhibit much lower current (in the range of picoamper), which however may change by two order of magnitude when the sample is exposed to water vapor. (b) Illustration of the nonhomogeneous plasma etching of the graphitic layer and formation of array of graphitic nanodots on diamond surface.

We further propose that there are two ways in which the interacting molecules may modulate the surface conductance. Firstly, it may occur when the molecules adsorb on the diamond surface within the gaps separating the carbon nanoislands (A-I in Fig. 15). The adsorbed molecules can provide alternate conduction pathways or may facilitate tunneling through the energy barrier between the islands. Secondly, the molecules absorbed on the carbon nanofilm (A-II in Fig. 15) may change its electronic properties and in particular conductance. This could occur either by donor-acceptor charge transfer between the adsorbed molecules and the conductive surface or by the charge induction due to localized electric field near the adsorption site. Donor-acceptor charge transfers have been reported for semi-conducting carbon nanotubes [55-57]. The charge induction is an effect working in chemical field-effect transistors.

I.3. Direct Growth of Graphene on Quartz

When performing experiments with growth of carbon nanofilms on diamond surface in different gas atmospheres, it was noticed that the deposition of conductive carbon films could be achieved in methane atmosphere on non-diamond surfaces too. It was found also that the growth at certain temperature-pressure parameters may result in formation of graphene layers. Thus the possibility of use of the graphite furnace for the growth of graphene films on insulating substrates has been studied.

The main challenge to be met on the way of application of graphene in electronic industry is the development of technology of growth of uniform graphene layers on insulating wafer-size substrates. Currently there are three main methods which are being developed as techniques of growth/deposition of graphene on large areas. One of them is the deposition of nano/micro flakes of oxidized graphene (GO) by spin coating with subsequent conversion of the oxidized graphene into graphene by heating or via chemical reactions [58]. Though being simple, this method, however, does not provide satisfactory uniformity of the graphene layer.

Another method is the surface graphitization of SiC substrates at high temperature (e.g. [59]). This method allows fabrication of very uniform graphene films. However, high cost of SiC wafers prevent this method from commercial application. Though, the solution of this problem could be the epitaxial growth of SiC layer over Si wafer with subsequent conversion of this layer into graphene [60,61].

The third method is the CVD growth of graphene on nickel [62] or on copper [63].It is hard to control number of layers on nickel, but on copper act self-limiting mechanism allowing to grow 1-layered graphene. Although this method provides the very good quality graphene films as large as 30" diagonal, it also has drawback: mandatory step of transfer of the as-grown graphene from copper onto insulating substrate, what may cause considerable damage to the film [63, 63 suppl.].

Several groups used CVD method for direct deposition of graphene films on insulating substrates [64-66]. Although this method appeared to be suitable for the growth of graphene on large areas, no reports on the growth of uniform single-layer graphene on insulators have been published.

Below we report a method of direct CVD deposition of graphene films from methane on single crystal quartz substrates placed in graphite container. The obtained results show that the films are uniform, they possess high electrical conductance and are formed mostly of single-layer graphene.

I.3.1 Growth Procedure

It is known that graphite acts as a catalyst for methane decomposition. Taking into account this catalytic property of graphite we attempted to achieve the growth of graphene in the graphite vacuum furnace, which was originally developed for annealing of diamonds. The working chamber of the furnace was controllably filled with ultra-high purity methane at a pressure ranging from 5×10^{-6} mbar to 1200 mbar, which was used as the growth medium [67] (Fig. 3.1). Single crystal quartz and sapphire plates of size $4\times4\times0.5$ mm^3 cut perpendicular to c-axis and polished to roughness Ra < 10 Å were used as substrates for deposition of graphene.

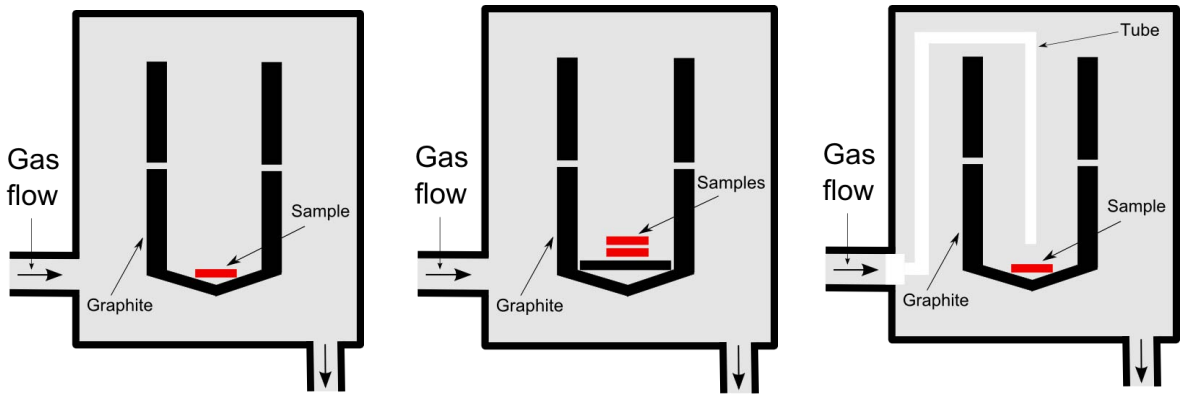

Fig. 3.1 Furnace with the graphite container (a), with two samples and additional graphite pad (b), with additional injector-tube for gas delivery directly to the sabstrate (c).

It was found, that the growth of conductive carbon films in graphite chamber filled with methane could be achieved at temperatures much lower than that required for spontaneous

non-catalytic decomposition of methane, which occurred at temperatures over 1200°C. Comparative experiments with a non-graphite ceramic chamber revealed that the presence of graphite was crucial for the decomposition of methane and deposition of carbon film at temperatures of 1200°C and below [68]. The lowest temperature at which the formation of carbon film was achieved was 650°C.

It has been found that the carbon film could grow on both sides of the substrate. Growth of the film occurred especially effectively on the bottom side of the substrate which was in contact with container bottom or graphite pad. It was also found that the proximity of another solid surface (counter surface) was very stimulating for formation of carbon film and the distance between the substrate surface and the counter surface (this distance is termed "slit" thereafter) is an important parameter of the growth. Notwithstanding the nature of the counter surface, the faster growth of the film was always observed for smaller slit. Fast formation of the film occurred even of the surfaces of two substrates lying one over another.

It is interesting that for small split, the growth of the film could be achieved at pressures considerably lower than those required for the formation of the films on the freely open surface. The role of the slit size has not been fully investigated yet and hence is still not clear. However, we believe that the slit creates conditions suppressing evaporation of carbon from the substrate surface increasing this way the probability of the nucleation and deposition processes.

The film deposition rate depends on the nature of substrate. The rate is higher for quartz than for sapphire. As a result, the growth of the carbon film on sapphire substrate occurs at higher methane pressure than that normally used for quartz. For instance, in order to achieve the formation of continuous film at a temperature of 1200°C in 1 hour on quartz it was necessary to keep the methane pressure at a level of 2-4 mBar, whereas for sapphire substrates the pressure had to be increased to 15 mbar and above. Possible reason for this difference is that the quartz has good crystal lattice match with graphene, whereas there is no good match with sapphire. Lattice constant of quartz is 4.914 Å, which is exactly 2 times greater than that of graphene (2.46 Å). In contrast, lattice constant of sapphire equals 4.758 Å, which is about 1.934 times as much as that of graphene. That is mismatch of the sapphire and graphene lattices is about 3.3%. This mismatch, though little it may seem, was a significant disadvantage for the formation of carbon films on sapphire. Because of this, most of the experiments were performed with quartz substrates. It was found that the optimal temperature-pressure-time parameters for the reliable growth of carbon films on quartz were 1200°C, 2 to 4 mbar and 1 hour.

I.3.2. Uniformity and Thickness

The carbon films grow at optimal parameters were visually very transparent and uniform. A light gray color of the film could be recognized only when directly comparing the color of the substrate with film and without it.

The film thickness has been measured on a substrate with a partially removed film. AFM measurements (non-contact mode) of the film edge show a uniform step between the film surface and the surface of bare substrate (Fig. 3.2). The height is of 0.2 nm only. It is small value, significantly less than 0.7 nm, which is expected for the step made by single layer graphene. Although it is not clear why the step is so small, this little value may be considered as an indication of monoatomic character of the deposited film.

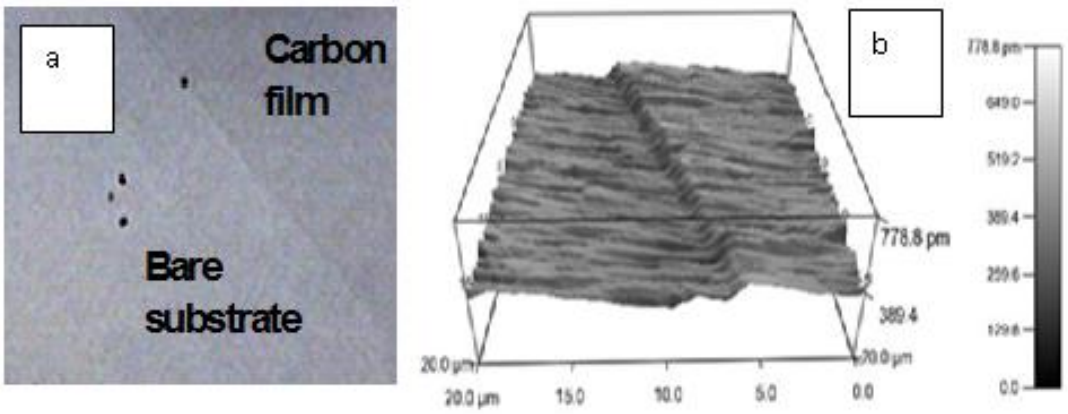

Figure 3.2 (a) Optical image of an edge of graphene film on quartz substrate viewed in transmitted light (contrast of the image was enhanced to clearly show the film, image size 50×50 µm^2). (b) AFM image of this edge. Height of the step of about 0.2 nm. Note that the height of the step is uniform over a distance of 20 µm.

Optical absorption measurements (performed by Prof. Kikkawa and his group, Penn State University) reveal characteristic spectra of single layer graphene (Fig. 3.3). Absorption strength at a wavelength of 550 nm may vary from 2.5 to 3%. This value is quite consistent with the absorption strength of 2,6% of perfect single layer graphene grown at copper and measured on the same wavelength [63]. The spectra taken in different places of the sample are almost identical, what is a good proof of uniformity of the film.

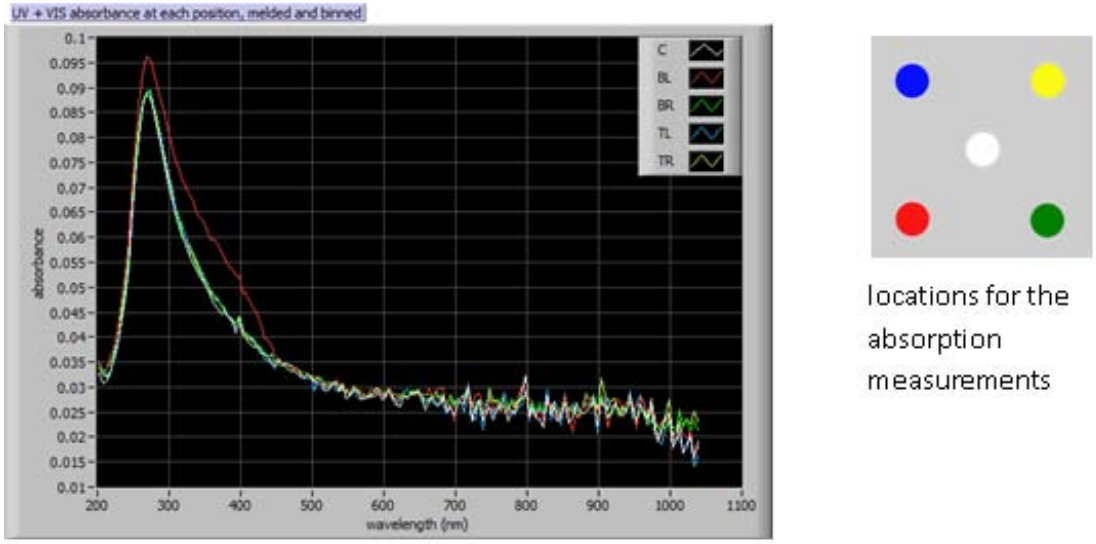

Fig. 3.3 Optical absorption measurements of carbon films deposited on quartz from methane in graphite container. Color of the spectra (left) correspond to the color of the spots (right) indicating the position where the measuremnets have been taken.

I.3.3 Raman characterization.

In Fig. 3.4, Raman spectra of carbon films grown in graphite chamber are compared with those of graphene grown on copper [63], TRGO [58], and graphene grown on MBE deposited

SiC [60]. Graphene grown on Cu reveals a dominating narrow 2D-peak (~2700 cm^{-1}) together with a minor G-band (~1580 cm^{-1}), what corresponds to a perfect single crystal graphene. In contrast, TRGO shows broad D- and G-bands and only traces of 2D-band, what means significant structural disorder (amorphous structure). The spectrum of graphene grown on SiC is very similar to that of the films grown in the present work. Both spectra exhibit somewhat broadened but well separated D- and G-bands as well as 2D-band of comparable intensity. This broadening of the Raman bands is definitely due to polycrystalline nature of the graphene films grown on quartz and SiC.

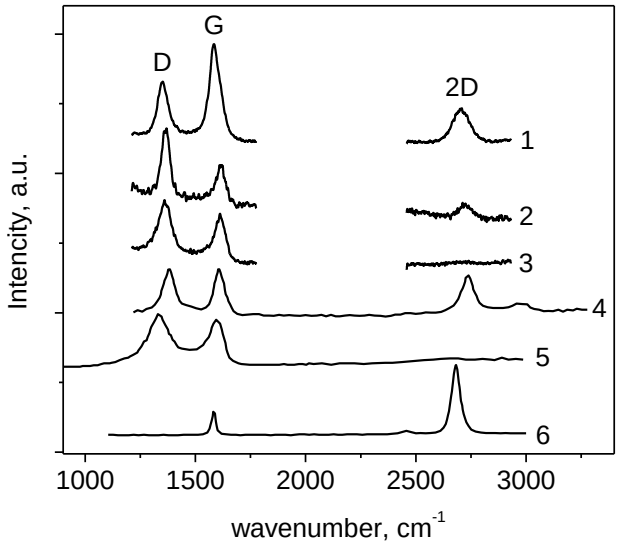

Fig. 3.4 Raman spectra of graphene films grown by different methods. Top to bottom: CVD on quartz from methane at 1200°C in graphite container for the growth time 2 hours (1), 30 min (2), and 30 min after preceding methane plasma treatment (3) (excitation at a wavelength of 514 nm); 4 – a few-layer graphene grown on MBE deposited SiC (replotted from [60]) 5 - TRGO (replotted from [58]); 6 - graphene grown on Cu (replotted from [63]).

I.3.4. Electrical Characterization

An important peculiarity of the growth process was found when studying the films grown for different times. Namely, the increase in the time of growth did not change noticeably the transparency and conductance of the films (Fig. 3.5). This effect was checked for the growth time up to 3 hours. Thus we could assume that no multilayer film formed. It appeared that there was sort of self-limiting mechanism of growth, making formation of multilayer graphene films unfavorable. Yet long time of growth did result in some changes in the temperature dependence of conductance making it less pronounced. Besides, Raman spectra of the films grown for a longer time revealed their higher quality compared to those grown for 30 minutes: stronger relative intensities of the G- and 2D-bands (Fig. 3.4).

Also it should be noted, the temperature dependence of conductance was similar to that reported for the exfoliated single-layer graphene transferred onto oxidized silicon substrate [69] (Fig. 3.5). These observations support statement concerning formation of a single-layer graphene.

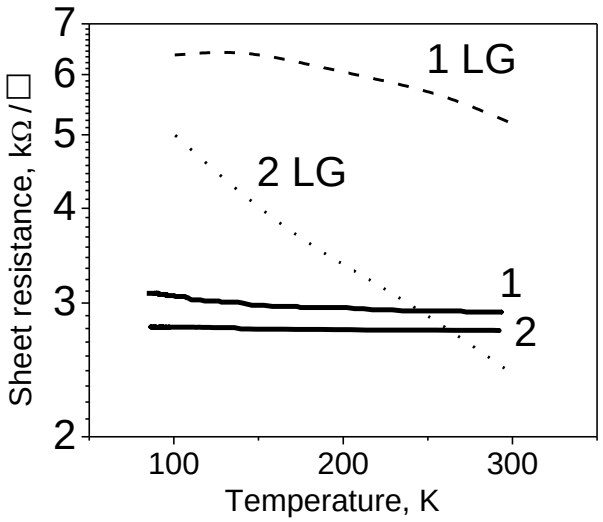

Fig. 3.5 Temperature dependence of the sheet resistance of carbon films grown at 1200°C for 30 min (1) and for 2 hours (2). For comparison, the sheet resistance of exfoliated one- (1 LG) and two- (2 LG) layer graphene deposited on oxidized silicon is shown too (adopted from [69]).

Unfortunately, the growth of the films could not be performed for very long time for the quartz surface degraded considerably after several hours of exposure to methane at high temperature. However, this degradation could be decreased by lowering the pressure, as can be seen in Fig. 3.6. Thus a possible way to increase the quality of graphene films grown by CVD deposition in graphite container is to decrease the methane pressure and to increase the time of growth.

It was found that the mobility at room temperature for the sample grown at 1200°C for 30 min is about 60 $cm^2/(Vs)$. The main charge carriers are holes.

As it is noted above, the growth of carbon films can be achieved in temperature range 650 -1200°C. Reduction in temperature, however, results in degradation of the film quality. Raman spectra of the films grown at temperatures 650 and 850°C show no 2D-band. The absence of the 2D-band indicates high atomic disorder of these films. Note that the growth of carbon films at temperature 850°C and below require much high pressure of methane. In the present case a pressure of 1200 mbar was used. In contrast, the growth at a temperature of 1200°C requires to keep the pressure at a level of 2-4 mbar only. Fig. 3.7 shows the conductance-versus-temperature dependences of carbon films deposited on quartz at different temperatures.

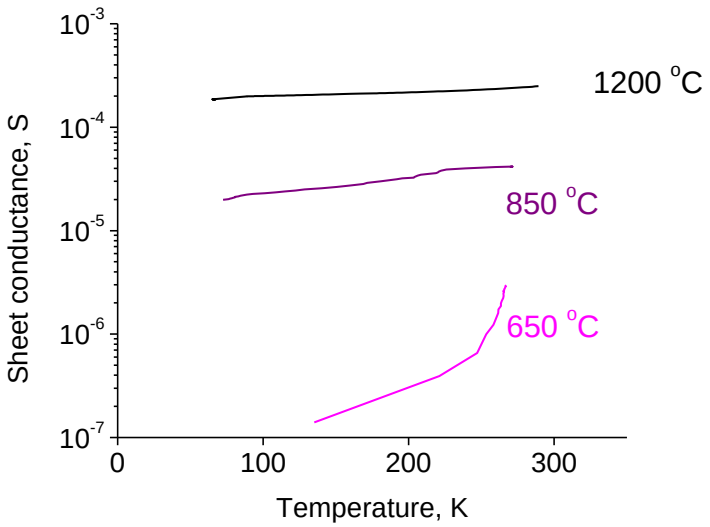

Fig. 3.7. Conductance of carbon films versus temperature. Conductance dependences of three films grown at different temperatures are compared.

It is seen that the increase in the growth temperature results in a strong increase in the conductance. Besides, the films grown at high temperature show more metallic behavior (less temperature dependence) than those grown at low temperatures. Intensity of Raman D-band decreases with temperature indicating better crystallinity of the film. In theory, direct growth of single crystal graphene on insulating substrates is possible at temperatures over 1700°C. Fig. 3.8 shows that the relative intensity of the D-band, which is characteristic of atomic disorder of graphene, approaches zero at temperatures 1700 – 1800C. Thus, a straightforward recipe for the CVD growth of perfect graphene is the increase in the growth temperature. However, a severe limiting factor of the growth temperature is the degradation of the substrate surface (see below).

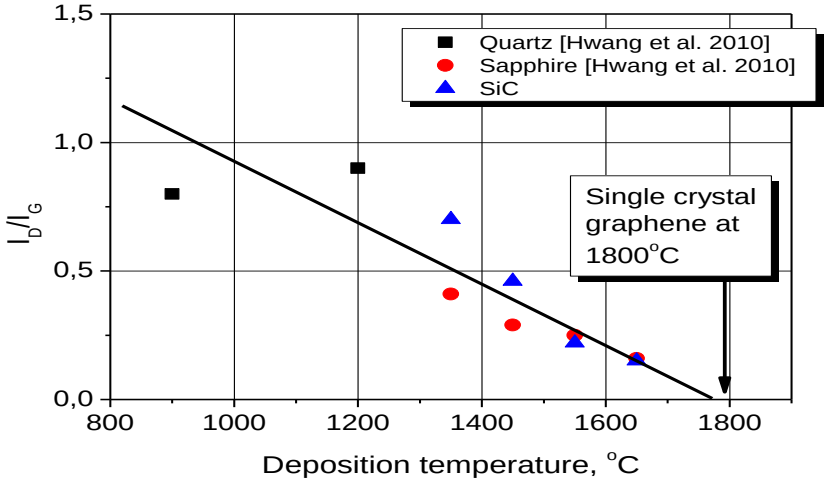

Fig. 3.8. Relative intensity of Raman D-band measured on graphene CVD-grown at different temperatures and different substrates. It is seen that at growth temperatures of 1700 to 1800C, formation of perfect crystalline graphene is expected.

I.3.5 Degradation

It has been also found, that the increase in temperature causes degradation of the quartz surface and this degradation may occur very fast even before the formation of the film (Fig. 3.9a). However, no sign of degradation is seen if the quartz substrates are annealed in vacuum at the same temperature. Thus, one may assume that the methane atmosphere stimulates the degradation process. The same behaviour of surface degradation has been also noticed for sapphire substrates. The degradation in methane has been checked on Si substrates too. It has been found that Si is very sensitive material and the surface degradation in methane could be observed at temperatures as low as 800°C (Fig. 3.9b).

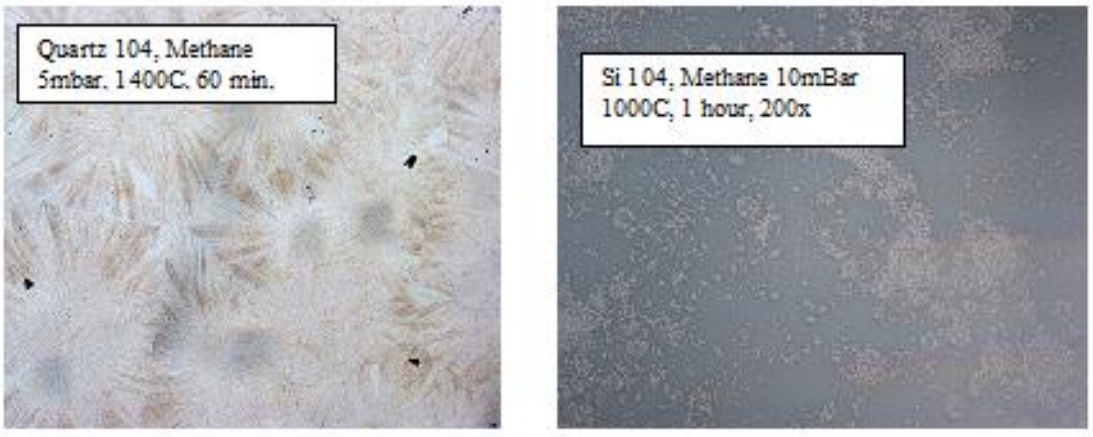

Fig. 3.9. Optical images (microscopy in transmitted light) of quartz (a) and silicon (b) substrates showing degradation after heating in methane at parameters indicated.

It is also worth to mention, that there is a threshold value of methane pressure, bellow which the film does not formation even in prolonged process. This value is close to 6 mbar. Therefore, it is important to precisely control the pressure of methane during the growth because the degradation may begin already at a pressure over 8 mbar (Fig. 3.10).

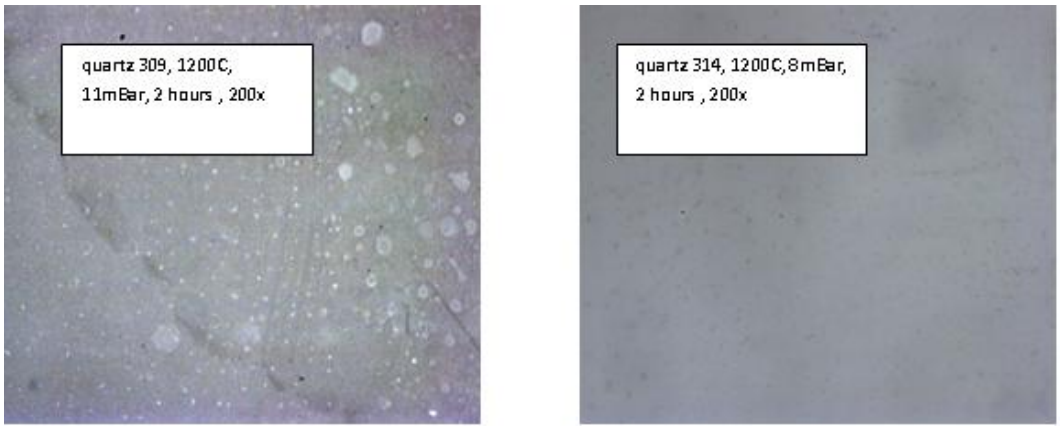

Fig. 3.10 Optical image of a grown film on quartz substrate viewed in transmitted light (contrast of the image was enhanced to clearly show the film, image size 0.5×0.5 mm^2 (200x)) for 2 hours. Grown at 11 mbar (a) and 8 mBar (b).

The degradation phenomenon causes considerable problems when carbon films are to be grown at high temperatures. Special precautions should be taken in order to suppress this negative effect and achieve growth of uniform films.

I.3.6. Compression with another methods of growth of graphene

In order to evaluate the electronic quality of the graphene films grown by different methods we compare their "estimated sheet resistance per one layer" R_s, which was calculated as the measured sheet resistance $R_{\square}$ multiplied by the average number of layers constituting the graphene film (Table 1). It is seen that R_s of graphene grown on quartz is significantly lower than that of TRGO and graphene grown from MBE deposited SiC and, eventually, it is comparable with R_s of the exfoliated graphene transferred on oxidized silicon. Though, graphene deposited on quartz is inferior to that grown on copper. We assume that the lower quality of graphene directly grown on quartz is because of its polycrystalline nature.

Table 1 Sheet Resistance of Graphene Films.

Method	Number of layers	$R_{\square}$, kΩ/□	R_s, kΩ/□
Presented method	1 (?)	2.5-3.5	2.5-3.5
Grown on Cu [63]	1	0.275	0.275
Exfoliated [69]	1	5.5	5.5
On MBE deposited SiC [61]	3 on Si(1 1 1); 2 on Si(1 1 0)	17; 90	34; 180
TRGO [58]	10 - 20	5.7	57 - 114

I.3.7 Selective deposition of graphene on insulating substrates

If was found that plasma treatment of quartz substrates, before placing them in graphite chamber, considerably influenced the growth of carbon films. A 1 minute exposure to low power RF oxygen plasma could completely suppress the growth of graphene (Fig. 3.11a). In contrast, methane plasma acted as a stimulator of the growth. Preceding methane plasma treatment resulted in fast growth of carbon deposit at pressures much lower than those required for the film formation on non-treated quartz surface (Fig. 3.11b) Although, it should be noted that films grown after methane plasma treatment were amorphous rather than graphene-like. Raman spectra of such films revealed the absence of 2D-band.

Further experiments with other plasma compositions were performed. It was found that nitrogen plasma had no effect on the film formation, whereas argon plasma and SF6 plasma acted like oxygen plasma – they suppressed the formation of the films.

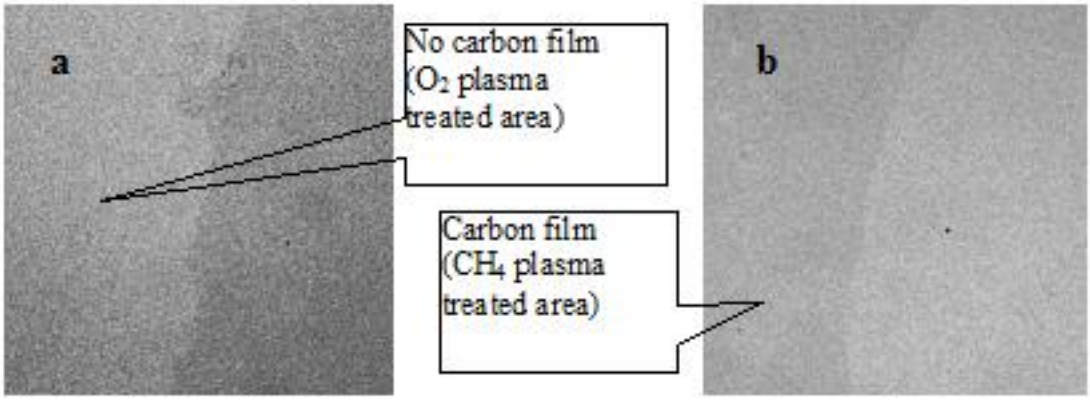

Fig. 3.11 Optical images (in transmitted light) of two quartz samples half of area of which was exposed to plasma before the growth of carbon films. The left side of samples is plasma-treated, whereas the right side is just cleaned in acetone. (a) Left side of this sample was exposed to oxygen plasma. (b) Left side of this sample was exposed to methane plasma. Size of the images is 0.2×0.2 mm^2 (enhanced contrast).

I.3.8 Chemical sensitivity of CVD-deposited Graphene

Chemical sensitivity of the graphene films CVD grown on quartz was tested in the same manner like it was done for carbon films on diamond. It was found that the conductance of these films was sensitive to exposure to water and acetone vapor. However, the dynamics of the response was different as compared with the carbon films on diamond. It is interesting, that after exposure to water vapor conductance did not recover fully, so this resembled a memory behavior when the conductance of the film retained the information on the preceding chemical exposure (Fig. 3.12).

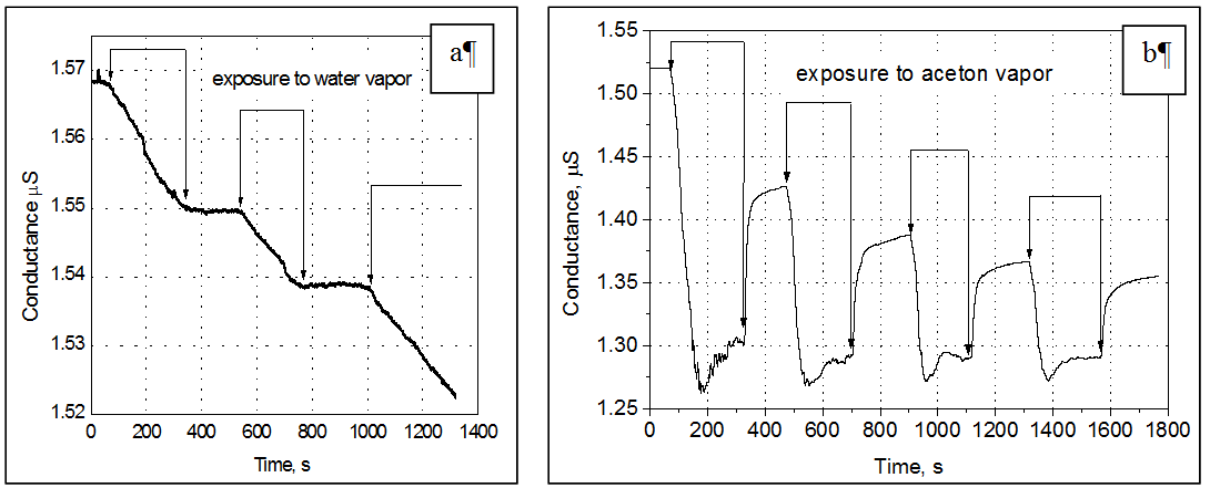

Fig. 3.12. Response of electrical conductance of graphene films CVD grown on quartz substrates to water (a) and acetone (b) vapor.

References to Part I

[1]1. R. Kalish, S. Prawer, " Graphitization of diamond by ion impact: Fundamentals and applications", Nuclear Instruments and Methods in Physics Research B, 106 (1995) 492-499.

[2]2. I. A. Dobrinets, A. D. Wieck, A. M. Zaitsev, T. Etzel, J. Butler, "Electrical Properties of Diamond Irradiated with Focussed Ion Beam", J. Wide Bandgap Materials, 9 (2001) 7-19.

[3]3. A. M. Zaitsev, "Carbon Nanowires Made on Diamond Surface by Focused Ion Beam", Physica Status Solidi (a), 202 (2005) R116-R118.

[4]4. C. Uzan-Saguy, C. Cyterman, R. Brener, V. Richter, M. Shaanan, R. Kalish, " Damage threshold for ion-beam induced graphitization of diamond", Appl. Phys. Letters, 67 (1995) 1194.

[5]5. A. V. Denisenko, "Unipolar Charge Carrier Injection in p-i-p Diamond Diodes: Theoretical and Experimental Studies", 1998, PhD thesis, Fern-University of Hagen, Germany.

[6]6. Toshimaro Sato, Kazutoshi Ohashi, Hiroyuki Sugai, Takashi Sumi, Katsuji Haruna, Hiroshi Maeta, Norimasa Matsumoto, Hideo Otsuka, " Transport of heavily boron-doped synthetic semiconductor diamond in the hopping regime", Phys. Rev. B, 61 (2000) 12970.

[7]7. R. Kalish, A. Resnik, K. W. Nugent, S. Praver, " The nature of damage in ion-implanted and annealed diamond", Nuclear Instruments and Methods in Physics Research B, 148 (1999) 626.

[8]8. L. C. Olsen, " Electrical Transport Properties of Graphite Assuming Lattice Scattering", Phys. Rev. B, 6 (1972) 4836.

[9]9. Y. Gurbuz, W. P. Kwang, J. L. Davidson, D. V. Kerns, "Diamond microelectronic gas sensor for detection of benzene and toluene", Sensors and Actuators, B 99 (2004) 207-215.

[10] Sberveglieri G. Recent developments in semiconducting thin-film gas sensors. Sens Actu B 1995;23(2-3):103-9.

[11] Bai H, Gaoquan S. Gas sensors based on conducting polymers. Sensors 2007;7:267-307.

[12] Kong J, Franklin NR, Zhou C, Chapline MG, Peng S, Cho K, et al. Nanotube molecular wires as chemical sensors. Science 2000;287:622-5.

[13] Zhang T, Mubeen S, Myung NV, Deshusses MA. Recent progress in carbon nanotube-based gas sensors. Nanotech 2008;19(33):332001-14.

[14] Wang Y, Yeow JTW. A review of carbon nanotubes-based sensors. J Sensor 2009;2009:9-24.

[15] Chopra S, Pham A, Gallard J, Parker A, Rao AM. Carbon-naotube-based resonant circuit sensor for anmmonia. Appl Phy Lett 2002;80(24):4632-4.

[16] Chopra S, McGuire K, Gothard N, Rao AM. Selective gas detection using carbon nanotube sensor. Appl Phy Lett 2003;83(11):2280-2.

[17] Cantalini C, Valentini L, Lozzi L, Armentano I, Kenny JM, Santucci S. NO_2 gas sensitivity of carbon nanotubes obtained by plasma enhanced vapor deposition. Sens Actu 2003;93(1-3):333-7.

[18] Jing L, Yijiang L, Qi Y, Martin C, Jie H, Meyyappan M. Carbon nanotube sensors for gas and organic vapor detection. Nano Lett 2003;3(7):929-33.

[19] Valentini L, Armentano I, Kenny JM, Cantalini C, Lozzi L, Santucci S. Sensors for sub-ppm NO_2 gas detection based on carbon nanotube thin films. Appl Phys Lett 2003;82(6):961-3.

[20] Wongwiriyapan W, Honda S, Konishi H, Mizuta T, Ikuno T, Ito T, et al. Single-walled carbon nanotube thin-film sensor for ultrasensitive gas detection. Jpn J Appl Phys 2005;44:L482-5

[21] Abraham JK, Philip B, Witchurch A, Varadan VK, Reddy CC. A compact wireless gas sensor using a carbon nanotube/PMMA thin film chemiresistor. Smart Mater Struct 2004;13(5):1045-9.

[22] Wisitsoraat A, Tuantranont A, Thanachayanont C, Patthanasettakul V, Singjai P. Electron beam evaporated carbon nanotube dispersed SnO2 thin film gas sensor. J Electroce 2006;17(1):45-9.

[23] Liang YX, Chen YJ, Wang TH. Low-resistance gas sensors fabricated from multiwalled carbon nanotubes coated with tin oxide layer. App Phy Lett 2004;85(4):666-8.

[24] Kong J, Chapline MG, Dai H. Functionalized carbon nanotubes for molecular hydrogen sensors. Adv Mat 2001;13(18):1384-6.

[25] Zhang T, Nix MB, Yoo BY, Deshusses MA, Myung NV. Electrochemically functionalized single-walled carbon nanotube gas sensor. Electroanal 2006;18(12):1153-8.

[26] Baratto C, Atashbar MZ, Faglia G, Sberveglieri G. Functionalized single-walled carbon nanotube-based gas sensor. Pro Inst Mech Eng N: J Nanoeng Nanosys 2007;221(1):17-21

[27] Odom TW, Huang JL, Kim P, Lieber CM. Atomic structure and electronic properties of single-walled carbon nanotubes. Nature 1998;391:62-4.

[28] Zaitsev AM. Carbon Nanowires Made on diamond surface by focused ion beam. Phys Stat Sol (a) 2005;202(10):R116-18.

[29] Zaitsev AM, Dobrinets IA. Carbon nanodots made on diamond surface by focused ion beam. Phys Stat Sol (a) 2006;203(5):R35-7.

[30] Zaitsev AM, Levine AM, Zaidi SH. Temperature and chemical sensors based on FIB-written carbon nanowires. IEEE Sens J 2008;8(6):849-56.

[31] Zaitsev AM, Levine AM, Zaidi SH. Carbon nanowire-based temperature sensor. Phys Stat Sol (a) 2007;204(10):3574-79.

[32] Robertson J. Diamond-like amorphous carbon. Mat. Sci Eng R 2002;37(4-6):129-281.

[33] Fowler JD, Allen MJ, Tung VC, Yang Y, Kaner RB, Weiller H. Practical chemical sensors from chemically derived graphene. ACS Nano 2009;3(2):301-6.

[34] Dan Y, Lu Y, kybert NJ, Luo Z, Johnson ATC. Intrinsic response of graphene vapor sensors. Nano Lett 2009;9(4):1472-5.

[35] Gao X, Xue Q, Hao L, Zheng Q, Li Q. Ammonia sensitivity of amorphous carbon film/silicon heterojunctions. Appl Phy Lett 2007;91(12):122110-1-4.

[36] Lukaszewicz JP. An application of carbon-type semiconductors for construction for the construction of a humidity sensitive diode. Sens Actu B 1992;6:61-5

[37] Lukaszewicz JP, Panas M, Siedlewski J. Sodium-doped carbons for humidity sensor construction. Sens Actu B 1996;32(3):221-6

[38] Lukaszewicz JP. Carbon-film-based humidity sensor containing sodium or potassium recovery effect. Sens Actu B 1999;60(2):184-90.

[39] Lukaszewicz JP, Skompska M. A novel carbon-based ionic conductor for humidity sensors. Sens Actu B 2006:113(2):970-7.

[40] Evans T, James PF. A study of the transformation of diamond to graphite. Proc R Soc Lond A 1964;277(1369):260-9.

[41] Davies G, Evans T. Graphitization of diamond at zero pressure and at a high pressure. Proc R Soc Lond A 1972;328(1574):413-27.

[42] Haines SR, Williams KH, Almond N, Schwitters M, Martin DS, Butler JE, et al. The initial stages of graphite formation on the diamond. J Elec Spec Rel Phen 2006;152(1-2):33-36.

[43] Ferrari AC, Robertson J. Interpretation of Raman spectra of disordered and amorphous carbon. Phys Rev B 2000;61(20):14095-107.

[44] Lewis A. Evidence of Mott model of hopping conduction in the anneal stable state of amorphous silicon. Phys Rev Lett 1972;29(23):1555-8.

[45] Massarani B, Bourgoin JC, Chrenko RM. Hopping conduction in semiconducting diamond. Phys Rev B 1978;17(4):1758-69.

[46] Morigaki K. Physics of amorphous semiconductors. London:Imperial College Press; 1999.

[47] Ambegaokar V, Halperin BI, Langer JS. Hopping conductivity in disordered systems. Phys Rev B 1971;4(8):2612-20.

[48] Ambegaokar V, Cochran S, Kurkijarvi J. Conduction in random systems. Phys Rev B 1973;8(8):3682-8.

[49] Takada T, Nakahara M, Kumagal H, Sanada Y. Surface modification and characterization of carbon black with oxygen plasma. Carbon 1996;34(9):1087-91.

[50] Boudou JP, Paredes JI, Cuesta A, Martine-Alonso A, Tascon JMD. Oxygen plasma modification of pitch-based isotropic carbon fibres. Carbon 2003;41(1):41-56.

[51] Bubert H, Haiber S, Brandl W, Marginean G, Heintze M, Bruser V. Characterization of the uppermost layer of plasma-treated carbon nanotubes. Diamond Relat Mater 2003;12(3):811-5.

[52] Vohrer U, Zschoerper NP, Koehne Y, Langowski S, Oehr C. Plasma modification of carbon nanotubes and bucky papers. Plasma Proc Poly 2007;4(1):S871-7.

[53] Chen C, Liang B, Ogino A, Wang X, Nagatsu M. Oxygen functionalization of multiwall carbon nanotubes by microwave-excited surface-wave plasma treatment. J Phys Chem C 2009;113(18):7659-65.

[54] Tay BK, Sheeja D, Lau SP, Guo JX. Study of surface energy of tetrahedral amorphous carbon films modified in various gas plasma. Diamond Relat Mater 2003;12(10):2072-6.

[55] Hutchison GR, Ratner MA, Mark TJ, Naaman R. Adsorption of polar molecules on a molecular surface. J Phys Chem B 2001;105(15):2881-4.

[56] Someya T, Small J, Kim P, Nuckolls C, Yardley JT. Alcohol vapor sensors based on single-walled carbon nanotube field effect transistors. Nano Lett 2003;3(7):877-81.

[57] Fan Y, Burghard M, Kern K. Chemical defect decoration of carbon nanotubes. Adv Mater 2002;14(2):130-3.

[58] Tran Viet Cuong, Viet Hung Pham, Quang Trung Tran, Sung Hong Hahn, Jin Suk Chung, Eun Woo Shin, Eui Jung Kim, Optoelectronic properties of graphene thin films prepared by thermal reduction of graphene oxide, Materials Letters 2010; 64:765-7.

[59] Caterina Soldano, Ather Mahmood, Erik Dujardin, Production, properties and potential of graphene, Carbon 2010; 48:2127–50

[60] Hyun-Chul Kang, Hiromi Karasawa, Yu Miyamoto, Hiroyuki Handa, Tetsuya Suemitsu, Maki Suemitsu, Taiichi Otsuji, Epitaxial graphene field-effect transistors on silicon substrates, Solid-State Electronics 2010; 54(9):1010-4.

[61] Hyun-Chul Kang, Hiromi Karasawa, Yu Miyamoto, Hiroyuki Handa, Hirokazu Fukidome, Tetsuya Suemitsu, Maki Suemitsu, Taiichi Otsuji, Epitaxial graphene top-gate FETs on silicon substrates, Solid-State Electronics 2010; 54(10):1071-5.

[62] Keun Soo Kim, Yue Zhao, Houk Jang, Sang Yoon Lee, Jong Min Kim, Kwang S. Kim, Jong-Hyun Ahn, Philip Kim, Jae-Young Choi, Byung Hee Hong, Large-scale pattern growth of graphene films for stretchable transparent electrodes, Nature 2009; 457:706-710.

[63] Sukang Bae, Hyeongkeun Kim, Youngbin Lee, Xiangfan Xu, Jae-Sung Park, Yi Zheng, Jayakumar Balakrishnan, Tian Lei, Hye Ri Kim, Young Il Song, Young-Jin Kim, Kwang S. Kim, Barbaros O¨zyilmaz, Jong-Hyun Ahn, Byung Hee Hong and Sumio Iijima, Roll-to-roll production of 30-inch graphene films for transparent electrodes, Nature Nanotechnology 2010; 5:574-8.

[64] Tomohide Takami, Shuichi Ogaway, Haruki Sumi, Toshiteru Kaga, Akihiko Saikubo, Eiji Ikenaga, Motonobu Sato, Mizuhisa Nihei, Yuji Takakuwa, Catalyst-Free Growth of Networked Nanographite on Si and SiO2 Substrates by Photoemission-Assisted Plasma-Enhanced Chemical Vapor Deposition, e-J. Surf. Sci. Nanotech 2009; 7:882-90.

[65] Mark H. Rmmeli, Alicja Bachmatiuk, Andrew Scott, Felix Brrnert, Jamie H. Warner, Volker Hoffman, Jarrn-Horng Lin, Gianaurelio Cuniberti and Bernd Bchner, Direct Low-Temperature Nanographene CVD Synthesis over a Dielectric Insulator, ACS Nano 2010; 4(7):4206-10.

[66] Jeonghyun Hwanga, Virgil B. Shieldsa, Christopher I. Thomasa, Shriram Shivaramana, Dong Haoa, Moonkyung Kima, Arthur R. Wollb, Gary S. Tompac and Michael G. Spencera, Epitaxial growth of graphitic carbon on C-face SiC and sapphire by chemical vapor deposition (CVD) , Journal of Crystal Growth 2010; 312(21):3219-24.

[67] S. V. Samsonau and A. M. Zaitsev, Provisional patent application, CSI/CUNY (2010).

[68] N. Muradov, Catalysis of methane decomposition over elemental carbon, Catatlysis Communications 2001; 2:89-94.

[69] S. V. Morozov, K. S. Novoselov, M. I. Katsnelson, F. Schedin, D. C. Elias, J. A. Jaszczak and A. K. Geim, Giant Intrinsic Carrier Mobilities in Graphene and Its Bilayer, Phys. Rev. Lett. 2008; 100(1):016602.

PART II, THEORY

II.1 CONTINUUM THEORY OF CARBON PHASES

II.1.1 Introduction

II.1.1.1 Carbon Phases

Carbon is one of the most abundant elements in the universe and the most versatile material known to a man. This element is the basis of life on Earth and constitutes interiors of the celestial objects: outer planets, Uranus and Neptune, and white dwarf stars. Carbon is often considered to be silicon of the future because of the unique properties resulting from the variety of possible structural forms. A wide range of electronic properties of carbon from insulating/semiconducting diamond to metal-like graphite, nanotubes, and graphene sheets yields many technological applications in different areas of human activity. Such versatility of this element in nature results from the unique property of a carbon atom to form bonds of many different configurations, called hybridizations: liner sp^1, planar sp^2, tetrahedral sp^3, etc. All of this causes great scientific interest in thermodynamic properties of carbon.

Equilibrium carbon phases have been studied for many years. Despite the tremendous technical difficulties of experimental studies (temperatures of up to 10,000 K and pressures of 100÷1000GPa) the phase diagram of carbon has been created [1-3]. Thermodynamic databases helped develop fairly good bulk-thermodynamic free-energy functions that reproduce the low-temperature portion of the carbon phase diagram [4]. Because of the experimental difficulties, the theoretical (density functional) and numerical (MC and MD) methods of study of carbon phases gained popularity in the scientific community [5-15]. The phase diagram of carbon most commonly considers three clearly distinguished phases: *graphite, diamond, and liquid carbon*, although there is a number of high energy phases, e.g. bc8 and simple cubic, which were found to be metastable al low pressure and temperature [5] and stable at high pressure conditions [6]. Analysis of the behavior of graphite under conditions of isotropic pressure brought a surprising result that at least its rhombohedral modification can transform into diamond without thermal activation at 80GPa [7]. Although these studies are still work in progress and the experimental phase diagram in its finality is still to be drawn, many features have been clarified recently: for instance, a triple point of coexistence of the three phases has been found to be around the temperature of 4250 K and pressure of 15GPa, see [8] and Figure 1.

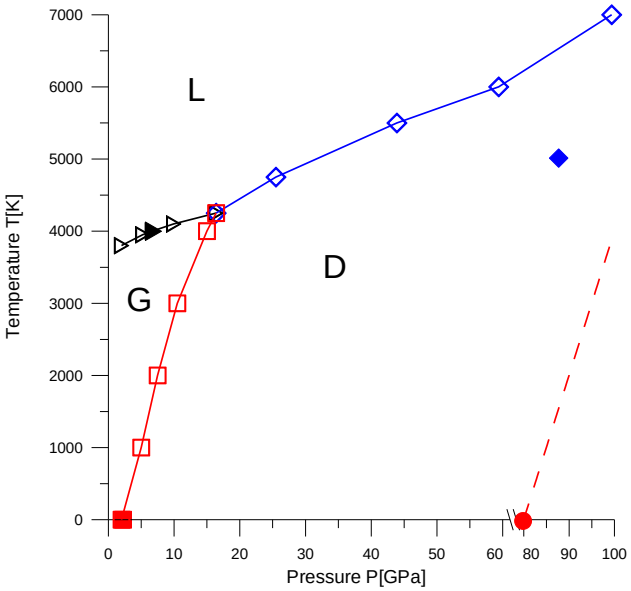

Fig. 1.1 (Color online). Low temperature-pressure region of the carbon phase diagram. G—graphite, D—diamond, L—liquid carbon regions. Solid lines—phase boundaries based on the data of [8]; dashed line—graphite/diamond spinodal line based on the data of [7]. Red square—(T=0K, P=1.36GPa); red circle—(T=0K, P=80GPa); black triangle—(T=4000K, P=6.7GPa); blue diamond—(T=5000K, P=85GPa).

Experimental results on liquid carbon are scarce because of the extreme conditions and/or short times of observations of the liquid state. However, a maximum in the melting temperature of graphite as a function of pressure has been observed in a number of studies [1-3]. Explanations of the maximum led to the introduction of two types of liquids: low-pressure graphite-like predominantly-sp^2 and high-pressure diamond-like predominantly-sp^3 [15]. Ree et al [9-11] conducted MD simulations and presented the isotherms of liquid carbon exhibiting a clear Van der Waals type dependence between the mostly sp^2 and sp^3 liquids. As a result, a liquid-liquid phase transition (LLPT) has been predicted. Moreover, a second triple point of coexistence of the two liquids and graphite and a critical point of the coexistence of the two liquids at the temperature around 9000K and pressure of 11GPa have been conjectured [9-11], although these did not follow from the experimentally observed properties of the liquid [1-3]. Numerical modeling of carbon structures relies heavily on the choice of the interaction potential, which is being constantly revised approaching the "real" interaction of carbon atoms. Recently Wang, Scandolo, Car [12] and Ghiringhelli *et al* [8] presented calculations using an improved interaction potential and found no evidence of LLPT or the critical point for liquid carbon. However, there are no doubts that as pressure increases atomic coordination of carbon undergoes an adjustment from three- to four- and higher-fold numbers [6].

Carbon may also exist in another solid-state form, amorphous [16-17]. Classification of carbonacious materials as 'amorphous' is not straightforward as many different systems fall into this category. One of the important parameters of such materials is the sp^3/sp^2 ratio. Amorphous carbon with high ratio, usually at or above 70%, is called tetrahedral (ta-C); it is also often called diamond-like carbon due to similarity of electrical and mechanical properties of ta-C to those of diamond. There is another category of amorphous carbon that attracts attention of the researchers—*nanostructured amorphous carbon* (na-C). Na-C can be manufactured using several different techniques: chemical vapor deposition (CVD) of carbon atoms, focused ion beam bombardment (FIB) of carbon surfaces with non-carbon ions [18-20], etc. Regardless of the preparation technique na-C's have two common features. First, these materials are always produced in the form of thin films, wires, or small particles that is, nanostructures. Second, although theoretical calculations and numerical simulations of such materials produced energies of formation significantly higher than those of graphite and diamond at the same temperatures [13, 21-23], these materials possess certain degree of thermodynamic stability.

The MD/MC cluster simulation methods are an excellent tool of materials study when equilibrium properties of phases—graphite, diamond, liquid, and amorphous—are considered [5-13]. These methods, however, encounter significant difficulties describing nucleation of the new phases [24] because they deal with relatively small clusters of atoms and do not allow for the analysis of heterosystems. As a result, stability of na-C can hardly be analyzed based on the cluster simulation methods. Another important area where these methods fail is the kinetics of phase transformations. A different method, which would allow for the analysis of the interface regions and kinetics, is required for the uninterrupted progress of the study of carbon.

II.1.1.2 Continuum Method of Phase Transitions

A *continuum approach* can serve this purpose. Many researchers have noticed that there are continuous transformation paths between different phases of carbon [5, 7]. In this publication we discuss our efforts to build a Landau-type theory of carbon phases [25, 26]. The theory does not introduce a new phase diagram of carbon but uses already existing data on phase boundaries of the diamond, graphite, and liquid phases [1-14]. Specifically, we will be using the database of [4] for the low-temperature region (0÷3000K) and the thermodynamic calculations of [8] for the high-temperature region (3000÷6000K) of the phase diagram. The theory has proven to be able to analyze a variety of systems [27, 28]; it provides a universal approach to a variety of processes and has an important advantage of analyzing both stability and transformation kinetics incorporating the thermodynamic and dynamic data into a unified scheme. To the best of our knowledge this is the first application of the theory to a system with pure covalent bonding. Most of the results of the paper relate to the region of the diagram near the graphite/diamond/liquid triple point, Fig.1.

The Landau theory of phase transitions is a mean-field type of theory. In the framework of this theory a state of a system, in addition to the thermodynamic variables like temperature T and pressure P, is represented by a certain value of a 'hidden' variable η, called an *order parameter* (OP) [25, 26]. OP is a low-dimensional characteristic of a particular transformation in a multi-dimensional space. The transformation is fully characterized by the *coarse-grained* free energy, which may be significantly simplified by taking into account all the symmetries of the system. Introduction of the OP allows one to define a *phase* as a locally stable homogeneous (with respect to the OP) state of the system. As known, in an open one-component system, a phase corresponds to a minimum of the molar Gibbs free energy, G(T, P, η). Hence, the OP for this state can be found among the critical points of G as a function of OP:

$$\left(\frac{\partial G}{\partial \eta}\right)_{T,P} = 0 \qquad (1)$$

The free energy function that describes a phase transition must have at least two minima with respect to OP that correspond to the phases: $\eta=\eta_0$, and $\eta=\eta_1$ (e.g. $\eta_1>\eta_0$), and a maximum, which corresponds to the *transition state*, $\eta=\eta_t$, that is, the barrier that separates the basins of stability of the phases. Transition state, a free-energy maximum with respect to OP, can also be found among the roots of Eq.(1) but, contrary to the bulk phases, it is locally unstable under the conditions of constant pressure that is $(\partial^2 G/\partial\eta^2)_{T,P}(\eta_t)<0$, see Inset (a) of Figure 2. The phase-equilibrium temperature or pressure P_E, is defined by the equation $G(T,P_E,\eta_0) = G(T,P_E,\eta_1)$. A system may also have one or several *spinodal points* that is, temperature and pressure values (T, P_S) where a metastable phase ultimately loses its stability and becomes absolutely unstable (see Figs. 1.2). Experimentally the spinodal points manifest themselves in disappearance of a need for thermal or chemical activation for the transition. In the language of the continuum theory the spinodal points appear when the OP of the transition state becomes equal to that of the metastable phase, e.g.

$$\eta_t(T,P_S^0) = \eta_0(T,P_S^0) \qquad (2)$$

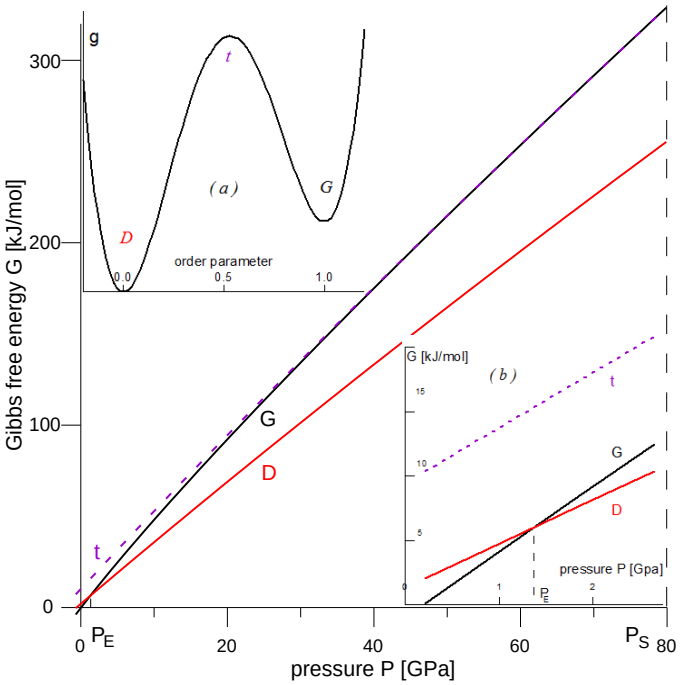

Fig. 1.2. (Color online). Gibbs free energy G of the diamond (D) and graphite (G) phases and the transition state (t) as functions of pressure P at T=0K using the database of [4] and estimates of Eq.(29). Inset (a)—Normalized Gibbs free energy g as a function of the order parameter at $P>P_E$. Inset (b)—G's as functions of P near the equilibrium value P_E=1.36GPa.

Many systems cannot be described by a single OP due to variety of transitions that may occur simultaneously. In this case the most convenient way to define the order parameters is to set them as independent. Even with two independent OP the free energy G(T, P, η, ξ) has significantly greater variety of types of the critical points than with one, the most popular additional type is the saddle point [29]. The sufficient condition of local minimum at the two-OP critical point is that:

$$\frac{\partial^2 G}{\partial \xi^2} > 0, \; and \; \frac{\partial^2 G}{\partial \eta^2}\frac{\partial^2 G}{\partial \xi^2} - \left(\frac{\partial^2 G}{\partial \eta \partial \xi}\right)^2 > 0 \qquad (3)$$

In the framework of the continuum field-theoretic approach of the Landau theory the structural *heterogeneities* are described by the gradients of the OP so that the molar Gibbs free energy of the substance is expressed as follows [30-32]:

$$\hat{G} = G(T,P,\eta) + \frac{1}{2}\kappa(T,P)\,(\nabla\eta)^2 \qquad (4)$$

where κ is called the *gradient-energy* coefficient. Thus, the *total* Gibbs free energy of the system of volume $\mathcal{V}$ is

$$\mathcal{G}\{T,P,\mathcal{N},\eta(\mathbf{r})\} \equiv \int_{\mathcal{V}} \rho \hat{G}\, d^3x \qquad (5)$$

where ρ is the molar density (V is the molar volume):

$$\rho^{-1} \equiv (\frac{\partial G}{\partial P})_{T,\eta} = V \qquad (6)$$

and $\mathcal{N}$ is the number of moles in the system:

$$\mathcal{N} \equiv \int_{\mathcal{V}} \rho \, d^3 x = const(T,P) \qquad (7)$$

Taking into account the constraint of fixed number of moles $\mathcal{N}$ in the system[1] we obtain that the open-system variational problem ($\mathcal{G}\rightarrow$min, $\mathcal{N}$=const, $\mathcal{V}\neq$const) yields the following boundary-value problem [33] for the equilibrium distribution $\eta_E(\mathbf{r})$:

$$\frac{\partial \rho(G-\mu)}{\partial \eta} - \nabla(\rho \frac{\partial \hat{G}}{\partial \nabla \eta}) = 0 \quad in\ \mathcal{V}; \qquad (8a)$$

$$\mathbf{n} \cdot \nabla \eta = 0 \quad on\ \hat{\mathcal{V}}; \qquad (8b)$$

$$\rho[G - \mu - \kappa/2(\nabla \eta)^2] = 0 \quad on\ \hat{\mathcal{V}}; \qquad (8c)$$

Here μ is the chemical potential of the system which depends on T, P, and $\mathcal{V}$; $\hat{\mathcal{V}}$ is the boundary of $\mathcal{V}$, and **n** is the unit vector on $\hat{\mathcal{V}}$. The free-boundary condition, Eq.(8c), appears because the volume of an open system is not specified. From the boundary conditions, Eqs.(8b,c), follows that

$$\mu = G(T, P_E, \eta_E\{\hat{\mathcal{V}}\}). \qquad (9)$$

Coexistence of two phases at equilibrium entails a layer between them called an *interface*. Many properties of an interface at equilibrium in a one-component medium can be completely determined by just one intensive quantity, the surface tension or *interface free energy* σ [34]. In the continuum formulation the interface is represented by a transition zone of certain thickness l where the OP changes its value from that in the bulk of one phase, e.g. η_0, to that in the bulk of the other one, e.g. η_1. Then the interfacial energy and thickness can be defined as follows [32]:

$$\sigma \equiv \int_{-\infty}^{+\infty} \rho \left[\hat{G}(T, P_E, \eta_E) - \mu \right] dx; \qquad l \equiv \frac{|\eta_1 - \eta_0|}{\max |d\eta/dx|}. \qquad (10)$$

In the case of a one-dimensional system with the size X in the direction perpendicular to the plane of the interface, the Euler equation, Eq.(8a), can be integrated once. Taking into account the free-boundary condition, Eq.(8c) and the fact that $\rho \neq 0$, we find that the 1D open-system equilibrium-state boundary-value problem takes the form:

$$G(T, P_E, \eta_E) - \frac{\kappa}{2}(\frac{d\eta_E}{dx})^2 = \mu \qquad for\ 0 < x < X, \qquad (11a)$$

[1] We define q≡const(u) as a quantity that does not depend on u but may depend on other variables of the problem.

$$\frac{d\eta_E}{dx}=0 \qquad for\ x=0,\ X. \tag{11b}$$

Then one can find the expressions for σ and *l* in an unlimited (X→∞) open system:

$$\sigma=\sqrt{2\kappa}\int_{\eta_0}^{\eta_1}\frac{\rho\, d\eta}{\sqrt{G_E-\mu}};\qquad l=|\eta_1-\eta_0|\sqrt{\frac{\kappa/2}{G_E-\mu}} \tag{12}$$

In the case of two OP's:

$$\hat{G}=G(T,P,\eta,\xi)+\frac{1}{2}\kappa_\eta(T,P)\,(\nabla\eta)^2+\frac{1}{2}\kappa_\xi(T,P)\,(\nabla\xi)^2 \tag{13}$$

If the molar density does not vary strongly, it may be assumed a constant, $\rho=\bar{\rho}=const(x)$, and the interface energy may be expressed as follows [35]:

$$\begin{aligned}\sigma&=2\bar{\rho}\int_{-\infty}^{+\infty}\{G(T,P_E,\eta_E,\xi_E)-\mu\}dx\\&=\bar{\rho}\int_{-\infty}^{+\infty}\{\kappa_\eta(\frac{d\eta_E}{dx})^2+\kappa_\xi(\frac{d\xi_E}{dx})^2\}dx\end{aligned} \tag{14}$$

II.1.1.3 Stability of Transition State in Closed Systems

The transition state of the single-OP homogeneous system, η_t, corresponds to a maximum of G(T, P, η) with respect to the OP variations and is absolutely unstable (that is, with respect to small fluctuations of η) in an open system (that is, for T,P=const). However, the stability of this state can change dramatically in a *closed system* when the condition of constant volume is imposed: $\mathcal{V}$=const. In this case instead of the molar Gibbs free energy as a function of pressure, G(T, P, η), it is more convenient to use the molar Helmholtz free energy, F(T, V, η), as a function of the molar volume V, Eq.(6). The latter can be found from the former through the Legendre transformation:

$$F(T,V,\eta)=G-P(\frac{\partial G}{\partial P})_{T,\eta}$$

Recently one of the authors (AU) used the continuum method to analyze the case of a closed system and showed [36] that a homogeneous transition state, η_t, can be thermodynamically stable if:

$$\left.\frac{\left(\frac{\partial^2 G}{\partial P \partial \eta}\right)^2}{\frac{\partial^2 G}{\partial \eta^2}\frac{\partial^2 G}{\partial P^2}}\right|_{\eta=\eta_t} > 1. \qquad (15)$$

As known, in a closed system of given size and average molar volume a heterogeneous mixture of the bulk phases is more stable than any other homogeneous state of the system. However, as it was demonstrated in [36], if the size of the closed system X is below the critical limit X_{cr}:

$$X < X_{cr} \equiv \frac{\pi}{2\sqrt{2}} l \,, \qquad (16)$$

the homogeneous transition state can be globally stable that is, have less Helmholtz free energy than any other equilibrium state including heterogeneous ones. Thus, if the material parameters of the system satisfy the criterion, Eq.(15), and the linear sizes—Eq.(16) then the homogeneous transition state, η_t, becomes the most stable state of the closed system in the certain range of average molar volumes.

The structure of the paper is as follows. In Sec. II we introduce a continuum model of carbon phases and demonstrate how the parameters of the model may be obtained from the data on nucleation of diamond on graphite and from liquid. In Sec. III we apply the developed model to the problem of crystallization of graphite by considering the processes of nucleation of graphite from liquid phase. The model will be also used in the present paper to gain an insight into the equilibrium properties of the amorphous phase of carbon at nanoscale dimensions (na-C) and amorphization of carbon under conditions of FIB irradiation of CVD-diamond nanofilms [18-20]. In Sec. IV we discuss the obtained results and extensions of the model on different systems.

II.1.2 Continuum Model of Carbon

II.1.2.1 Order parameters

The choice of OP's for a real-material continuum modeling is always a complicated matter. As we pointed out in the Introduction our goal is to construct a model that describes the processes of carbon melting-crystallization and the graphite-diamond structural transformation. To describe the variety of possible structural forms and different transformations of carbon in the region of the phase diagram near the graphite/diamond/liquid triple point, see Fig.1, we need at least two OP's, which may be multi-component and depend on three spatial coordinates. To describe crystallization we use the approach of Ramakrishnan and Yussouff [37] where the authors proved that "the lattice periodic component of the density is ... an order parameter" for freezing transition. In the Landau-Gibbs free energy proposed below the *effective scalar crystallization* OP η that distinguishes a solid state from a liquid one may be interpreted as the crystal-lattice Fourier component of the density.

Dmitriev et al [38-39] interpret "the graphite-diamond transition … as a transition between two low-symmetry ordered phases, which are derived from a common disordered

hexagonal latent parent phase". It was also found in [38-39] that "an essential parameter appears to be the degree of occupancy of the latent unit cell by the atoms (i.e., the concentration)." The treatment in [38-39], however, did not produce a phase diagram of carbon as a real material, which should be accomplished by our model. That is why we will be using an *effective scalar structural* OP ξ associated with the graphite-diamond transition, which describes the most favorable path between the graphite and diamond phases in the multi-dimensional space of the structural OP's.

Diversity of atomic configurations of solid carbon is usually characterized by the *average coordination number* C, which is defined as the number of other atoms directly linked to the specified atom. In the literature [13, 23] one may find a working definition of the average coordination as the number of neighbors in a sphere of certain radius, usually about 1.85 Å. On the microscopic scale the average coordination number relates to the state of atomic hybridization: sp^3, sp^2 or sp^1. On the macroscopic scale C is connected to the properties of the material; e.g. the molar density ρ of carbon structures [16, 17, 23]. As the definition of C relates to the coarse-grained nature of the effective OP's, their physical meaning may be clarified through the relationship with ρ: $C=\Phi\{\rho(T,P;\eta,\xi)\}$, where the density of the system in the entire domain of variation of temperatures and pressures can be found using Eq.(6).

A reliable relationship $C=\Phi\{\rho\}$ for different structural modifications of carbon should be a subject of an independent study. In this paper we use a linear approximation of this relationship; such approximation was found to be approximately correct in amorphous carbon [16, 17, 23]. As the function $C=\Phi\{\rho\}$ must pass through the densities of graphite ($\rho=\rho_G$, C=3) and diamond ($\rho=\rho_D$, C=4), it can be expressed as follows:

$$C(T,P,\eta,\xi)=3+\frac{\rho(T,P,\eta,\xi)-\rho_G(T,P)}{\rho_D(T,P)-\rho_G(T,P)} \tag{17}$$

This relationship spreads beyond the values of graphite and diamond phases into the domains of densities typical for the liquid carbon and high-energy phases.

II.1.2.2 Gibbs Free Energy of Carbon

Although the energies of formation of different carbon structures are very close, they must be separated by high activation barriers, which provide their stability in a wide range of conditions. For instance, diamond is stable at room temperature and pressure although it is thermodynamically unstable against graphite phase under these conditions. Both transitions, structural and crystallization, are of the first-order; hence, the free-energy function of carbon must be a polynomial of the order not less than fourth and include the terms of the third order in ξ and η. The OP's coupling must start with the bi-quadratic term and have the form that excludes the stability of the phases other than diamond, graphite, and liquid. On the basis of these facts we propose the following form of the Landau-Gibbs free energy:

$$\begin{aligned} G(T,P;\eta,\xi) &= Q+\frac{1}{2}A_\eta\omega^2(\eta)+B_\eta\nu(\eta) \\ &+\frac{1}{2}A_\xi\omega^2(\xi)+B_\xi\nu(\xi)+J\nu(\xi)\nu(1-\eta) \end{aligned} \tag{18a}$$

where A's, B's, Q, and J are functions of (T, P), which should be determined through the comparison with the phase diagram of carbon. The OP's can always be scaled such that their

values at the stable phases are near 0 and 1; this constraint allows us to select the functions ω(x) and ν(x) as

$$\omega(x) = x(1-x); \quad \nu(x) = x^2(3-2x) \tag{18b}$$

The equilibrium phases—graphite, diamond, and liquid—can be found among the critical points (ξ_C, η_C) of the free energy G, Eq.(18), that is, the solutions of the following simultaneous equations:

$$\begin{aligned} \frac{\partial G}{\partial \xi} &= \omega(\xi)[A_\xi \omega'(\xi) + 6B_\xi + 6J\nu(1-\eta)] = 0 \\ \frac{\partial G}{\partial \eta} &= \omega(\eta)[A_\eta \omega'(\eta) + 6B_\eta - 6J\nu(\xi)] = 0 \end{aligned} \tag{19}$$

Eqs.(19) can be easily resolved and the critical points (ξ_C, η_C) can be found as the intersections of the pairs of the critical lines from the following two sets:

$$\xi_0 = 0; \qquad \xi_t = \frac{1}{2} + \frac{3}{A_\xi}[B_\xi + J\nu(1-\eta)]; \qquad \xi_1 = 1 \tag{20a}$$

$$\eta_0 = 0; \qquad \eta_t = \frac{1}{2} + \frac{3}{A_\eta}[B_\eta - J\nu(\xi)]; \qquad \eta_1 = 1 \tag{20b}$$

According to the definition presented above, a phase is a locally stable homogeneous state of a system. Hence, to identify the OP's of the phases we have to verify Eq.(3) for the critical points (ξ_C, η_C). As the second-order partials of G are:

$$\begin{aligned} \frac{\partial^2 G}{\partial \xi^2} &= A_\xi\{\omega(\xi)\omega''(\xi) + [\omega'(\xi)]^2\} + 6\omega'(\xi)[B_\xi + J\nu(1-\eta)] \\ \frac{\partial^2 G}{\partial \eta^2} &= A_\eta\{\omega(\eta)\omega''(\eta) + [\omega'(\eta)]^2\} + 6\omega'(\eta)[B_\eta - J\nu(\xi)] \\ \frac{\partial^2 G}{\partial \eta \partial \xi} &= -36J\omega(\xi)\omega(\eta) \end{aligned} \tag{21}$$

the condition, Eq.(3), will be satisfied if we choose the phases as following: *Liquid*=(ξ_0, η_0); *Diamond*=(ξ_0, η_1); *Graphite*=(ξ_1, η_1). Such choice of phases helps identify parameters Q, B_ξ, and B_η of the free energy, Eq.(18), as following:

$$\begin{aligned} Q &= G_L(T,P) \\ B_\eta &= G_D(T,P) - G_L(T,P) \equiv \Delta G_{D/L} \\ B_\xi &= G_G(T,P) - G_D(T,P) \equiv \Delta G_{G/D} \end{aligned} \tag{22}$$

where $\Delta G_{D/L}$, $\Delta G_{G/D}$ may be called the *driving forces* of the respective transitions.

The free energy, Eqs.(18, 22), has another critical point—(ξ_1, η_0) with liquid-like OP η. As pointed out in the Introduction there is no LLPT in the carbon system. To exclude the second liquid phase from our system we assume that this state represents a saddle point of the free energy:

$$\eta_t(\xi = \xi_1) = \eta_0. \tag{23}$$

This yields a constraint on the interaction parameter J:

$$J = \frac{1}{6}A_\eta + \Delta G_{D/L} \tag{24}$$

Thus the molar Gibbs free energy of carbon takes the form:

$$\begin{aligned} G(T,P;\eta,\xi) = G_L &+ \frac{1}{2}A_\eta\,\omega^2(\eta) + \Delta G_{D/L}\,\nu(\eta) \\ &+ \frac{1}{2}A_\xi\,\omega^2(\xi) + \Delta G_{G/D}\,\nu(\xi) \\ &+ (\frac{1}{6}A_\eta + \Delta G_{D/L})\nu(\xi)\nu(1-\eta) \end{aligned} \tag{25}$$

where A_η, A_ξ are called the *barrier-height coefficients* because at equilibrium the phases are separated by the free energy barrier of the height A/32. Notice that redefinition of the OP's does not change the heights of the free energy barriers.

Figure 3 represents a phase map—the critical lines in the plane (ξ, η)—of the Landau-Gibbs free energy, Eq.(25), with the values of $G_{L(G,D)}(T, P)$ obtained from [8] and parameters, A_η, A_ξ identified in the following sections. The stable (and metastable) phases satisfy the conditions of Eqs.(3, 21) and the saddle points represent the transition states between the phases. In Figure 4 is depicted the stereoscopic projection of the Landau-Gibbs free energy, Eq.(25), as a function of OP's (ξ, η) at the same point in the (P, T)-phase diagram of Fig.1 as in Fig.3 that is, on the graphite melting line.

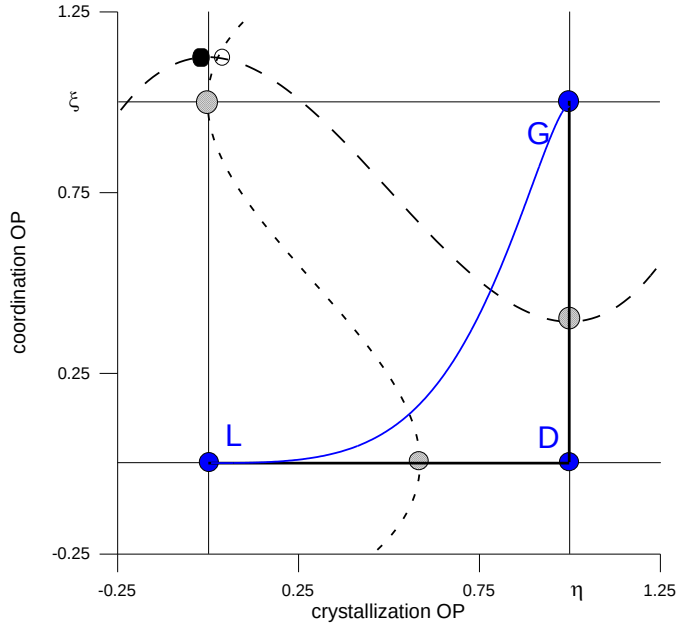

Fig. 1.3. (Color online). Phase map—plane of the structural and crystallization OP's—for the 'black triangle' point (T=4000K, P=6.7GPa) on the graphite melting line in Fig.1. Black lines are the critical lines, Eqs.(20); solid lines: $\xi=\xi_{0,1}$ and $\eta=\eta_{0,1}$; dashed lines: $\xi=\xi_t(\eta)$ and $\eta=\eta_t(\xi)$. Circles are the critical points (ξ_C, η_C): full blue circles—stable phases, full black circle—metastable state, crosshatched circles—saddle points, open circle—local maximum of the free energy. Thick lines—trajectories that represent the interfaces: black—diamond/graphite and diamond/liquid-carbon, blue—graphite/liquid-carbon.

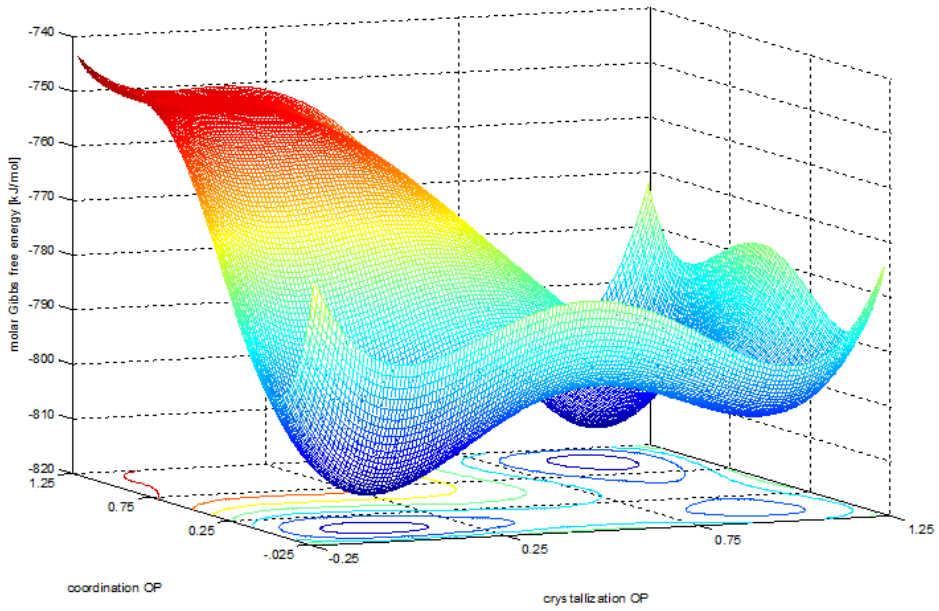

Fig. 1.4. (Color online). Stereoscopic projection of the Landau-Gibbs free energy, Eq.(25), for the conditions of Fig.1.3.

The free energy density of the continuum theory, Eqs.(13, 25), contains a set of coefficients, the barrier-height A's and the gradient-energy κ's. For instance, inclusion of the gradient energy contributions into the theory accounts for the heterogeneities of the material, which in the case of carbon are due to the stretching and bending of atomic bonds that is, stresses in the system. As these coefficients are not standard, tabulated properties of materials one needs to find means of estimating them. For the consistency of the continuum theory it is preferable to estimate them *directly* from the *ab initio* calculations. Because this problem is not solved yet, in the following two sections the coefficients (A_η, κ_η) and (A_ξ, κ_ξ) will be identified *indirectly* via the comparison with the appropriate quantities obtained from the results of the simulations of nucleation of diamond phase from graphite and liquid carbon. We will also estimate the (T, P)-dependence of these coefficients using the data on stability of carbon phases.

II.1.2.3 Diamond/Graphite Coexistence

As known, the interfacial energy plays a major role in the processes of nucleation and epitaxial growth of one phase on the surface of another, e.g. diamond on graphite [16]. To calculate the excess of the total energy of a non-hydrogenated graphite/diamond interface Lambrecht *et al* [40] used the method of continuous matching of diamond and graphite planes for two possible structures: (i) two $(1\bar{1}00)$ graphite planes matching three $(1\bar{2}1)$ diamond

planes and (ii) two $(11\bar{2}0)$ graphite planes matching three $(10\bar{1})$ diamond planes. The coherency of the graphite/diamond interface will be warranted in both cases if three {111} diamond planes match up with two {0001} graphite planes. The model yielded quantitative structures of the interfaces at 0K where the excess energy was "essentially due to (the presence of) the dangling bonds". For the magnitudes of $\sigma_{D/G}$ the authors found: (i) 1.7J/m^2 and (ii) 2.5J/m^2; they argued that this result explained the fact that type-(i) interface is the most frequently observed in the experiments.

The interfacial structure presented in [40] allowed us to estimate the thickness of the interface $l_{D/G}$. In addition to sp^2-sp^2 and sp^3-sp^3 bonds, the interface includes sp^2-sp^3 and dangling bonds. As it can be expected, the graphite planes are affected greater by the coherent matching than those of the diamond phase. We estimate that two layers of the graphite, two layers of the transition zone, and one layer of the diamond phase are affected by the transition. Then, taking into account angular orientation of the diamond bonds and using the value of 1.42Å for the average bond length, the total thickness of the type-(i) interface $l_{D/G}$ comes to about 0.57nm. Although this result was obtained from the analysis of one orientation only, it provides a good starting point for numerical analyses of the model.

In the continuum theory a phase-separating interface is described by the interfacial energy σ and thickness l from Eqs.(10). In the present subsection we consider the solid-state transformation of carbon between the diamond and graphite phases. As the terminal phases of the transformation path defined by the free energy, Eq.(25), have the same crystallization OP $\eta=\eta_1$, the entire diamond/graphite interface may be described by Eqs.(12) with only one, structural OP ξ, varying (the thick black vertical line in Fig.3). Then we obtain (see details in [36]):

$$\sigma_{D/G}=\frac{1}{6}\sqrt{\kappa_\xi A_\xi}\,\frac{\ln V_G/V_D}{V_G-V_D},\qquad l_{D/G}=4\sqrt{\frac{\kappa_\xi}{A_\xi}} \tag{26}$$

Given the estimates of $l_{D/G}$ and $\sigma_{D/G}$ for the type-(i) graphite/diamond interface and the magnitudes of V_G=5.082cc/mol, V_D=3.406cc/mol, we estimate the magnitudes of the barrier-height A_ξ and gradient-energy κ_ξ coefficients at (T=0K, P_E=1.36GPa) as follows:

$$\begin{aligned} A_\xi &= 24\,\frac{\sigma_{D/G}}{l_{D/G}}\,\frac{V_G-V_D}{\ln V_G/V_D}\approx 300.\frac{kJ}{mol};\\ \kappa_\xi &= \frac{3}{2}\,\sigma_{D/G}\,l_{D/G}\,\frac{(V_G-V_D)}{\ln V_G/V_D}\approx 0.609\times10^{-15}\,\frac{J\,m^2}{mol}. \end{aligned} \tag{27}$$

The activation barrier height at equilibrium, $A_\xi/32\approx$9.4kJ/mol (~0.1eV/atom) can be compared with the driving force for the diamond-to-graphite transition at (0K, 0GPa), which, using the data of [4], can be estimated as 2.7kJ/mol, and the thermal energy at (300K, 0GPa) of 2.5kJ/mol. We can conclude that the activation barrier significantly impedes transition of diamond to the more stable graphite phase as the experiment shows. In Fig.2 are depicted the Gibbs free energies of graphite and diamond phases and the transition state versus pressure at 0K. As the results of [40] are applicable only to the specific direction of matching diamond and graphite planes, the magnitudes of A_ξ and κ_ξ should be orientation sensitive.

Fahy, Louie, Cohen [7], using the density-functional theory with an *ab initio* pseudopotential and the interlayer distance as a free parameter, calculated the activation

barrier between rhombohedral graphite and diamond to be 0.33eV/atom. This estimate, which seems to eliminate practically any thermally activated diamond–graphite transition at temperature below 2000 K, is significantly greater than ours not only because they considered a rhombohedral modification of graphite. Greater difference comes from the fact that they considered a homogeneous single-crystal graphite/diamond transformation without any dangling bonds while we consider an interface that is, a heterogeneous structure, which requires the dangling bonds even when it is coherent. The experimental value can be even less if the mechanism of termination of the dangling bonds by sp^1 carbon atoms is essential.

In the same paper [7] the authors predicted disappearance of the need for thermal activation of the transition of rhombohedral graphite into diamond at (0K, 80GPa). This fact may be interpreted as attainment of the graphite spinodal point of the free energy, Eq.(25), see Fig.2. Then, using Eqs.(2, 20, 22), and the data of [4], we obtain that A_ξ(0K, 80GPa)=$6\Delta G_{G/D}$(0K, 80GPa)≈441.kJ/mol. Using a linear approximation for the pressure dependence of the coefficient A_ξ we can estimate $\partial A_\xi/\partial P \approx 1.79$ cm^3/mol. Notice that $\partial A_\xi/\partial P \approx V_G - V_D$.

The conclusion of [40] that high value of the diamond/graphite interfacial energy mostly is due to the significant number of dangling bonds on the interface allows us to estimate the slope of the temperature dependence of the barrier-height coefficient A_ξ. Indeed, any process that causes termination of the dangling bonds will decrease $\sigma_{D/G}$ and the coefficient A_ξ. Three mechanisms may be responsible for termination of the dangling bonds on the diamond/graphite interface: sp^1-hybridization, hydrogenization, and generation of 'free' electrons. In the present paper we will consider only the latter. The structure of the interface yields the number of the interface dangling bonds of about 5×10^{18} m^{-2}. Generation of 'free' electrons is a thermally activated process; at 4000K the bulk concentration of 'free' electrons (1.5×10^{24} m^{-3}) will be sufficient to saturate all dangling bonds with the electrons. If we estimate the energy decrease from trapping an electron on the dangling bond to be ~1eV, we arrive at the interface energy reduction of 0.8 J/m^2. Then, assuming that $l_{D/G}$ and the average molar volume do not change much with temperature, we can estimate from Eq.(27) the slope of the temperature dependence of the barrier-height coefficient to be $\partial A_\xi/\partial T \approx -0.05$ kJ/mol·K. Thus the linear approximation of the barrier-height coefficient takes the form:

$$A_\xi(T,P)[\frac{kJ}{mol}] \approx 297.6 + 1.79\times P[GPa] - 0.05\times T[K] \quad (28)$$

Variation of A_ξ with temperature along the graphite/diamond phase-equilibrium boundary is shown in Figure 5.

As one can see from Eq.(26) the interfacial energy of the carbon system is affected by the phase-transformation compression while the interfacial thickness is unaffected by the volume change. The effect of compression on the interfacial energy can be estimated as follows:

$$e \equiv \frac{\sigma_{D/G}(V_G \neq V_D)}{\sigma_{D/G}(V_G = V_D)} - 1 = \frac{V_G + V_D}{2(V_G - V_D)} \ln\frac{V_G}{V_D} - 1 \quad (29)$$

For the diamond/graphite transition this effect is relatively small, e≈1.4%.

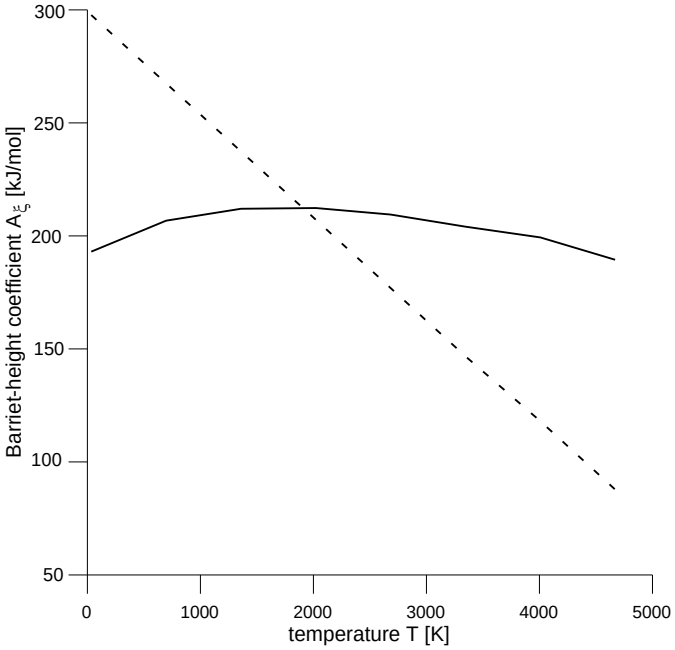

Figure 1.5. Barrier-height coefficient A_ξ (dashed line) and its critical value A_ξ^* (solid line) versus temperature along the graphite/diamond phase-equilibrium boundary.

II.1.2.4 Nucleation of Diamond from Liquid Carbon

Ghiringhelli et al [14] conducted MD simulations of nucleation of diamond phase from liquid carbon using a semiempirical many-body potential that has been fit to the properties of solid and liquid carbon phases. The entire simulation box contained 2744 particles. The successful attempt at T_A=5000K and P_A=85GPa ('blue diamond' in Fig.1) corresponded to the chemical potential difference (driving force) of $\Delta\mu_A=0.60k_BT_A$. It resulted in the creation of a critical nucleus of N_A=110 carbon atoms with the number density of $\rho_A=191\text{nm}^{-3}$ and the total Gibbs free energy excess of $\Delta G_A=25k_BT_A$. These numerical results were fitted into the Classical Nucleation Theory (CNT). Although the authors have to be complimented for their attempt to obtain the quantitative information regarding the nucleation process, one has to notice that matching their data to CNT was not justified because neither of the regular CNT assumptions—that a new-phase nucleus contains large number of atoms, the interface between the new and parent phase is infinitely thin, or that the interfacial energy is independent of the driving force—was satisfied in their case. For instance, we will show below that most of the volume of the critical nucleus was covered by the interfacial region.

The continuum theory provides a much better platform for comparison with the MD numerical simulations then CNT because neither of the CNT assumptions is used in the continuum theory. In Appendix, using the continuum theory, we derived the expressions for the total Gibbs free energy excess ΔG_{cn} and number of moles N_{cn} of the critical nucleus of a new phase in the infinite amount of the parent phase. These expressions were used to formulate a routine for the identification of the parameters of the continuum theory. Below this routine will be used for the parameters A_η and κ_η. For the free energy, Eq.(25), the terminal phases—diamond and liquid carbon—have the same structural OP $\xi=\xi_0$. Hence, the whole system of diamond nucleus in liquid carbon corresponds to $\xi=0$ (the thick black horizontal line in Fig.3). As the compression effect for diamond/graphite transition is rather small (see Eq.(29) and below) and $V_L-V_D \ll (V_L+V_D)/2$ at high temperature, we neglect this effect for the diamond/liquid-carbon system.

According to the routine developed in Appendix, one has to numerically resolve Eq.(A19) where the left-hand side is a particular function, $H(\eta_t)$, represented in Fig.A2 and the right-hand side is a number α obtained from experiments or simulations. Comparing the continuum-theory quantities with their numerical counterparts from Refs.[8, 14] we find that $\Delta\mathcal{G}_{cn}=\Delta G_A$, $\Delta G_{D/L}=\Delta\mu_A N_{Av}$, and $N_{cn}=N_A N_{Av}$ where N_{Av} is the Avogadro number. Hence:

$$\alpha \equiv \frac{\Delta G_{cn}}{N_{cn}\Delta G_{D/L}} = \frac{\Delta G_A}{N_A \Delta\mu_A} = -0.379$$
$$V_{cn} \equiv \frac{N_{cn}}{\bar{\rho}} = \frac{N_A}{\rho_A} = 0.576\,nm^3 \qquad (30)$$

Then, the numerical solution of Eq.(A19) yields (see Fig.A2):

$$\eta_t(\alpha) = 0.334. \qquad (31)$$

Application of Eq.(A20) yields the values of the coefficients A_η and κ_η at (T=5000K, P=85GPa):

$$A_\eta = \frac{6|\Delta\mu_A| N_{Av}}{1-2\eta_t(\alpha)} = 374.\frac{kJ}{mol}$$
$$\kappa_\eta = A_\eta \left\{ \frac{V_{cn}}{4\pi I_1[\eta_t(\alpha)]} \right\}^{2/3} = 2.46\times10^{-15}\,\frac{J\,m^2}{mol} \qquad (32)$$

Using the values of A_η and κ_η we can estimate the diamond/liquid interface energy and thickness as following:

$$\sigma_{D/L} = \frac{\bar{\rho}}{6}\sqrt{\kappa_\eta A_\eta} = 1.603\,\frac{J}{m^2},$$
$$l_{D/L} = 4\sqrt{\frac{\kappa_\eta}{A_\eta}} = 0.324\,nm \qquad (33)$$

The present estimate of the diamond/liquid interfacial energy is in good but not perfect agreement with that of [14], 1.86 J/m^2, obtained through the comparison with CNT. We argue here that our estimate is more consistent. Indeed, given the volume of the critical nucleus in [14] of 0.576 nm^3 (see Eq.(30)) and assuming that it was a sphere, its radius would be 0.516nm. Comparing this estimate with that of the interfacial thickness, Eq.(33), we can see that the thickness of the interface is more than a half of the radius of the critical nucleus. In Figure 6 is depicted OP η versus the scaled distance from the center of the critical nucleus of diamond in liquid carbon. The graph also shows that the transition zone occupies a large portion of the critical nucleus. Thus, at least one assumption of CNT was not satisfied in the simulations of [14].

Also in Fig. 6 is depicted variation of the average coordination number C, defined by Eq.(17), along the radius of the critical nucleus of diamond in liquid carbon. Notice that the

coordination number changes more abruptly from the diamond-like to liquid-like value in the transition zone than the OP. Another important feature to notice is that in the liquid phase the average coordination number falls below the value of 3, which on the microscopical level means presence of sp^1 hybridized atoms. Although this may be an artifact of the linear relationship, Eq.(17), it may also contain certain physical significance. Modeling of liquid and amorphous carbon shows that sp^1-carbon can be present in both materials, although not in high concentration. For instance, the fraction of sp^1-carbon in liquid carbon around the triple point can be as high as 15% although diamond and graphite remain essentially sp^1-carbon free. This means that sp^1-carbon plays an important role in transition states, mostly facilitating the continuity of the network and helping to eliminate the dangling bonds.

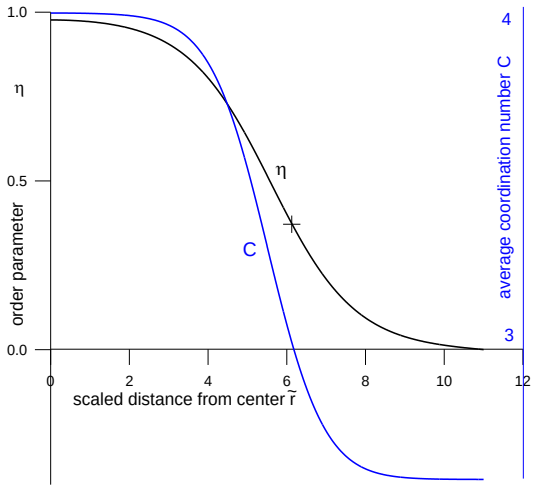

Fig. 1.6. (Color online). Order parameter η and average coordination number C versus the scaled distance from the center of the critical nucleus of diamond in liquid carbon at (T, P) that corresponds to the blue diamond point on the phase diagram of Fig. 1. (+)—transition state $\eta_t(\alpha)$.

II.1.3 Applications of The Theory

II.1.3.1 Graphite/Liquid-Carbon Interfacial Energy

A natural application of the developed model is to the problem of crystallization of graphite from liquid phase. Out of many aspect of graphite crystallization only the structure of the solid/liquid interface and the interfacial energy, $\sigma_{G/L}$, at the graphite melting line (the 'black triangle' point on the phase diagram in Fig.1) will be considered here. The difference from the previously considered cases of diamond/liquid and diamond/graphite interfaces is that now both OP's, η and ξ, vary along the coordinate axis perpendicular to the plane of the interface. Hence, the 1D open-system equilibrium-state boundary-value problem for the graphite/liquid interface includes simultaneous equations, Eq.(11a), for both OP's. In addition to the driving forces of both processes—crystallization and structural—our model depends on the two sets of barrier-height and gradient-energy coefficients. These coefficients were identified in the previous section but at the temperatures and pressures different from those of the 'black triangle'. In the calculations below we used Eq.(28) for the coefficient A_ξ; all other coefficients were assumed to be temperature and pressure independent. The system of simultaneous equations was numerically solved and a separatrix that satisfies the boundary conditions, Eqs.(11b) was found. In Fig. 3 is depicted the projection of the separatrix on the plane (η, ξ). In Figure 7 are shown the spatial distributions of OP's and scaled molar Gibbs

free energy, Eq.(25), along the coordinate axis perpendicular to the plane of the interface. Compare Figs. 3, 7 and notice that although the trajectory of the representative point of the interface crosses two critical lines, $\xi=\xi_t(\eta)$ and $\eta=\eta_t(\xi)$, Eqs.(20), there is actually only one Gibbs free energy barrier on the path of this point.

Numerical calculations of the graphite/liquid interfacial energy, Eqs.(14, 25), produced the value:

$$\sigma_{G/L} = 1.66 \frac{J}{m^2}. \qquad (34)$$

Notice that this value is comparable to $\sigma_{D/L}$ and $\sigma_{G/D}$.

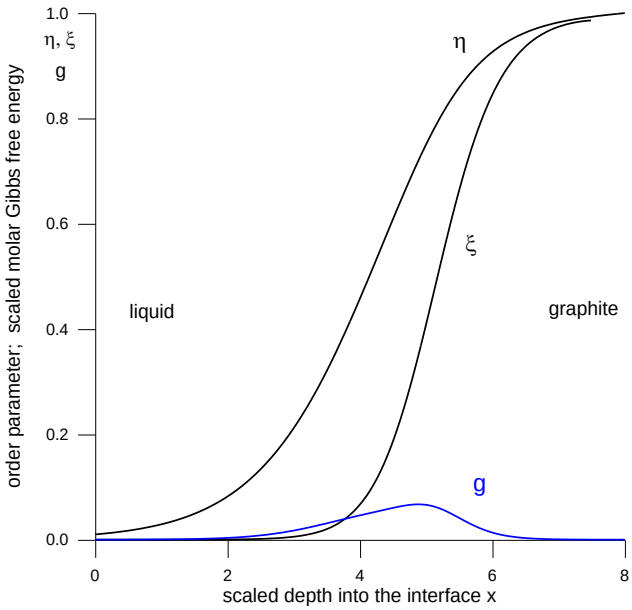

Fig. 1.7. (Color online). Spatial distribution of the crystallization OP, η, and structural OP, ξ, and scaled molar Gibbs free energy $g=(G-\mu)/A_\eta$ (blue line) for the graphite/liquid interface at (T, P) that corresponds to the 'black triangle' point on the phase diagram of Fig. 1.

II.1.3.2 Nanostructured Amorphous Carbon

In Sec.II.2 we discussed a possibility for a transition state to become thermodynamically stable in a closed system if the conditions of Eqs.(16, 17) are fulfilled. In the present section we apply these conditions to the system described by Landau-Gibbs free energy, Eq.(25). Eq.(16) can be expressed as an inequality for the barrier-height coefficient:

$$A_\xi(T,P_E) < A_\xi^* \equiv 8(V_G - V_D)^2 \left| \left(\frac{\partial V}{\partial P}\right)_G + \left(\frac{\partial V}{\partial P}\right)_D \right|^{-1} \qquad (35)$$

where its critical value, A_ξ^*, depends only on the equilibrium properties of the phases and is proportional to the transformation shrinkage squared[2]. In Fig.5 the coefficient A_ξ, Eq.(28), and its critical value A_ξ^* are shown as functions of T along the graphite/diamond phase-equilibrium boundary. As one can see the condition of Eq.(35) is fulfilled for T>2000K.

[2] The critical value in Eq.(35) is 9/8 times greater if only the local stability of the transition state is required as opposed to the global one.

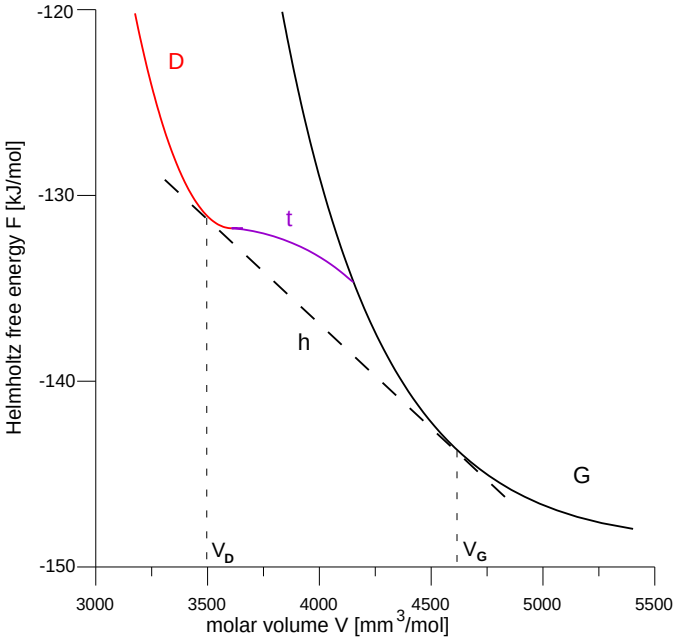

Fig. 1.8. (Color online). Helmholtz free energy F of the diamond (D) and graphite (G) phases, the transition (t) and heterogeneous (h) states as functions of the molar volume V at T=4000K using the calculations of [8] and Eq.(30).

In Figure 8 the graphite and diamond phases and the transition state are represented by their molar Helmholtz free energies as the functions of molar volume at 4000K. One can see that there is a certain domain of molar volumes where the transition state has less Helmholtz free energy (more stable) than both bulk phases. Compare Fig.8 with Fig.2 and notice that the transition state has greater Gibbs free energy than both bulk phases for the same pressure. This means that although this state is not a stable phase under conditions of fixed pressure it can be stable under the conditions of fixed volume. However, the heterogeneous state that is, a mixture of graphite and diamond phases has lower Helmholtz free energy than any of the homogeneous ones in the domain between the equilibrium values of the molar volumes of the bulk phases (V_D, V_G). This means that in a closed system of the average molar volume from this domain a macroscopic (large enough) piece of carbon will break up into coexisting phases of diamond and graphite. The situation changes dramatically in nanostructures with the dimensions less than the critical size, Eq.(17): according to the analysis of [36] the transition state becomes globally stable (that is, with respect to all fluctuations of ξ) against the graphite and diamond phases and a mixture of the two.

Stabilization of the diamond/graphite transition state under the closed-system conditions allows us to conjecture that this state corresponds to the nanostructured amorphous carbon (na-C), which, as it was pointed out in the Sec.I, is thermodynamically stable to a certain degree. Notice that formation of the stable na-C should be orientation dependent.

The above presented conjecture allows us to interpret results of the experiments on FIB irradiation of the surface of the single crystal CVD diamond film [18-20]. Ga^+-ion-beam scanning irradiation of the films produced nanodots and nanowires of the width approximately equal to the diameter of the beam that is ~20nm [18-20]. The nanostructures were stable at the room temperature; their conductivity was smaller than that of the graphite but greater than that of the diamond. When annealed at approximately 1000°C for 15-20 min the conductivity of the nanostructures always increased approaching that of the graphite phase. In the experiments of [18-20] the phase content of the nanostructures remained

undetermined with the amorphous phase being a candidate. Irradiation of the film creates high temperature and pressure in the affected zone. However, there is no evidence that the irradiated material in these experiments was molten at any time and we assume that the entire transformation path passed in the solid state. Ga^+ ions most likely do not remain in the nanostructures because Ga does not form compounds with carbon. Then, according to the criterion, Eqs.(35), at the temperature and pressure of irradiation the condition for the stabilization of the amorphous phase was met, see Fig.5. The support for the amorphous structure of the produced states comes from the observed limited conductivity of the irradiated materials, which is due to the partial hybridization of the transition state, $0<\xi_t<1$. When the temperature decreases the amorphous phase becomes unstable but the slow kinetic processes do not allow the material to achieve the thermodynamic equilibrium state—the graphite phase. During annealing the kinetic processes speed up significantly which helps the system to restore thermodynamic equilibrium that is, transform the nanostructure into the stable graphite phase ($\xi_G=0$).

The present theoretical study applies to a closed system of fixed volume, which is not completely the case for the surface irradiation experiments. To verify the theoretical predictions of the present research it would be very interesting to conduct an irradiation experiment where the transformation takes place completely under the surface of the film that is, in the bulk of a carbon film. This may be achieved by means of focused high energy ion irradiation [41-42], which is known to produce buried amorphous nanoclusters in diamond.

II.1.4 Discussion

In this paper we build a continuum theory of carbon phases, which ties up many seemingly unrelated data on carbon system. For the consistency of the theory it would be preferential to use the data from the same work or at least the works that use similar methods. Unfortunately such data are not available at present. That is why we used the data of a few different studies, which nevertheless we find quite consistent. The theory describes transformations between graphite, diamond and liquid carbon with the help of a Landau-Gibbs free energy which, in addition to temperature and pressure, depends on two order parameters: crystallization and structural. The thermodynamic data on the equilibrium (stable and metastable) phases were obtained from the database of [4] for low temperatures and the numerical study of carbon system in [8] for high temperatures. The Landau-Gibbs free energy contains two barrier-height and two gradient-energy coefficients, which were calculated from the data obtained in the studies of nucleation of diamond on graphite [40] and from liquid-carbon [14]. The results of [40] are applicable only to the specific, most favorable, diamond/graphite matching direction, which means that out of a few possible diamond/graphite barriers the value determined here is the lowest. On the microscopic level, in the transition zone the diamond crystal, which incorporates atoms with rigid sp^3 bonds, should match another carbon phase—liquid or graphite—composed of atoms with predominantly sp^2 bonds. As a result, there are certain similarities between the barrier heights of the two interfaces. Thus, similarity of the values of the diamond/graphite and diamond/liquid-carbon barrier-height coefficients, A_η and A_ξ, Eqs.(27, 32), is due to similarities of the transition regions as opposed to the terminal phases because structurally graphite and liquid carbon are very different. The disparity of the values of the gradient-energy coefficients, κ_ξ and κ_η, Eqs.(27, 32), with the latter being more than 4 times greater than the former can be explained by significantly greater level of stress in the diamond/graphite interface than in the diamond/liquid one. The boundary of the absolute stability of the graphitic phase, which was attained in the numerical calculations of the graphite-diamond transition in [7], we interpret here as the spinodal point of the Landau-

Gibbs free energy. This result allowed us to calculate the pressure dependence of the coefficient A_ξ. The temperature dependence of this coefficient was estimated on the bases of the conclusion in [40] that high value of the diamond/graphite interfacial energy mostly is due to the significant number of dangling bonds on the interface. We have not found data in the literature that would allow us to estimate the temperature-pressure dependencies of other coefficients.

The continuum model yielded the value of 1.603 J/m^2 for the diamond/liquid-carbon interface energy as opposed to 1.86 J/m^2 obtained in [14] by comparing the MD simulation results with the Classical Nucleation Theory. We believe that our value is more consistent because it is not based on the comparison with CNT, which is not applicable here. The calibrated theory was also used for the analyses of the graphite/liquid-carbon interface energy, which can be used for numerical simulations of graphite crystallization and, to the best of our knowledge, has not been published yet. The obtained value of graphite/liquid-carbon interface energy, 1.66 J/m^2, is comparable to that of diamond/liquid-carbon and can also be explained by the similarities of the transition regions.

The diamond/liquid and graphite/liquid interfacial energies can be compared with the crystal/liquid interfacial energies of other elements of group IV of the periodic table. The values of the latter quantities acceptable for the comparison were obtained in numerical experiments using cleaving or capillary-fluctuation methods. They are (in J/m^2): 0.34÷0.42 for silicon (depending on the orientation of the interface) [43][3], 0.165 for germanium, 0.055 J/m^2 for tin [45], and 0.057(4) for lead [46]. As one can see the interfacial energies of these materials depend strongly on the bond energies of the elements, with carbon being a strongly covalent material with the highest bond energy and tin and lead—a metal or semimetal with the least bond energy. A similar trend can be found in the surface energies (crystal/vapor) of C, Si and Ge where, however, the role of orientation and surface reconstruction is much more important [47].

We also analyzed stability of nanostructured amorphous carbon (na-C) and were able to interpret na-C as the transition state of the Landau-Gibbs free energy function. This conjecture helped us to explain results of the experiments on amorphization of carbon under conditions of FIB irradiation of CVD-diamond nanofilms [18-20]. Regardless of the theoretical interpretation, we think that the term 'amorphous carbon' is a misnomer. The problem with such nomenclature is that amorphization is usually associated with crystallization when amorphous state is understood as a failed crystal [48]. It should be distinguished from a phase or state that emerges as a result of an entirely solid-state transformation. For the lack of a better term such phases may be called *disordered solid phases*.

The present model may be extended to include other structural modifications of carbon. To include a carbine phase with predominantly sp^1 hybridization of carbon atoms the free energy $G(\eta, \xi)$ should have another minimum in the (η, ξ)-domain that corresponds to the average coordination number $C\approx2$. For the model to include other solid phases, e.g. BC-8 or hexagonal carbon, the free energy $G(\eta, \xi)$ should have additional minimum in the domain $\eta>1$ or a third OP should be introduced.

Kinetics of the transformations is another direction of expansion of the present theory. It is possible to extract the kinetic coefficients from the numerical simulations of diamond nucleation rate in [14]. These data may be used for the large-scale modeling of graphite and diamond crystallization. The suggested framework may also be applied to an entirely

[3] Another value obtained experimentally, 0.68-0.69 at melting temperature and decreasing to about 0.32 for lower temperatures, is given in [44], but seems to be inconsistent here.

different element of tremendous practical significance—silicon. These challenging problems will be dealt with in the later publications.

II.1 Appendix: 3D Critical Nucleus

Proper description of the process of nucleation is an important goal of the continuum theory of phase transitions. Thermodynamic data on the free energy excess and size of a critical nucleus can be successfully used for the identification of the parameters of the continuum method. The general strategy is the following: one obtains values of the free energy excess and volume of the critical nucleus of the new phase using other means of study, e.g. experiment or molecular simulations, and compares them with the similar values obtained by means of the continuum method. Cahn and Hilliard [49] (CH) considered this problem in the limit of a large driving force that is, the free energy difference between the parent and product phases. In the present Appendix the problem will be solved without the simplifying assumptions of the large driving force. The process of nucleation is affected by the difference of the densities of the parent and product phases. However, the compression effect of nucleation is not considered here. For the sake of brevity we will be considering nucleation for a solid phase from liquid, although the results are applicable to many different transformations.

The boundary-value problem for the crystallization OP variation can be obtained from Eqs.(8) in the main text:

$$\kappa\nabla^2\eta = \frac{\partial G}{\partial \eta} \qquad (A1)$$

$$|\nabla\eta| \to 0, \quad \eta \to 0 \qquad for\, \mathbf{x} \to \infty \qquad (A2)$$

$$\mu = G(T,P,\eta=0) \equiv G_L(T,P) \qquad (A3)$$

For a 3D spherically symmetric nucleus: $\nabla^2 = \frac{1}{r^2}\frac{d}{dr}(r^2\frac{d}{dr})$ where r is the distance from the center of the nucleus. For the molar free energy of the system, Eqs.(4, 25), r can be scaled as follows:

$$\tilde{r} = \frac{r}{\delta}; \qquad \delta = \sqrt{\frac{\kappa}{A}} \qquad (A4)$$

and the boundary-value problem, Eqs.(A1-3), takes the form:

$$\frac{d^2\eta}{d\tilde{r}^2} + \frac{2}{\tilde{r}}\frac{d\eta}{d\tilde{r}} + 2\eta(\eta-\eta_t)(1-\eta) = 0, \qquad (A5)$$

$$\frac{d\eta}{d\tilde{r}} = 0 \qquad at \quad \tilde{r} = 0, \qquad (A6)$$

$$\frac{d\eta}{d\tilde{r}} \to 0, \eta \to 0 \quad at \quad \tilde{r} \to \infty, \qquad (A7)$$

that depends only on the transition state OP, Eqs.(20, 22), as an external parameter:

$$\eta_t = \frac{1}{2} + 3\frac{\Delta G_{S/L}}{A} \tag{A8}$$

The solution of the boundary-value problem Eqs.(A5-7) is not a regular trajectory in the space $(\eta, d\eta/d\tilde{r})$ but a separatrix because there are three boundary conditions for a second-order ODE [29]. The problem Eqs.(A5-7) can be solved numerically by selecting a proper initial value $\eta_0 = \eta(\tilde{r} = 0)$ that allows the trajectory to satisfy other three boundary conditions.

The total free energy excess due to presence of the solid nucleus in a previously homogeneous liquid equals:

$$\Delta G_{cn} = G\{T, P, \mathcal{N}, \eta(\mathbf{r})\} - \mu\mathcal{N} \tag{A9}$$

Taking into account the expressions for the total free energy, Eqs.(4,5), and the mole number, Eq.(7), and assuming that densities of the phases are equal $\rho = \bar{\rho} = const(x)$, Eq.(A9) can be written as follows:

$$\Delta G_{cn} = \bar{\rho}\int_{\mathcal{V}} [G(T,P,\eta) + \frac{1}{2}\kappa(\nabla\eta)^2 - \mu]d\mathbf{x} \tag{A10}$$

Using the Gaussian theorem together with the formula $\nabla(\eta\nabla\eta) = \eta\nabla^2\eta + (\nabla\eta)^2$, the equilibrium equation, Eq.(A1), and boundary condition, Eq.(A2), we obtain the relation:

$$\kappa\int_{\mathcal{V}} (\nabla\eta)^2 d\mathbf{x} = -\int_{\mathcal{V}} \eta\frac{\partial G}{\partial\eta} d\mathbf{x} \tag{A11}$$

Then using this relation and the boundary condition Eq.(A3) for Eq.(A10) we obtain the expression for the free energy of the 3D spherically symmetric ($d\mathbf{x}=4\pi r^2 dr$) critical nucleus of solid in liquid:

$$\Delta G_{cn} = 4\pi\bar{\rho}\delta^3\int_0^\infty [G(T,P,\eta) - G_L(T,P) - \frac{1}{2}\eta\frac{\partial G}{\partial\eta}]\,\tilde{r}^2 d\tilde{r} \tag{A12}$$

For the system with the molar free energy, Eq.(25), this expression takes the form:

$$\Delta G_{cn} = 2\pi\bar{\rho}\delta^3 A[\frac{2}{3}(1+\eta_t)I_3 - I_4] \tag{A13}$$

where we used the expressions for the n-th order moments of the OP distribution:

$$I_n(\eta_t) = \int_0^\infty \eta^n \tilde{r}^2 d\tilde{r} \tag{A14}$$

The number of moles in the nucleus is

$$N_{cn} = \int_{\mathcal{V}} \rho\,\eta\, d\mathbf{x}. \tag{A15}$$

For the 3D spherically symmetric nucleus this expression takes the form:

$$N_{cn} = 4\pi\bar{\rho}\delta^3 I_1 \tag{A16}$$

Thus, using Eqs.(A4, 8, 13, 16) we can formulate a routine for the identification of the coefficients A and κ:

1. Solve the boundary-value problem, Eqs.(A5-7), for all appropriate values of η_t.
2. Compute the moments, Eq.(A14), using the solution from #1.
3. Compute the function:

$$H(\eta_t) \equiv \frac{(1+\eta_t)I_3(\eta_t) - \frac{3}{2}I_4(\eta_t)}{(\eta_t - \frac{1}{2})I_1(\eta_t)} \tag{A17}$$

4. From the external data compute the following numbers:

$$\alpha \equiv \frac{\Delta G_{cn}}{N_{cn}\Delta G_{S/L}};\ V_{cn} = \frac{N_{cn}}{\bar{\rho}} \tag{A18}$$

5. Find the value of the transition state OP η_t that satisfies the following equation:

$$H(\eta_t) = \alpha \tag{A19}$$

6. Find A and κ from the following relation:

$$A = \frac{3\Delta G_{S/L}}{\eta_t(\alpha) - \frac{1}{2}};\quad \kappa = A\left\{\frac{V_{cn}}{4\pi I_1[\eta_t(\alpha)]}\right\}^{2/3} \tag{A20}$$

7. If the value of the solid/liquid interfacial energy σ is independently available, verify the obtained values of A and κ by comparing the external value of σ to the continuum expression of the interfacial energy:

$$\sigma = \frac{\bar{\rho}}{6}\sqrt{\kappa A}. \tag{A21}$$

In Figure A1 are plotted the solutions of the boundary-value problem, Eqs.(A5-7), which was numerically solved for the values of $0<\eta_t<0.4$. Notice that a recognizable interface exists only for $\eta_t \geq 0.16$ when the value of the OP at the center of the nucleus is greater than 0.5. In Figure A2 are plotted function $H(\eta_t)$, Eq.(A17), and the moments I_n of orders $n=1\div4$, Eq.(A14). The rest of the routine, (##4-7), depends on the external data and is implemented in the main text.

The CH-routine suggested in [49] has an advantage over the present one (UA) in being able to avoid #5 after scaling out the transition state OP: $\eta \to \eta_t\eta$. The CH-routine assumes that $\eta \ll 1$. As one can see from Fig.A1 the CH-routine is valid for $\eta_t \leq 0.0041$. To estimate the accuracy of the CH-routine for the problem considered in the main text we computed η_t for a

particular value of α=–0.379 (see main text) using both methods: $\eta_{t,UA}(\alpha)$=0.334; $\eta_{t,CH}(\alpha)$=0.227. As one can see from Eq.(A20) and Fig.A2, different routines yield different values of the coefficients A and κ. Obviously, the source of the difference is the fact that the condition η«1 is not satisfied for this value of α.

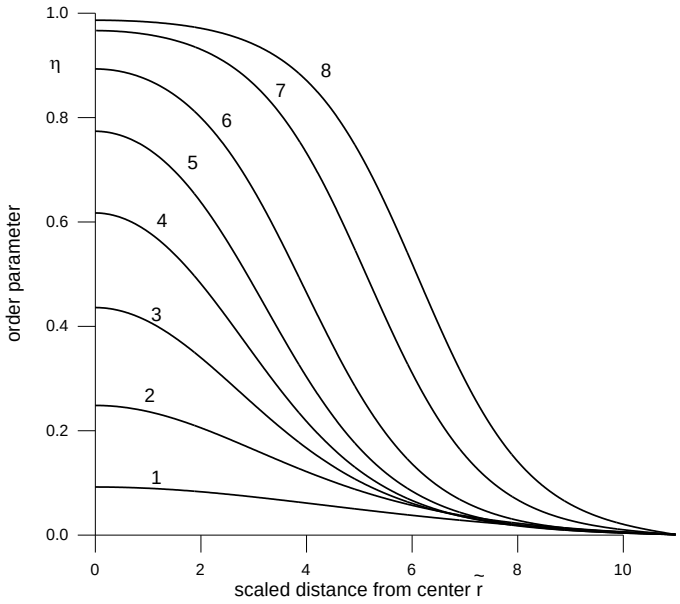

Figure A1. Solutions of the problem, Eqs.(A5-7) for different values of the transition state OP: (1)—η_t=0.0041; (2)—0.0558; (3)—0.1075; (4)—0.1592; (5)—0.2109; (6)—0.2625; (7)—0.3142; (8)—0.3401.

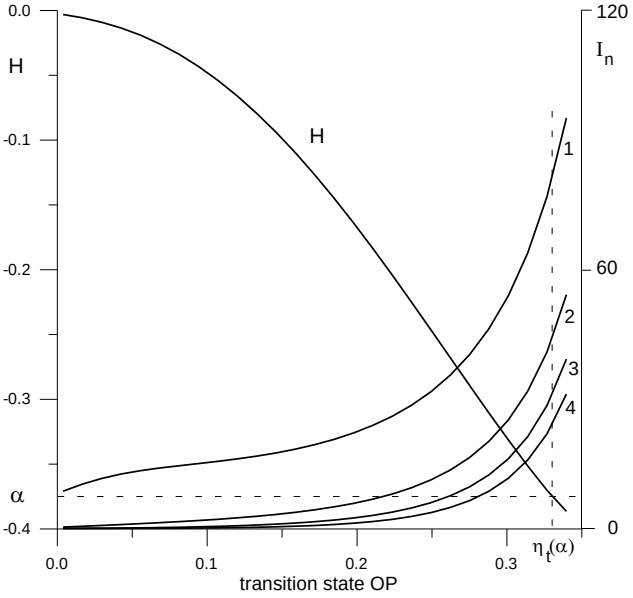

Figure A2. Function H, Eq.(A17), and the n-th order moments I_n (n=1,2,3,4), Eq.(A14), as the functions of the transition state OP η_t. The value of $\alpha$is calculated in the main text.

REFERENCES to Part II.1

1. Bundy FP, Bassett WA, Weathers MS, Hemley RJ, Mao HK, Goncharov AF. The pressure-temperature phase and transformation diagram for carbon; updated through 1994. Carbon 1996; **34**, 141-153.

2. Togaya M. Pressure dependence of the melting temperature of graphite and the electrical resistivity of liquid carbon. Phys. Rev. Letters 1997 **79**; 2474-2477.

3. Brygoo S, Henry E, Loubeyre P, Eggert J, Koenig M, Loupias B, et al. Laser-shock compression of diamond and evidence of a negative-slope melting curve. Nature_Materials 2007; **6**, 274 - 277.

4. Fried LE, Howard WM. Explicit Gibbs free energy equation of state applied to the carbon phase diagram. Phys. Rev. B 2000; **61**, 8734-8743.

5. Mailhiot C, McMahan AK. Atmospheric-pressure stability of energetic phases of carbon. Phys. Rev. B 1991; **44**, 11578-11591.

6. Correa AA, Bonev SA, Galli G. Carbon under extreme conditions: Phase boundaries and electronic properties from first-principles theory. PNAS 2006; **103**, 1204-1208.

7. Fahy S, Louie SG, Cohen ML. Pseudopotential total energy study of the transition from rhombohedral graphite to diamond. Phys. Rev. B 1986; **34**, 1191-1199.

8. Ghiringhelli LM, Los JH, Meijer EJ, Fasolino A, Frenkel D. Modeling the phase diagram of carbon. Phys. Rev. Lett. 2005; **94**, 145701-4.

9. van Thiel M, Ree FH. Theoretical description of graphite, diamond, and liquid phases of carbon. Inter. J. Thermphys. 1989; **10**, 227-236.

10. Glosli J, Ree FH. Liquid-liquid phase transition in carbon. Phys. Rev. Lett. 1999; **82**, 4659-4662.

11. Wu CJ, Glosli JN, Galli G, Ree FH. Liquid-liquid phase transition in elemental carbon: a first-principles investigation. Phys. Rev. Lett. 2002; **89**, 135701-4.

12. Wang X, Scandolo S, Car R. Carbon phase diagram from *ab initio* Molecular Dynamics. Phys. Rev. Lett. 2005; **95**, 185701-4.

13. Fyta MG, Remediakis IN, Kelires PC. Energetics and stability of nanostructured amorphous carbon. Phys. Rev. B 2003; **67**, 035423-6.

14. Ghiringhelli LM, Valeriani C, Meijer EJ, Frenkel D. Local structure of liquid carbon controls diamond nucleation. Phys. Rev. Lett. 2007; **99**, 055702-4.

15. Korsunskaya IA, Kamenetskaya DS, Aptekar IL. Fiz. Metal. Metalloved. 1972; **34**, 942 (Russian); English version in: Phys. Met. Metallogr. (USSR) 1972; **34**, 39.

16. Ferrari AC, Libassi A, Tanner BK, Stolojan V, Yuan J, Brown LM, et al. Density, *sp*3 fraction, and cross-sectional structure of amorphous carbon films determined by x-ray reflectivity and electron energy-loss spectroscopy. Phys. Rev. B 2000; **62**, 11089 - 11103.

17. Casiraghi C, Robertson J, Ferrari AC. Diamond-like carbon for data and beer storage" Materials Today 2007; **10**, 44-53.

18. Zaitsev AM. Carbon nanowires made on diamond surfaces by focused ion beam, Phys. Stat. Solidi (a) 2005; **202** R116-R118.

19. Zaitsev AM, Dobrinets IA. Carbon nanodots made on diamond surfaces by focused ion beam, Physica Status Solidi (a), 2006; **203** R35-R37.

20. Zaitsev AM, Levine AM, Zaidi SH. Temperature and chemical sensors based on FIB-written carbon nanowires. IEEE Sensors J. 2008; **8**, 849-856.

21. Efstathiadis H, Akkerman Z, Smith FW. Atomic bonding in amorphous carbon alloys: A thermodynamic approach", J. Appl. Phys. 1996; **79**, 2954-2967.

22. Akkerman Z, Efstathiadis H, Smith FW. Thermal stability of diamond-like carbon films J. Appl. Phys. 1996; **80**, 3068-3075.

23. Marks NA. Thin film deposition of tetrahedral amorphous carbon: a molecular dynamics study. Diamond Relt. Mater. 2005; **14**, 1223-1231.

24. Liu H, Dandy DS. Studies on nucleation process in diamond CVD: an overview of recent developments. Diamond Relt. Mater. 1995; **4**, 1173–1188.

25. Landau LD. On the theory of phase transitions. Phys. Zs. Sowjet. 1937; **11**, 26-42; see also: Collected Papers of L.D. Landau, Ter-Haar D editor; London; Gordon and Breach, 1967: 193-209.

26. Landau LD, Lifshitz EM. Statistical Physics 3rd ed. Oxford; Pergamon Press, 1980); 471-472.

27. Echebarria B, Folch R, Karma A, Plapp M. Quantitative phase-field model of alloy solidification", Phys. Rev. E 2004; **70,** 061604-22.

28. Umantsev A. Identification of material parameters for continuum modeling of phase transformations in multicomponent systems. Phys. Rev. B, 2007; **75**, 024202-9.

29. Poston T, Stewart I. Catastrophe Theory and Its Applications. London; Pitman; 1978.

30. Landau LD. X-ray scattering of crystals in the neighborhood of the Curie point. Phys. Zs. Sowjet. 1937; **12**, 123-132; see also: Collected Papers of L.D. Landau, Ter-Haar D editor; London; Gordon and Breach, 1967: 233-242.

31. Ginzburg VL, Landau LD. On the theory of superconductivity. Sov. Phys. JETP 1951; **20**, 1064.

32. Cahn JW, Hilliard JE. Free energy of a nonuniform system. I. Interfacial energy. J. Chem. Phys. 1958; **28**, 258-267.

33. Gelfand IM, Fomin SV. Calculus of Variation.s New York; Prentice-Hall; 1963.

34. Gibbs JW. The Scientific Papers. Vol. 1, New York; Dover; 1961: 229-230.

35. Umantsev A. Continuum theory of interfacial segregation. Phys. Rev. B, 2001; **64**, 075419-10.

36. Umantsev A. "Thermodynamic stability of amorphous phases in pure substances", J. Stat. Phys. Submitted.

37. Ramakrishnan TV, Yussouff M. First-principles order-parameter theory of freezing. Phys. Rev. B 1979; **19**, 2775-2774.

38. Dmitriev VP, Rochal SB, Gufan YuM, Toledano P. Reconstructive transitions between ordered phases: the martensitic fcc-hcp and the graphite-diamond transitions. Phys. Rev. Lett. 1989; **62**, 2495-2498.

39. Toledano P, Dmitriev VP. Reconstructive Phase Transitions Singapore; World Scientific 1996: 292-299.

40. Lambrecht WRL, Lee CH, Segall B, Angus JC, Li Z, Sunkara M. Diamond nucleation by hydrogenation of the edges of graphite precursors. Nature 1993; **364** (6433) 607-610.

41. Stephan A, Meijer J, Weidenmüller U, Röcken H, Bukow HH, Burchard M, et al. The heavy ion micro-projection setup at Bochum. Nuclear Instruments and Methods in Physics Research Section B: Beam Interactions with Materials and Atoms 2001; **181**, Issues 1-4 (July), 39-43.

42. Zaitsev AM. High energy ion implantation into diamond and cubic boron nitride. Nuclear Instruments and Methods in Physics Research Section B: Beam Interactions with Materials and Atoms 1991; **62**, Issue 1 (November), 81-98.

43. Apte PA, Zeng XC. "Anisotropy of crystal-melt interfacial free energy of silicon by simulation", Appl. Phys. Lett. 2008; **92**, 221903-4

44. Jian Z, Kuribayashi K, Jie W, Chang F. Solid–liquid interface energy of silicon. Acta Materialia 2006; **54** 3227–3232.

45. Ravelo RJ, Baskes MI. Free energy calculations of the Cu-Sn interfaces. Mater. Res. Soc. Symp. Proc. 1996; **398**, 287–293.

46. Hoyt JJ, Asta M, Karma A. Atomistic and continuum modeling of dendritic solidification. Materials Science and Engineering 2003; **R41**, 121-163.

47. Stekolnikov AA, Furthmuller J, Beschtedt F. Absolute surface energies of group-IV semiconductors: Dependence on orientation and reconstruction**.** Phys. Rev. B 2002; **65** 115318-10.

48. Zallen R. The physics of Amorphous Solids. Weinheim, Germany, Wiley, 2004.

49. Cahn JW, Hilliard JE. Free energy of a nonuniform system. III. Nucleation in a two-component incompressible fluid. J. Chem. Phys. 1959; **31**, 688-699.

II.2 NUCLEATION IN THIN FILMS

II.2.1 Introduction

In order to better understand experimental results on growth of graphene films from carbonaceous atmospheres on sapphire substrates, theoretical and computational models to simulate this process have been developed. The problem of incipience of a new phase (*nucleation*) is central not only for physics of materials but also for many branches of science overall. Although the main reason for the nucleation—some kind of instability of the old phase—is the same in all of the situations, actual realization of it may be very different. In many cases nucleation occurs due to presence of foreign objects in the system or specific properties of the walls of a container that encompasses it. This type of nucleation sometimes is called "heterogeneous" and is not a subject of the present publication. We consider only those cases when the nucleation is a completely intrinsic phenomenon that comes about due to presence of thermal fluctuations in the system. Experimental verification of the nucleation theories encounters significant challenges because of many reasons, one of which is inconsistencies of the verification quantities, e.g. the nucleation rate versus transformation time. Notwithstanding, theoretical results allow researchers to glean valuable information regarding qualitative dependence of the experimental results on the control parameters, e.g. system's volume, driving force, and noise level.

Cluster models of nucleation, like the Classical Nucleation Theory (CNT), consider small aggregates of atoms or molecules (termed embryos or nuclei) as precursors of the new phase,

which constantly form and decompose in the old phase [1, 2]. On the other hand, field models of nucleation consider the system as a continuous medium whose properties are described by an effective Hamiltonian as a function of one or more continuous functions of space and time [3-7]. This type of models is the subject of the discussion in the present publication. Langer [3] introduced the field approach to the statistical theory of nucleation by describing the phase space of the system with an order parameter taken at a certain number of fixed space points. He obtained an equation for the probability current density in the phase space and found its stationary solution when the system is close to the phase-coexistence line. The nucleation rate in Langer's theory is estimated as the probability current at the saddle point of the Hamiltonian. Klein et al [4] extended the Langer's theory on the systems close to the spinodal point that is, the point of a barrierless transition. Buttiker and Landauer [5] applied the theory to a multi-saddle system. Patashinskii and Shumilo [6] developed a consistent field theory of decomposition of metastable states in conserved and non-conserved systems and calculated the lifetimes of the states as functions of the driving force. As a state variable they used radius of the nucleus, which is a well-defined quantity near the coexistence line but becomes ill-defined near the spinodal point. However, the functional dependencies of the lifetime on the control parameters in different theories are different. Tomita and Miyashita [7] conducted Monte Carlo simulations of the nucleation process in a metastable state of a two-dimensional Ising model. By examining the statistical properties of the ensemble of time-evolution paths of the state variable they analyzed dependence of the mean lifetime of the state on the system's size and driving force. They found that the dependence of the lifetime on the size itself depended on the magnitude of the driving force, being inversely proportional to the volume for small driving forces and independent of the size for the large ones. The crossover size depended on the driving force. The authors concluded that the change was due to a switchover in the relaxation mechanism and suggested "existence of a kind of dynamical potential of one degree of freedom" that describes the nucleation process.

An effective way to analyze the nucleation problem is to use the concept of *escape time* [8-10], which is loosely defined as the phase-transition time. This concept, however, avoids a multiple nuclei scenario, which may be important in some situations. Two methods are most often employed in order to compute the escape time in a continuous system: the Ising-model type and the analytical continuation type. In the framework of the first one the infinite-dimensional continuous system is broken into a large but finite set of cells and the spatially continuous function is replaced by the set of discrete variables [3, 11]. Then, the escape time is calculated for the multivariable finite system. In the second one, the real-valued partition function of the infinite-dimensional continuous system in the domain of parameters of the stable-phase is extended into the domain where the system is metastable or unstable and the partition function becomes complex. Then, the imaginary part of the latter is declared to be (proportional to) the rate of escape [3, 4, 11].

Much work has been done for the one-spatial dimension (1D) system. In a finite-size 1D system the barrier state undergoes a bifurcation at a particular size, which depends on the boundary conditions [19]. In $D \geq 2$, as known, there are many different barrier states of different 'heights'. In this publication we develop a method to calculate the escape rate in a two-space-dimensional (2D) continuum system, which is based on a single-variable Kramers-type problem. The recipes on how to reduce the infinite-dimensional spatially extended system to the single variable are provided in Sec. II. In Sec. III we analyze an important for applications two dimensional case and in Sec. IV we discuss all possible scenarios of nucleation in extended systems.

II.2.1.1 Ginzburg-Landau System

Many phase transformations in spatially extended systems have been successfully modeled by a set of ideas and equations known as the *Ginzburg-Landau* (GL) *system* [4, 6, 10-12]. In recent years the GL system turned into a paradigm that transcended traditional boundaries of scientific disciplines. In the GL system the thermodynamic states are represented by different distributions of an *order parameter* $\eta(\mathbf{x})$ (OP, scalar in the simplest case) and the free energy

$$G\{\eta\} = \int_V d^3x \left[g(\eta) + \frac{1}{2}\kappa(\nabla\eta)^2 \right] \qquad (1)$$

where V is the volume of the system, $g(\eta)$ represents the free energy density of a homogeneous system with multiple equilibrium states (*phases*), and the gradient term represents the free-energy contributions due to inhomogeneous distribution of the OP. The actual transformation from one state to the other proceeds through a process of nucleation that is, incipience of a nucleus or nuclei—small regions of the old phase (α) that have properties of the new phase (β). The process depends on the chemical potential difference:

$$[g] = g(\eta_\beta) - g(\eta_\alpha) \qquad (2)$$

which is often called the '*driving force*'. Usually it depends on the temperature of the system T; however, in addition to the temperature, it may depend on other factors, like pressure, concentration, external field (e.g. magnetic), etc. That is why we will keep the driving force as an independent control parameter of the system.

Equilibrium states of the system are extremals $\eta_E(\mathbf{x})$ of the functional Eq.(1) in the functional space $\{\eta\}$; they are described by the Euler-Lagrange equation:

$$\frac{\delta G}{\delta \eta} \equiv \frac{\partial g}{\partial \eta} - \kappa\nabla^2\eta = 0 \qquad (3)$$

The OP values in the old (α) and new (β) phases, η_α and η_β, are homogeneous solutions of Eq.(3); they are separated by another homogeneous equilibrium state—*transition state* η_t. As the first variation of G vanishes at $\eta=\eta_E(\mathbf{x})$ we have:

$$G\{\eta(\mathbf{x},t)\} = G\{\eta_B(\mathbf{x})\} + \delta^2 G\{\delta\eta\} + O(\delta\eta^3) \qquad (24)$$

As known [16], the second variation of the GL functional, Eq.(1), can be expressed as follows

$$\delta^2 G\{\delta\eta\} = \int_V d^3x\, \delta\eta \hat{H}(\eta)\delta\eta \qquad (24a)$$

where $\hat{H}$ is the GL Hamiltonian operator:

$$\hat{H}(\eta) \equiv \frac{\partial^2 g}{\partial \eta^2}\big(\eta(\mathbf{x})\big) - \kappa\nabla^2 \qquad (24b)$$

which has a complete set of eigenfunctions $\{\psi_i(\mathbf{x})\}$ [20]:

$$\hat{H}(\eta_E)\psi_i(\mathbf{x}) = \lambda_i\psi_i(\mathbf{x}) \qquad (24c)$$

The Schrodinger-type eigenfunction Eq.(24c) always has Goldstone modes—solutions for $\lambda_0=0$:

$$\boldsymbol{\psi}_0(\mathbf{x}) = \nabla\eta_E(\mathbf{x}) \qquad (24d)$$

For a non-convex free energy density function $g(\eta)$ there exists a localized solution the $\eta_B(\mathbf{x})$ with finite free energy excess

$$\Delta G_B \equiv G\{\eta_B(\mathbf{x})\} - G\{\eta_\alpha\} \tag{24e}$$

This solution is called the barrier state (*critical nucleus* or instanton) [22]. The spectrum of the barrier state Hamiltonian operator $\hat{H}(\eta_B)$ has a minimum:

$$\min_i \lambda_i \equiv \lambda_* \leq \lambda_0 = 0 \tag{25}$$

The eigenfunction ψ_* that corresponds to the minimum eigenvalue λ_* may be called the 'most dangerous mode'. Much is known about the one-spatial dimension (1D) system where for small driving forces the barrier states approach the kink-type solution [6, 11, 12, 17] and the spectrum of eigenvalues of $\hat{H}(\eta_{1D})$ is continuous in the positive domain and discrete with a minimum in the negative domain [18]. In a finite-size 1D system the barrier state undergoes a bifurcation at a particular size, which depends on the boundary conditions [19]. In D≥2, as known [12], a GL system has many different barrier states of different 'heights'. In a large isotropic system the critical nucleus and its 'most dangerous mode' (but not the Goldstone mode $\boldsymbol{\psi}_0$) are spherically symmetric that is, the OP distribution η_B and ψ_* depend on the distance from the *center* of the nucleus r only [20]. The eigenfunctions with $\lambda_i>0$ are the asymmetric, shape-distorting modes.

Internal (thermal) fluctuations play critical role in the transformation process by helping the system to form a nucleus or nuclei of the new phase, eventually driving the state variable 'over the barrier'. According to the Boltzmann's principle equilibrium probability density of a state $\eta(\mathbf{x})$ is

$$\mathcal{P} \sim e^{-\frac{G\{\eta\}}{k_B T}} \tag{5}$$

where k_B is the Boltzmann's constant. Evolution of the system with fluctuations may be described by a Fokker-Plank-type equation for the non-equilibrium probability density or the stochastic time-dependent Ginzburg-Landau equation (STDGLE):

$$\frac{d\eta}{dt} = -\gamma \frac{\delta G}{\delta \eta} + \xi(\mathbf{x}, t) \tag{4}$$

with the Langevin random force that obeys the conditions:

$$\langle \xi(\mathbf{x}, t) \rangle = 0; \ \langle \xi(\mathbf{x}, t) \xi(\mathbf{x}', t') \rangle = 2\gamma k_B T \delta(\mathbf{x} - \mathbf{x}') \delta(t - t') \tag{4b}$$

where γ is the GL relaxation coefficient.

According to the *Levanyuk-Ginsburg criterion* (LGC) for the GL method to be valid the scale of the OP fluctuations in a cube with the *correlation radius* r_C on the side must be smaller than the jump on both sides of the transition point: $[\eta] \equiv |\eta_\beta - \eta_\alpha|$. Taking into account that:

$$r_C = \sqrt{\frac{\kappa}{\frac{\partial^2 g}{\partial \eta^2}(\eta_\alpha)}} \tag{6}$$

the LGC may be written as follows:

$$\frac{(k_B T)^2}{\kappa^3} \left(\frac{\partial^2 g}{\partial \eta^2} (\eta_\alpha) \right) \ll [\eta]^4 \tag{7}$$

II.2.1.2 Escape Time

Many processes of different physical nature can be described as overdamped Brownian motion—random walk of a single stochastic variable subject to an external field of force and the irregular force of thermal fluctuations. Evolution of the stochastic variable v(t) from the initial value $v(0)=v_\alpha$ to the final value $v(\infty)=v_\beta>v_\alpha$ is described by the Langevin equation [8, 9]:

$$\frac{dv}{dt} = -\frac{\partial U}{\partial v} + \zeta(t),\ \langle \zeta(t)\zeta(t')\rangle = \Gamma\delta(t-t') \qquad (8)$$

with the zero-mean and delta-correlated Gaussian noise ζ(t) of the strength Γ. If the bistable potential U(v) has a maximum (*barrier*) in the domain $v_\alpha<v<v_\beta$, then Eq.(8) describes the Kramers-type process of overcoming the barrier [8, 9]. If the variable v represents different states of matter this process may be presented as a Brownian-motion replica of nucleation.

As the absolute value of the potential U does not matter, it may be normalized by defining $U(v_\alpha)=0$. If the height of the energy barrier located at $v= v_B$ is greater than the energy of the thermal fluctuations,

$$U(v_B) > \frac{\Gamma}{2} \qquad (9)$$

then the process may be characterized by the *escape time*—the time needed for a system, which was initially in the vicinity of a minimum at $v(0)=v_\alpha$ with higher value of the potential, to reach for the first time a vicinity of the minimum at $v= v_\beta$ with lower value of the potential [13]. If the inequality, Eq.(9), is not true the system is said to be in the fluctuation regime [8, 9]. The escape time can be expressed as follows [9]:

$$\tau_v = 2\sqrt{\frac{\pi}{\Gamma|U''(v_B)|}}\, e^{\frac{U(v_B)}{\Gamma/2}} \int_{-\infty}^{v_B} e^{-\frac{U(v)}{\Gamma/2}} dv \qquad (10)$$

In Eq.(10) the exponential (the Arrhenius factor)is inversely proportional to the probability of the barrier state, U'' is the second derivative of the potential and the square-root represents the Zeldovich factor, which expresses the probability for the variable v to return back from the region beyond the barrier. The integral in Eq.(10) is proportional to the splitting probability—probability for the variable v to be found left of the barrier, that is with $v<v_B$. Due to condition (9) this integral can be estimated using the Laplace method [14]. Depending on the analytical properties of the potential U(v) at the point of minimum v_α, the integral takes on different values. If (Figure 1a)

$$U(v) = U'(v_\alpha)v + O(v^2)\ \ for\ \ v \geq 0, \qquad (11a)$$

then

$$\int_{-\infty}^{v_B} e^{-\frac{U(v)}{\Gamma/2}} dv \approx \int_0^{+\infty} e^{-\frac{2U'(v_\alpha)}{\Gamma}v} dv = \frac{\Gamma}{2U'(v_\alpha)} \qquad (11b)$$

while if (Figure 1b)

$$U(v) = \frac{1}{2}U''(v_\alpha)v^2 + O(v^3), \qquad (12a)$$

then

$$\int_{-\infty}^{v_B} e^{-\frac{U(v)}{\Gamma/2}} dv \approx \int_{-\infty}^{+\infty} e^{-\frac{U''(v_\alpha)}{\Gamma} v^2} dv = \sqrt{\frac{\pi\Gamma}{U''(v_\alpha)}} . \qquad (12b)$$

Notice that the difference in 'smoothness' of the potential U(v) at the point of minimum v_α, Eq.(11a) or Eq.(12a), entails different dependences of the prefactor in Eq.(10) on the noise strength Γ.

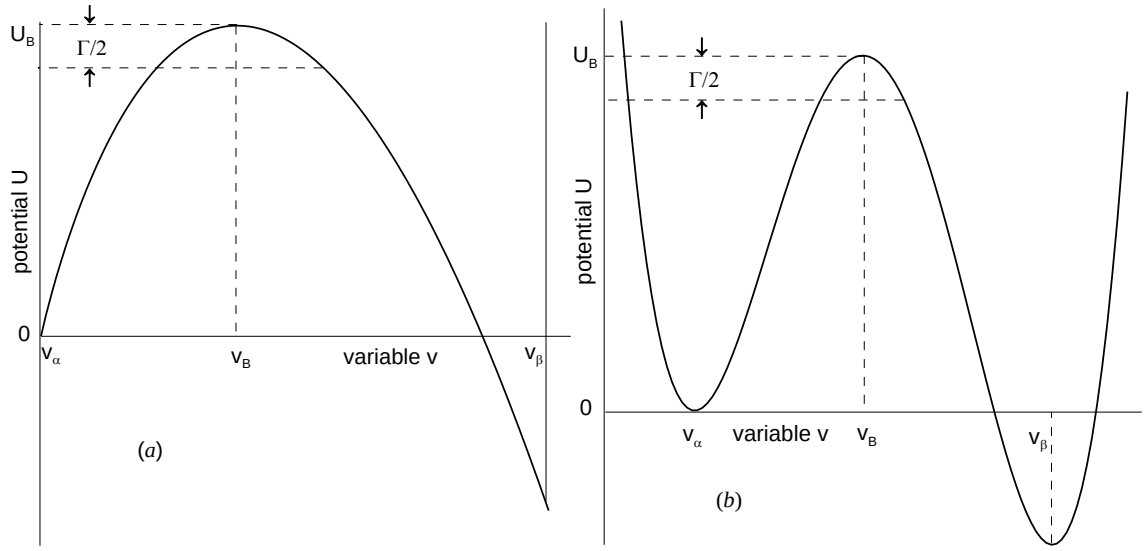

Fig. 2.1. Bistable potentials U(v) with different analytical properties at the point of minimum v_α: (a)—non-smooth, Eq.(11a); (b)— smooth, Eq.(12a).

II.2.2 Most Probable Path

We are considering a transformation in a system that favors the β phase but starts off in an almost homogeneous state close to the α phase. The transformation, of course, may take a path that consists of the states all of which are almost homogeneous. However, in large systems (not necessarily thermodynamic limit of V→∞) the 'homogeneous path' takes very long time because the exponent in Eq.(10) is proportional to V (small-size systems will be discussed in Sec.III). Hence, the system will be 'looking' for another, heterogeneous path. In the present study we are assuming that between the equilibrium states evolution of the OP in the functional space {η} proceeds along *the most probable path* (MPP) consisting of the states such that all nearby states with the same v have smaller probability measured by the Boltzmann's formula, Eq.(5). Thus, MPP is an evolutionary path in a phase space of the system that matches the one-dimensional trajectory of the state variable v(t). Then, in order to use solution, Eqs.(10; 11 or 12), for the GL system we need to bridge the gap between the infinite-dimensional continuum function η(**x**, t) and the one-dimensional quantity v(t), which obeys the stochastic, Langevin Eq.(8).

To convert the infinite-dimensional continuum function η(**x**, t) into the one-dimensional quantity v(t) we will be using the functional

$$v(t) \equiv \int_V d^3x \, [\eta(\mathbf{x}, t) - \eta_\alpha] \qquad (13)$$

which may be called the *volumetric content*. In terms of this quantity the phase transformation is a process of change of v(t) from v_α=0 to v_β=[η]V. Differentiating Eq.(13) with respect to time and using Eqs.(3, 4) we reduce the STDGLE (4) to a Langevin Eq.(8):

$$\frac{dv}{dt} = -\gamma F + \zeta_v(t) \tag{14}$$

where the random force of fluctuations

$$\zeta_v(t) \equiv \int_V d^3x\, \xi(\mathbf{x}, t) \tag{15}$$

has zero mean and the following correlation property:

$$\langle \zeta_v(t)\zeta_v(t')\rangle = \Gamma_v \delta(t-t'), \quad \Gamma_v = 2\gamma k_B T V \tag{15a}$$

The thermodynamic force

$$F \equiv \int_V d^3x\, \frac{\delta G}{\delta \eta}\{\eta(\mathbf{x}, t)\} \tag{16}$$

makes the quantity v increase or decrease depending on the state of the system $\eta(\mathbf{x}, t)$. At the equilibrium states $\eta_E(\mathbf{x})$, including the homogeneous phases η_α and η_β and the transition state η_t, the force F vanishes, see Eqs.(3, 16). Using the Gauss theorem and the Newmann-type boundary condition ($\mathbf{n}\nabla\eta=0$) on the boundary of V one can see that the gradient-energy contribution to the thermodynamic force, Eq.(16), vanishes. If the OP of the system deviates only slightly from its value in the α-phase ($|\eta-\eta_\alpha| \ll [\eta]$), then $\partial g/\partial\eta \approx \partial^2 g/\partial\eta^2(\eta_\alpha)(\eta-\eta_\alpha)$ and the force F is a linear function of the content v:

$$F = \frac{\partial^2 g}{\partial \eta^2}(\eta_\alpha)v + O(v^2) \tag{17}$$

If the OP deviation is not small, the thermodynamic force may not be a function of v in the sense that for the same value of v different values of F are possible.

However, on the MPP this is not the case. Indeed, variation of the content v between two nearby states when at least one of them, $\eta_v(\mathbf{x}, t)$, is on MPP is

$$dv = \int_V d^3x\, \delta\eta\,, \qquad \delta\eta \equiv \eta(\mathbf{x}, t) - \eta_v(\mathbf{x}, t) \tag{18}$$

If both states are on the MPP then $dv\neq 0$; if only one, then we can find a hypersurface $\{\eta_0\}$ on which dv=0. On this hypersurface

$$\delta G\{\eta_v, \eta_0\} \equiv G\{\eta_0\} - G\{\eta_v\} = \int_V d^3x\, \frac{\delta G}{\delta \eta}\{\eta_v\}\delta\eta_0$$

If $F\{\eta_v\}>0$ then $\delta G\{\eta_v, \eta_0\}>0$. Hence (see Eq.(5)), no state on the hypersurface other than η_v belongs to the MPP. Thus, on the MPP the thermodynamic force *is* a function of the content v: F=F(v). Notice that $\delta F\{\eta_v\}$ is not sign definite on the hypersurface.

Introducing on the MPP the potential U as

$$U(v) \equiv \gamma \int_0^v F(v')dv' \tag{19}$$

and using Eq.(17) we find that

$$U'(v_\alpha) = 0; \;\; U''(v_\alpha) = \gamma \frac{\partial^2 g}{\partial \eta^2}(\eta_\alpha) > 0 \tag{20}$$

The strong inequality in Eq.(20) comes from the assumption that the phase α is not at the spinodal point. Applying Eqs.(3, 16, 19) to the MPP we see that the U-potential has a barrier at $v=v_B$ with:

$$U(v_B) > 0; \quad U'(v_B) = \gamma F(v_B) = 0 \tag{21}$$

Hence, it represents a saddle-type extremal $\eta_B=\eta_E(\mathbf{x})$ of the functional, Eq.(1)—the barrier state of the GL system. Furthermore,

$$U(v) = \gamma \int_V d^3x \int_{\eta_\alpha}^{\eta_v} \delta\eta \int_V d^3x' \frac{\delta G}{\delta \eta}\{\eta(\mathbf{x}', t)\}$$
$$= \gamma V[G\{\eta_v(\mathbf{x}, t)\} - G\{\eta_\alpha\}] \tag{22}$$

where the middle integration is functional and v and $\eta_v(\mathbf{x},t)$ are related by Eq.(13). Then

$$U(v_B) = \gamma V \Delta G_B \tag{23}$$

where ΔG_B is the free energy excess associated with the barrier state.

Variations $\delta\eta(\mathbf{x}, t)$ can be expanded in $\{\psi_i(\mathbf{x})\}$, see Eq.(24c). Now we can specify the MPP in the vicinity of $\eta_B(\mathbf{x})$ as the variations of $\eta_v(\mathbf{x}, t)$ in the directions of the most dangerous and Goldstone modes:

$$\delta\eta_v(\mathbf{x}, t) \equiv \eta_v - \eta_B = \alpha_*(t)\psi_*(\mathbf{x}) + \boldsymbol{\alpha_0}(t)\boldsymbol{\psi_0}(\mathbf{x}) \tag{26}$$

The most dangerous mode is responsible for the magnitude of the variation $\delta\eta$, the Goldstone mode—for the emergence of the barrier state at different points in the space. The shape distorting modes $\psi_i(\mathbf{x})$ with $\lambda_i>0$ are not a part of the MPP. Then, using Eqs.(13, 24d) we obtain that on the MPP

$$v = v_B + \alpha_* \int_V d^3x\, \psi_*(\mathbf{x}), \tag{27}$$

because the barrier state is an instanton:

$$\int_V d^3x\, \nabla\eta_B(\mathbf{x}) = 0$$

Using Eqs.(24a, 26) we obtain that on the MPP

$$\delta^2 G = \alpha_*^2 \lambda_* \int_V d^3x\, \psi_*^2(\mathbf{x}),$$

because in the direction of the Goldstone modes the free energy does not change ($\lambda_0=0$). Then using Eqs.(22-24) we obtain that on the MPP

$$U(v) = U(v_B) + \alpha_*^2 \lambda_* \gamma V \int_V d^3x\, \psi_*^2(\mathbf{x}) \tag{28}$$

Now we can estimate the second derivative of the potential U at the barrier state. Indeed, using the rule of differentiation of implicit functions for Eqs.(27, 28), we obtain:

$$U''(v_B) = 2\gamma\lambda_* V \frac{\int_V d^3x\, \psi_*^2(\mathbf{x})}{\left(\int_V d^3x\, \psi_*(\mathbf{x})\right)^2} \tag{29}$$

Compare Eq.(29) with Eq.(20) and notice that in the thermodynamic limit ($V\to\infty$) $U''(v_B)$ scales with the volume of the system V while $U''(v_\alpha)$ is independent of it. Substituting Eqs.(29, 20) into Eq.(10) we arrive at the following expression for the escape time in the stochastic GL system:

$$\tau_v = \frac{\sqrt{2}\pi \int_V d^3x\, \psi_*(\mathbf{x})}{\gamma\sqrt{V g''(\eta_\alpha)|\lambda_*| \int_V d^3x\, \psi_*^2(\mathbf{x})}}\, e^{\frac{\Delta G_B}{k_B T}} \tag{30}$$

In small systems (V→0) the escape time is independent of the volume because $\int_V \sim V$. In the thermodynamic limit (V→∞) when

$$v_B \ll (\eta_\beta - \eta_\alpha)V \tag{53}$$

the escape time is inversely proportional to the square-root of the volume, not the volume itself, because $\int_V \to$const.

II.2.2.1 Tangential Potential

To elucidate the dependence of the escape time on the driving force [g] let us consider a system which is described by the *tangential potential*:

$$g(\eta,[g]) = g_\alpha + \frac{1}{2}a\,\omega^2(\eta) + [g]\,\nu(\eta); \tag{31}$$

$$\omega(\eta) = \eta(1-\eta);\;\; \nu(\eta) = \eta^2(3-2\eta) \tag{31a}$$

where $g_\alpha = g(\eta_\alpha, [g])$ and $a>0$ may depend on temperature and other external parameters. A useful property of the tangential potential is

$$\frac{\partial g}{\partial \eta}(\eta,[g]) = \frac{\partial g}{\partial \eta}(\eta,0) + 6[g]\sqrt{\frac{2}{a}\{g(\eta,0) - g_\alpha\}} \tag{31b}$$

The phases $\eta_\alpha=0$ and $\eta_\beta=1$ are separated by the transition state

$$\eta_t = \frac{1}{2}\left(1 + 6\frac{[g]}{a}\right), \tag{32a}$$

and

$$g''(\eta_\alpha,[g]) = 2a\eta_t \tag{32b}$$

The α and β phases are at equilibrium for [g]=0; at [g]=$-a/6$ the α-phase reaches its spinodal point.

Using the internal time, length, and temperature scales of the tangential potential:

$$\tau = \frac{1}{\gamma a},\;\; l = \sqrt{\frac{\kappa}{a}},\;\; T_F = \frac{al^3}{k_B}, \tag{33a}$$

the system's volume, fluctuations, and driving force are scaled as follows:

$$\Omega = \frac{V}{l^3},\;\; \vartheta = \frac{T}{T_F},\;\; \Delta = \frac{|[g]|}{a/6} \tag{33b}$$

For the tangential potential the correlation length diverges near the spinodal point:

$$r_C = \frac{l}{\sqrt{1-\Delta}} \tag{34a}$$

and the LGC, Eq.(7), takes the form:

$$1 - \Delta \ll \frac{1}{\vartheta^2} \tag{34b}$$

On the 'homogeneous path' of the system described by the tangential-potential the escape time, Eq.(10), can be calculated by noticing that in this case v=η and U(v)=γg(η). Then

$$\tau_h = \frac{2\sqrt{2}\pi}{\gamma a(1+6[g]/a)\sqrt{1-6[g]/a}} e^{\frac{Va}{32k_BT}(1+6[g]/a)^3(1-2[g]/a)} = \tau \frac{2\sqrt{2}\pi}{(1-\Delta)\sqrt{1+\Delta}} e^{\frac{\Omega}{32\vartheta}(1-\Delta)^3(1+\frac{1}{3}\Delta)} \quad (35)$$

According to the criteria (9, 34) Eq.(35) is valid if the driving force is in the following range:

$$2\left(\frac{3\vartheta}{\Omega}\right)^{1/3} < 1-\Delta \ll \frac{1}{\vartheta^2} \quad (36)$$

Furthermore, the 1D kink-type equilibrium state obeys the following equation

$$\kappa\left(\frac{d\eta_{1D}}{dx}\right)^2 = a\,\omega^2(\eta_{1D}). \quad (37)$$

It has a hyperbolic-tangent solution (with two branches: + and –), which describes an interface between the α and β phases. For the system described by the tangential potential, Eqs.(31), Eqs.(3, 24c) take the form:

$$\kappa\left(\frac{d^2}{dr^2}+\frac{2}{r}\frac{d}{dr}\right)\eta_B + 2a\eta_B(\eta_B-\eta_t)(1-\eta_B) = 0 \quad (38a)$$

$$\kappa\left(\frac{d^2}{dr^2}+\frac{2}{r}\frac{d}{dr}\right)\psi_* + \{\lambda_* - a[2\eta_t - 4(1+\eta_t)\eta_B + 6\eta_B^2]\}\psi_* = 0 \quad (38b)$$

They are supplemented by the boundary conditions:

$$\frac{df}{dr} = 0 \;\; at\, r = 0 \quad (39a)$$

and

$$f \to 0, \;\; \frac{df}{dr} \to 0 \;\; for \;\; r \to \infty \quad (39b)$$

that apply to both functions:

$$f = \eta_B(r); \;\; \psi_*(r) \quad (39c)$$

The function $\psi_*(r)$ needs to be normalized because it obeys a linear equation. The escape time, however, is independent of the normalization condition, see Eq.(30). Below for the purposes of numerical calculations the following normalization condition will be used:

$$\psi_*(0) = 1 \quad (39d)$$

Applying formula $\nabla(\eta\nabla\eta)=\eta\nabla^2\eta+(\nabla\eta)^2$ and the Gaussian theorem to Eqs.(1, 23) and using the equilibrium equation, Eq.(3), together with the boundary condition, Eq.(39b) we express the free energy excess of the barrier state as follows:

$$\Delta G_B = 4\pi\int_0^\infty \left\{\frac{1}{2}\kappa\left(\frac{d\eta_B}{dr}\right)^2 + g(\eta_B) - g_\alpha\right\} r^2\, dr = \frac{4\pi}{3}a\left[(1+\eta_t)I_3(\eta_B) - \frac{3}{2}I_4(\eta_B)\right] \quad (40)$$

where the moments are defined as:

$$I_n(f) \equiv \int_0^\infty f^n(r)\, r^2\, dr \tag{40a}$$

Eqs.(38, 39) can be solved numerically and the escape time, Eq.(30), can be calculated as a function of the volume, fluctuations, and driving force (see Sec. II.3). However, the limiting cases of small and large driving force can be studied analytically.

II.2.2.2 Small Driving Force

Compare Eq.(38a) with the 1D version of Eq.(3) using the property Eq.(31b) and notice that if $|[g]|\to 0$ then everywhere except for a small vicinity of the center: $\eta_B(r)\approx\eta_{1D}(r\text{-const})$ [6]. Specifically, for

$$\Delta \ll 1 \tag{41}$$

using the following scaling of independent and dependent variables:

$$r = l\tilde{r};\ \eta_B(r) = \tilde{\eta}_B(\tilde{r});\ g(\eta) = a\tilde{g}(\tilde{\eta}); \tag{41a}$$

we find that the following solution applies:

$$\eta_B(r) \cong \eta_{1D}(r - R_B), \quad r > r_0 \sim o(1); \tag{42}$$

if

$$R_B = \frac{2}{\Delta}; \tag{42a}$$

Here and below the tildes are dropped. The solution around the center is as follows

$$\eta_B(r) \cong \eta_B(0) + \frac{1}{6}\frac{\partial g}{\partial \eta}(\eta_B(0), \Delta) r^2, \quad 0 < r < r_0; \tag{43}$$

Matching the solutions, Eqs.(42) and Eqs.(43), we obtain:

$$\eta_B(0) \cong \eta_{1D}(-R_B) = 1 - \eta_{1D}(R_B) \sim 1 - e^{-R_B} \tag{44}$$

Apply Eq.(31) to Eq.(43) and notice that in the limit $\Delta\to 0$ the coefficient in front of r^2 is also exponentially small.

Next, differentiating Eq.(38a) with respect to r and comparing it to Eq.(38b) one can see that

$$\psi(r) \cong -\frac{d\eta_B}{dr}(r) \cong -\frac{d\eta_{1d}}{dr}(r - R_B), \quad r > r_0; \tag{45}$$

if

$$\lambda = \frac{2}{R_B^2} = \frac{\Delta^2}{2}; \tag{46}$$

while

$$\psi(r) \cong 1 + \frac{1}{6}\left\{\frac{\partial^2 g}{\partial \eta^2}(\eta_B(0), \Delta) + \frac{2}{R_B^2}\right\} r^2, \quad 0 < r < r_0; \tag{47}$$

Here we used the normalization condition Eq.(39d) and the scaling (tildes were dropped):

$$\lambda_* = -a\tilde{\lambda}; \psi_*(r) = \tilde{\psi}(\tilde{r}); \tag{41b}$$

Now we can find the exponent and the prefactor of the escape time, Eq.(30). To calculate the free energy barrier we divide the domain $0<r<\infty$ into four subdomains: (a)-$0<r<r_0$, (b)-$r_0<r<R_B-r_0$, (c)- $R_B-r_0<r<R_B+r_0$, (d)-$R_B+r_0<r<\infty$. Contributions of the domains (a) and (d) are negligible—the first one because of the small size of the domain, the second one because of the vanishing value of $\eta_B(r)$ in that domain. Then the total free energy barrier may be written as follows

$$\Delta \mathcal{G}_B = \frac{4\pi}{3}\left[(1+\eta_t)\eta_B^3(0) - \frac{3}{2}\eta_B^4(0)\right]\int_0^{R_B} r^2\, dr + 4\pi R_B^2 \int_{-\infty}^{+\infty}\left(\frac{d\eta_B}{dr}\right)^2\, dr \tag{48}$$

where the first integral is the contribution of the domain (b), the second—(c), the integration limits in (c) were spread to $\pm\infty$ due to Eq.(42), and the following scaling was used:

$$I_n = l^3\tilde{I}_n;\quad \Delta\mathcal{G}_B = al^3\widetilde{\Delta\mathcal{G}}_B \tag{41c}$$

The interfacial energy for the tangential potential is

$$\sigma \equiv \int_{-\infty}^{+\infty}\kappa\left(\frac{d\eta_{1D}}{dx}\right)^2 dx = \frac{\sqrt{a\kappa}}{6}. \tag{49}$$

Using properties of the 1D kink-type solution, Eq.(37), and Eq.(43) we obtain

$$\Delta\mathcal{G}_B = \frac{2\pi R_B^2}{9} = \frac{8\pi}{9\Delta^2} \tag{50}$$

In order to calculate the prefactor we, using Eqs.(37, 45) obtain:

$$\int_V d^3x\,\psi(\mathbf{x}) = 4\pi\int_0^{\infty}\psi(r)\,r^2\,dr \approx 4\pi R_B^2\eta_B(0) \approx 4\pi R_B^2 \tag{51a}$$

$$\int_V d^3x\,\psi^2(\mathbf{x}) = 4\pi\int_0^{\infty}\psi^2(r)\,r^2\,dr \approx 4\pi R_B^2\left(\frac{\eta_B^2(0)}{2} - \frac{\eta_B^3(0)}{3}\right) \approx \frac{2}{3}\pi R_B^2 \tag{51b}$$

Then, for the escape time in the small-driving-force regime we obtain:

$$\tau_v^s = \tau\frac{2\sqrt{6}\,\pi^{3/2}R_B^2}{\sqrt{\Omega(1-\Delta)}}e^{\frac{2\pi R_B^2}{9\vartheta}} = \tau\frac{8\sqrt{6}\,\pi^{3/2}}{\Delta^2\sqrt{\Omega(1-\Delta)}}e^{\frac{8\pi}{9\vartheta\Delta^2}} \tag{52}$$

The unbounded growth of the escape time in the limit of vanishing driving force ($\Delta\to 0$) needs to be investigated further. As we pointed out above (see Eq.(9) and the comments after) the barrier must be high enough for the concept of the escape time to be valid.

Combining all conditions together we arrive at a double inequality on the driving force:

$$2\left(\frac{4\pi}{3\Omega}\right)^{1/3} \ll \Delta < \min\left(\frac{3}{16}, \frac{2}{3}\sqrt{\frac{2\pi}{\vartheta}}\right) \tag{54}$$

which shows that in small or noisy systems the small-driving-force approximation does not apply.

II.2.2.3 Large Driving Force

In the large-driving-force (so-called scaling or Cahn-Hilliard) regime of nucleation where $|[g]| \to a/6$ or

$$\Delta \to 1^- \tag{55}$$

an analytic expression for the escape time as a function of the scaled volume, fluctuations, and driving force can be obtained if the variables in Eqs.(41) are rescaled further as follows:

$$r = \frac{\tilde{r}}{\sqrt{\eta_t}};\ \eta_B(r) = \eta_t\, Y(\tilde{r});\ \ \psi(r) = \tilde{\psi}(\tilde{r});\ \ \lambda = \eta_t\, \Lambda;\ I_n(\eta_B) = \eta_t^{n-3/2} \tilde{I}_n(Y);\ \ I_n(\psi) = \eta_t^{-3/2} \tilde{I}_n(\tilde{\psi}) \tag{56}$$

Indeed, noticing that in this regime $\eta_t \ll 1$ (see Eqs.(32a, 33b)) and $\eta_B \ll 1$ we obtain from Eqs.(38) the following equations

$$\left(\frac{d^2}{dr^2} + \frac{2}{r}\frac{d}{dr}\right) Y + 2Y(Y-1) = 0 \tag{57a}$$

$$\left(\frac{d^2}{dr^2} + \frac{2}{r}\frac{d}{dr}\right) \psi + [4Y - \Lambda - 2]\psi = 0 \tag{57b}$$

with the boundary conditions that follow from Eqs.(39). The tildes in Eqs.(57) were dropped. Then Eq.(30) for the escape time takes the form:

$$\tau_v^l = \tau \frac{2\pi^{3/2} I_1(\Psi)}{\eta_t^{7/4}\sqrt{\Omega \Lambda I_2(\Psi)}} e^{\frac{4\pi I_3(Y)}{3}\frac{\eta_t^{3/2}}{\vartheta}} \tag{58}$$

Divergence of the prefactor in Eq.(58) as $\eta_t \to 0$ ($\Delta \to 1$) is a result of two effects. First, the Zeldovitch factor increases because of the decreasing barrier sharpness (flattening of the potential barrier $U(v_B)$). Second, the splitting-probability integral in Eq.(12b) increases because of the flattening of the 'metastable valley' $U(v_\alpha)$. Both effects render recrossings much easier. Combining the conditions of high potential barrier, Eq.(9), large driving force, Eq.(55), LGC, Eq.(34), and small volume of the nucleus, Eq.(53) into one double inequality we obtain:

$$\left(\frac{3\vartheta}{\sqrt{2}\pi I_3(Y)}\right)^{2/3} < 1 - \Delta \ll \min\left(1, \frac{1}{\vartheta^2}, \frac{\Omega}{2\pi I_1(Y)}\right) \tag{59}$$

This condition shows that near the α-phase spinodal point ($\Delta=1$) there is the fluctuation zone where Eq.(58) is not applicable.

II.2.3 Numerical Calculations

Numerical solutions of the equilibrium equations with the boundary conditions, Eqs.(38, 39), scaled as in Eqs.(41) were obtained using the shooting method. Specifically, for given Δ, first, the value of $\eta_B(0)$ was set equal to $(1+\eta_c)/2$ where $g(\eta_c, \Delta)=g_\alpha$ and $0<\eta_c<1$. Second, $\eta_B(r_0)$ was calculated using Eq.(41) for $r_0=0.005$. Third, using this value as the initial condition, Eq.(38a) was integrated in the domain $r_0<r<10$ using Runge-Kutta method with adaptive step-size control. Fourth, $\eta_B(10)$ was verified against the boundary conditions, Eq.(39b), the value of $\eta_B(0)$ was adjusted accordingly, and the calculations were repeated from step two. The iterations of $\eta_B(0)$ were repeated twenty times. Fifth, the integration

domain boundary was increased from 10 to 11 and, provided the change was not significant, the trajectory $\eta_B(r)$ was recorded. After that, integration of Eq.(38b) with a trial eigenvalue $\lambda=5$ was conducted in the domain $r_0<r<11$ using the Runge-Kutta method and Eq.(43) as the initial condition $\psi(r_0)$. Iterations of λ were conducted until the maximum value that satisfies the boundary conditions, Eqs.(39b), was achieved. Using the previously recorded trajectory $\eta_B(r)$ and eigenfunction $\psi(r)$ the moments, Eqs.(40a), were calculated. Same procedure was used to solve the scaled Eqs.(57) for the large-driving-force regime. Results of the numerical calculations are presented in Figures 2 and 3. In Fig. 2 notice the significant difference between the shapes of the eigenfunctions at different values of the driving force Δ. In Fig. 3 notice that the general case of Eq.(38) matches the limiting cases of small and large driving forces in the eigenvalue, prefactor, and exponent; however, the resolution of the numerical method was too coarse to allow for the match to be smooth.

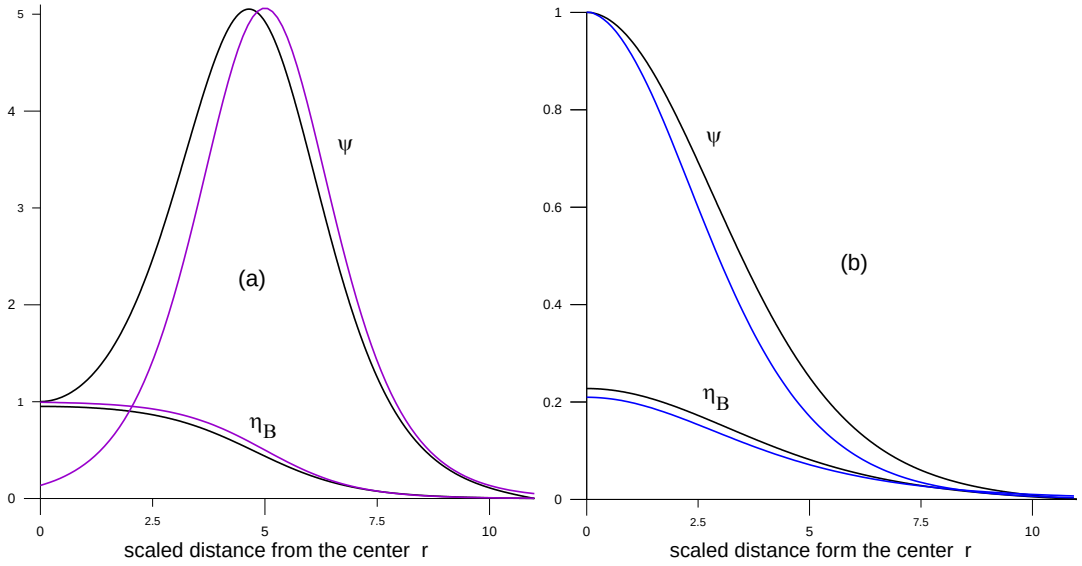

Fig. 2.2. Numerically calculated critical nucleus $\eta_B(r)$ and the most dangerous eigenfunction $\psi(r)$ for (a)— large ($\Delta=0.9$) and (b)—small ($\Delta=0.4$) driving forces. Black lines correspond to the solutions of Eqs.(38), blue lines—Eqs.(57), purple lines—analytical solutions, Eqs.(42, 45), with R_B, Eq.(42a).

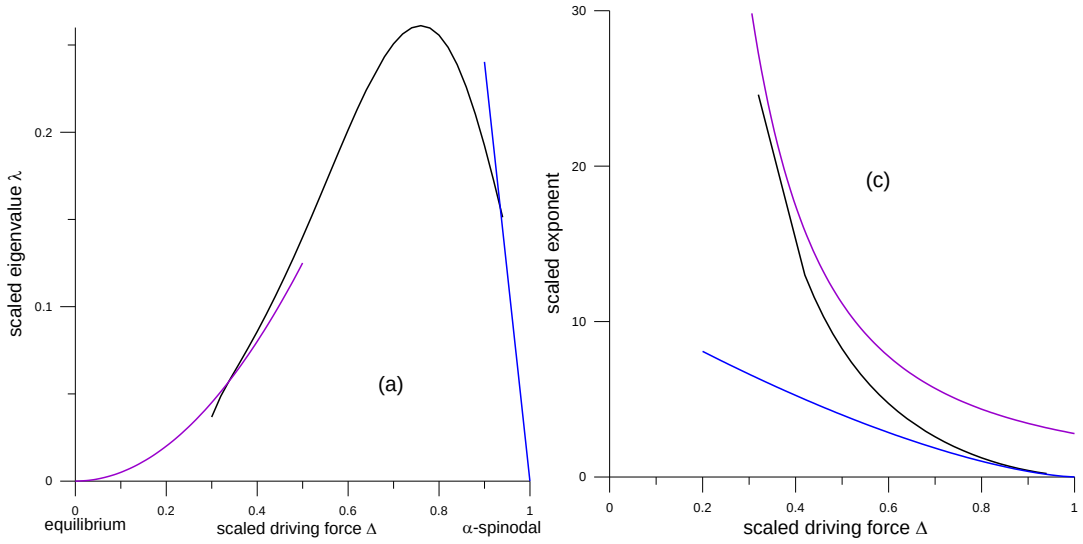

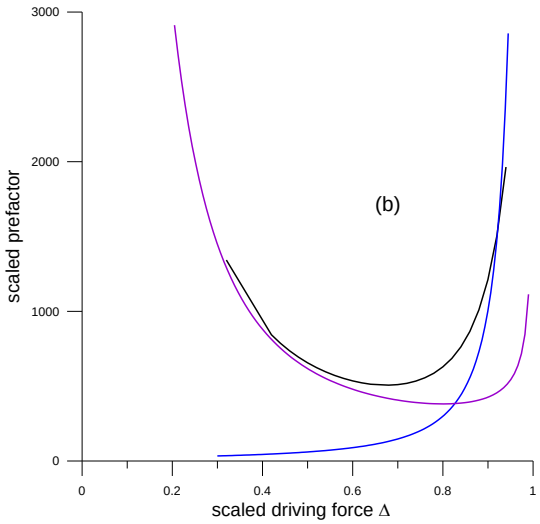

Fig. 2.3. Scaled eigenvalue λ of the most dangerous eigenfunction—(a), prefactor—(b), and exponent—(c) of the escape time versus scaled driving force Δ in the system with ϑ=1 and Ω=1. Black lines correspond to the general case, Eq.(30), blue—large-driving-force, Eq.(58), purple—small-driving-force, Eq.(52) cases.

II.2.4 Discussion of the Nucleation Path

In this Section we will compare main results of this publication with similar results available in the literature by comparing their *nucleation rates* defined as

$$k_v = \frac{1}{\tau_v}, \tag{60}$$

and discuss how they can be used to identify a proper nucleation path in the system. All expressions of the nucleation rate, including CNT, contain the Arrhenius factor—exponential of the ratio of the free energy excess due to the barrier state ΔG_B to the noise intensity k_BT [3, 6, 11, 4, 19]. The prefactors of all the expressions are different. The difference in the dependence on the driving force may be attributed to the difference in the free energy potentials used. Noticeable, however, is the difference in the dependence of the prefactors on the volume of the system with the nucleation rate due to Eq.(30) being proportional to the square-root of the volume as opposed to the traditional linear proportionality. To understand the source of the discrepancy let us analyze contributions of different modes into the nucleation rate. The shape-distorting modes do not contribute because they attenuate very fast [6]. To estimate the contribution of the Goldstone mode we will calculate the escape time without this contribution and compare the results. In Appendix we consider the small-driving-force regime without taking the Goldstone mode into account. Comparing Eqs.(52, A13) we notice that the prefactors of both expressions depend differently on the volume Ω, noise level ϑ, and driving force Δ. This means that the translational freedom of the nucleus makes its nucleation rate more volume dependent. The square-root dependence of the escape times on the volume of the system may be explained by the large correlation length $\sim l/\sqrt{1-\Delta}$, see Eq.(34a), which approaches the size of the system as the driving force increases. In their Monte Carlo simulations of the nucleation process in a two-dimensional Ising model Tomita and Miyashita [7] obtained variable dependence of the lifetime on the volume of the system depending on the magnitude of the driving force.

Different regimes of nucleation considered in this paper may be looked at as interplay of different length scales. For many transformations, e.g. crystallization, the driving force may be expressed as a linear function of temperature:

$$[g] = -L\delta,\ \ \delta \equiv \frac{T_E - T}{T_E} \qquad (61)$$

where L is the latent heat of the transformation, T_E is the equilibrium temperature, and δ--*supercooling*. In this case the scaled driving force and noise level become linearly dependent:

$$\Delta = \frac{\delta}{E},\ \ \vartheta = \vartheta_E(1-\delta),\ \ E = \frac{L}{a},\ \ \vartheta_E = \frac{T_E}{T_F} \qquad (62)$$

In the Table are shown the typical values of the numbers E and ϑ_E for metals and carbon. Then, in addition to the correlation length, Eq.(34a), critical nucleus radius, Eq.(42a), and system's size $\Omega^{1/3}$ we find two more length scales, the capillary length l_C and the fluctuation length l_F:

$$l_C \equiv \frac{\sigma}{L} = \frac{l}{6E}, \qquad l_F \equiv \sqrt{\frac{k_B T_E}{\sigma}} = l\sqrt{6\vartheta_E} \qquad (63)$$

For instance, condition Eq.(9) means that $R_B \gg l_F$.

To assess feasibility of different paths we will be comparing their nucleation rates declaring a winner the path with the greatest rate. A nucleating system may choose among several options: (a)—form a single nucleus: 3D, 2D, or 1D, (b)—form multiple nuclei, or (c)—transform more or less homogeneously. Let us first compare the 3D path with the homogeneous one in the systems of different sizes and noise levels and under different driving forces. The large-driving-force homogeneous/3D crossover value, which can be found by equating Eqs.(35, 58):

$$\Delta_{h/v} \cong 1 - 2^{7/3}\left(\frac{\pi}{\Omega}A\right)^{2/3}, \qquad \frac{I_1^2(\Psi)}{\Lambda\, I_2(\Psi)} < A < I_3(\mathrm{Y}) \qquad (64)$$

is in the fluctuation zone for large systems and, most likely, does not present physical interest. More interesting is the medium-driving-force homogeneous/3D crossover. In Figure 2.4 are plotted the escape rates as functions of the supercooling for the 3D and homogeneous paths of nucleation in the system with E=0.5 and ϑ_E=0.6 and different values of Ω. Notice that if the volume is small enough, the nucleation path depends on the supercooling.

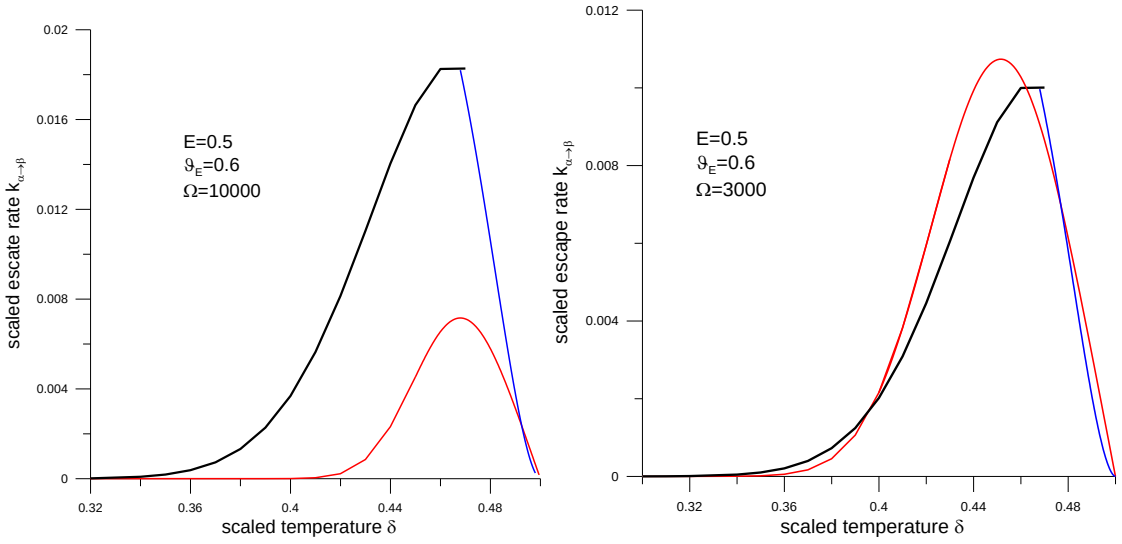

Fig. 2.4. Escape rates as functions of the supercooling in systems with E=0.5, ϑ_E=0.6, and different values of Ω: (a)— Ω=10000, (b)— Ω=3000. Black—3D general path, Eq.(30), blue—3D large-driving-force path, Eq.(58), red—homogeneous path, Eq.(35).

Instead of a single nucleus path the system may choose the multi-nucleus scenario in which the escape rate 'competes' with the growth rate of the nucleus past the barrier state. The multi-particle scenarios can appear when the escape rate is large. Hence, the midrange of the supercoolings.

In the future results of this publication will be compared to the results of direct numerical simulations of the GL system described by Eqs.(1-5). To verify the MPP hypothesis we will trace the barrier state back 'into oblivion' and compare its evolution to the most dangerous, Goldstone, and distorting modes.

Table of crystallization constants of different substances

Quantity /Units	T_E 10^{+3}K	L 10^{+9}J/m^3	σ J/m^2	l 10^{-10}m	γ 10^{+3}m^3/Js	$a=6\sigma/l$ 10^{+9}J/m^3	$\kappa=6\sigma l$ 10^{-10}J/m	$T_F=al^3/k_B$ 10^{+3}K	$l_C=\sigma/L$ 10^{-10}m	$(k_BT_E/\sigma)^{1/2}=l_F$ 10^{-10}m	$\tau=(\gamma a)^{-1}$ 10^{-14}s	$E_E=\sigma/6L$	$S_E=T_E/T_F$
Aluminum	0.9335	1.04	1.15	0.5	2.96	2.76	1.73	3.12	1.11	3.35	6.08	0.441	0.299
Copper	1.3580	1.73	1.280	0.65	1.96	1.02	2.77	3.31	1.62	2.59	5.00	0.984	0.410
Nickel	1.7280	2.35	1.370	0.25	1.96	7.8	2.78	2.51	1.57	2.54	2.87	1.26	0.688
Carbon-Graphite	3.750	22.	0.66						0.755	1.77			

II.2 Appendix: Sharp Interface Approximation

Derivation of the escape time in the small-driving-force regime can be simplified and generalized if one agrees to sacrifice the contribution of the Goldstone mode. Indeed, as known [6, 11, 12], if the driving force is much smaller than the barrier height

$$|[g]| \ll g(\eta_t, 0) - g(\eta_\alpha, 0) \qquad \text{(A1)}$$

a thin layer, called *interface*, develops in the system where the OP field changes quickly while in the rest of the system it changes slowly (sharp-interface or drumhead approximation). Then, instead of the Cartesian coordinate system **x**=(x, y, z), one can introduce new time-dependent curvilinear coordinates {u=u(**x**, t), p=p(**x**, t), q=q(**x**, t)} such that the OP is a function of one coordinate *only:* η=η(u). In the curvilinear system the coordinates (u, p, q) separate and STDGLE (4) transforms into the following equation

$$\gamma\kappa\frac{d^2\eta}{du^2}+(V_n+2\gamma\kappa K)\frac{d\eta}{du}-\gamma\frac{\partial g}{\partial\eta}+\xi=0 \qquad \text{(A2)}$$

where the normal velocity V_n and the mean curvature K of the interface depend on (p, q, t), and ξ depends on (u, p, q, t). Then we multiply the left-hand side of Eq.(A2) by dη/du and integrate it over the thickness of the layer that is, from u_β to u_α. Taking into account that in this approximation $\eta(u_\alpha)=\eta_\alpha$ and $\eta(u_\beta)=\eta_\beta$, we obtain an equation

$$(V_n+2\gamma\kappa K)\int_{u_\beta}^{u_\alpha}\left(\frac{d\eta}{du}\right)^2 du+\gamma[g]+\varphi=0 \qquad \text{(A3)}$$

where the integral is proportional to the interfacial energy σ, Eq.(49), and the stochastic force φ is defined as follows:

$$\varphi(p,q,t)\equiv\int_{u_\beta}^{u_\alpha}\xi(u,p,q,t)\frac{d\eta}{du}du \qquad \text{(A4)}$$

Obviously, the new force has zero mean. To evaluate its strength we write the autocorrelation function:

$$\langle\varphi(p,q,t)\varphi(p',q',t')\rangle=2\gamma\frac{\sigma}{\kappa}k_BT\delta(p-p')\delta(q-q')\delta(t-t') \qquad \text{(A4a)}$$

where we used Eqs.(4b, 49) and one integration over u was removed by the δ-function. Then, from Eq.(A3) we obtain the sharp-interface approximation of the STDGLE (4):

$$V_n=\gamma\kappa\left(\frac{|[g]|}{\sigma}-2K\right)-\frac{\kappa}{\sigma}\varphi \qquad \text{(A5)}$$

which can be applied to many interesting problems of interface motion.

The MPP of the sharp-interface approximation consists of spherically symmetric particles (nuclei) of the new phase β surrounded by the transition layer in the shape of a sphere because in anisotropic systems a sphere provides minimum surface for the same enclosed volume. Hence, the spherical shape provides minimum free energy excess G that is, maximum probability, Eq.(5), for the nuclei of the same volume. Then, in order to use Eq.(A5) on the MPP we rewrite it for the radius of the nucleus R(t):

$$V_n=\frac{dR(t)}{dt},\ K=\frac{1}{R(t)}\ \ on\ S_R \qquad \text{(A6)}$$

where S_R is the surface of the surrounding sphere. To eliminate superfluous dependence of the stochastic force φ on the surface coordinates (p, q) in the spherically symmetric case we average the force, Eq.(A4), over the surface of the sphere taking into account that $\int_{S_R}dp\,dq=4\pi R^2$. Then Eq.(A5) turns into

$$\frac{dR}{dt}=2\gamma\kappa\left(\frac{1}{R_C}-\frac{1}{R}\right)-\frac{\kappa}{4\pi R^2\sigma}\zeta_R(t) \qquad \text{(A7)}$$

where

$$R_C=\frac{2\sigma}{|[g]|} \qquad \text{(A7a)}$$

is the radius of the critical nucleus and the stochastic force on the particle's radius is

$$\zeta_R(t)\equiv\int_{S_R}\varphi(p,q,t)dp\,dq\,; \qquad \text{(A8)}$$

$$\langle \zeta_R(t)\zeta_R(t')\rangle = 8\pi R^2\gamma\frac{\sigma}{\kappa}k_BT\,\delta(t-t') \qquad \text{(A8a)}$$

Compare the stochastic forces ζ_R, Eqs.(A8), and ζ_v, Eq.(15), which are averages of the internal fluctuations $\xi(\mathbf{x}, t)$ over the entire volume of the system V, and notice the difference in the dependence of their strengths on the volume V. This is a result of the weight factor $d\eta/du$, which was used for the former. By using the random variable R(t), Eq.(A6), to uniquely describe the state of the whole system we eliminated the distorting modes of the nuclei. By reducing Eq.(A5) to Eq.(A7) we eliminated the center of the nucleus as an independent variable and pinned it down at its center. This eliminates the Goldstone modes responsible for the translation invariance of the system.

Hence, R(t) describes the system on the MPP without the Goldstone modes and, in principle, Eq.(A7) (or an equation for the volumetric content $4\pi R^3/3$) can be used to derive an expression for the escape time. The problem is that this equation creates the so-called Ito-Stratonovich dilemma for the Langevin equation with the multiplicative stochastic force that is, dependent on the random variable itself [9, 15]. In order to eliminate the dilemma we introduce the new MPP variable—area of the nucleus' surface S_R:

$$s = 4\pi R^2 \qquad \text{(A9)}$$

and derive a Langevin equation for it. For this we multiply all terms of Eq.(A7) by $8\pi R$ and renormalize the stochastic force:

$$\zeta_s(t) \equiv -\frac{2\kappa}{R\sigma}\zeta_R(t), \qquad \text{(A10)}$$

$$\langle \zeta_s(t)\zeta_s(t')\rangle = \Gamma_s\,\delta(t-t'), \quad \Gamma_s = 32\pi\frac{\kappa}{\sigma}\gamma k_BT \qquad \text{(A10a)}$$

Then the Langevin equation for s takes the form:

$$\frac{ds}{dt} = 16\pi\gamma\kappa\left(\frac{\sqrt{s}}{\sqrt{s_C}} - 1\right) + \zeta_s(t) \qquad \text{(A11)}$$

where s_C is the surface area of the critical nucleus. This equation describes 'random walk' of the variable v=s in the potential field

$$U(s) = 16\pi\gamma\kappa\left(s - \frac{2}{3\sqrt{s_C}}s^{3/2}\right), \quad 0 \le s \le s_\beta \qquad \text{(A12)}$$

with an infinitely high 'walls' erected at s_α=0 and $s=s_\beta$ in order to terminate disappearance of the nuclei and unlimited growth past certain size of the nucleus (precise value of s_β does not matter for as long as $s_\beta > s_C$). The potential (A12) with the two walls has two minima at 0 and s_β and a maximum at s_C; hence, this is a non-smooth bistable potential (see Figure 1a) and the surface of the critical nucleus plays the role of the barrier state. Then, substituting (11b) into (10) using the potential (A12) and the noise intensity from Eq.(A10a) and then using Eqs.(33, 49) we obtain:

$$\tau_s^s = \frac{1}{8\gamma\kappa}\sqrt{\frac{k_BTs_{CN}}{\pi\sigma}}\,e^{\frac{\sigma s_{CN}}{3k_BT}} = \frac{\sqrt{k_BT\sigma}}{2\gamma\kappa\,|[g]|}e^{\frac{16\pi\sigma^3}{3k_BT\,[g]^2}} = \tau\frac{\sqrt{6\vartheta}}{2\Delta}e^{\frac{8\pi}{9\vartheta\,\Delta^2}} \qquad \text{(A13)}$$

References to PART II.2

1. J. W. Christian, "The Theory of Phase Transformations in Metals and Alloys" (Pergamon, Oxford, 1965), p. 418.

2. R. W. Balluffi, S. M. Allen, W. C. Carter, "Kinetics of Materials" (Wiley, Hoboken, NJ, 2005), p. 459.

3. J. S. Langer, Ann. Phys. **41**, 108-157 (1967); ibid **54**, 258-275 (1969).
4. C. Unger and W. Klein, Phys. Rev. B **29**, 2698 (1984).
5. M. Buttiker and R. Landauer, Phys. Rev. A **23**, 1397 (1981).
6. A. Z. Patashinskii and B. I. Shumilo, Sov. Phys. JETP **50**, 712-719 (1979).
7. H. Tomita and S. Miyashita, Phys. Rev. B **46**, 8886 (1992).
8. H. A. Kramers, Physica (Utrecht), **7**, 284 (1940); P. Hanggi, P. Talkner, M. Borkovec, Rev. Mod. Phys. **62**, 251 (1990).
9. N. G. van Kampen, "Stochastic Processes in Physics and Chemistry" (Elsevier, Amsterdam, 1981).
10. B. N. Belintsev, M. A. Livshits, and M. V. Volkenstein, Z. Physik B, **30**, 211-218 (1978).
11. J. D. Gunton and M. Droz, "Introductions to the Theory of Metastable and Unstable States" (Springer-Verlag, Berlin 1983), p. 84.
12. A. Umantsev, J. Chem. Phys. **116** (10**)**, 4252-4265 (2002).
13. In condition (9) a weak inequality may be used because it affects the exponential in Eq.(3).
14. F. W. J. Olver, "Introduction to Asymptotics and Special Functions" (Academic Press, NY-London, 1974).
15. J. Garcia-Ojalvo and J. M. Sancho, "Noise in Spatially Extended Systems" (Springer-Verlag, New York, 1999).
16. I .M. Gelfand and S. V. Fomin, "Calculus of Variations" (Prentice-Hall, New York, 1963).; P. M. Morse H. Feshbach, "Methods of Theoretical Physics" (McGraw-Hill, New York, 1953)
17. A. Umantsev and G. B. Olson, Phys. Rev. E **48**, 4229 (1993) and other 1D papers.
18. M. A. Neimark, "Linear Differential Operators" (Gos. Pub. Tech-Theor Literature, Moscow, 1954) (in Russian)
19. R. S. Maier and D. L. Stein, Phys. Rev. Let. **87**, 270601 (2001); E. Vanden-Eijnden and M. G. Westdickenberg, J. Stat. Phys. **131**, 1023-1038 (2008).
20. C. B. Muratov and E. Vanden-Eijnden, J. Stat. Phys. **114**, 605 (2004); C. V. Coffman, Arch. Rat. Mech. Anal., **46**, 81 (1972); H. Berestycki and P.-L. Lions, Arch. Rat. Mech. Anal., **82**, 313 (1983); Loss and Leib, "Analysis".
21. G. Barton, A. J. Bray, and A. J. McKane, Am. J. Phys., **58**, 71 (1990).
22. L. S. Schulman, "Techniques and Applications of Path Integration" (J. Wiley, New York, 1981), Chapter 29.

II.3 COMPUTER SIMULATIONS

The above described theoretical model, Eqs.(1, 3, 4, 31), was scaled, discretized, and converted into a computer model for the numerical simulations. Results of the simulations of evolution of the isothermal system with moderated driving force are presented in Figure 3.1.

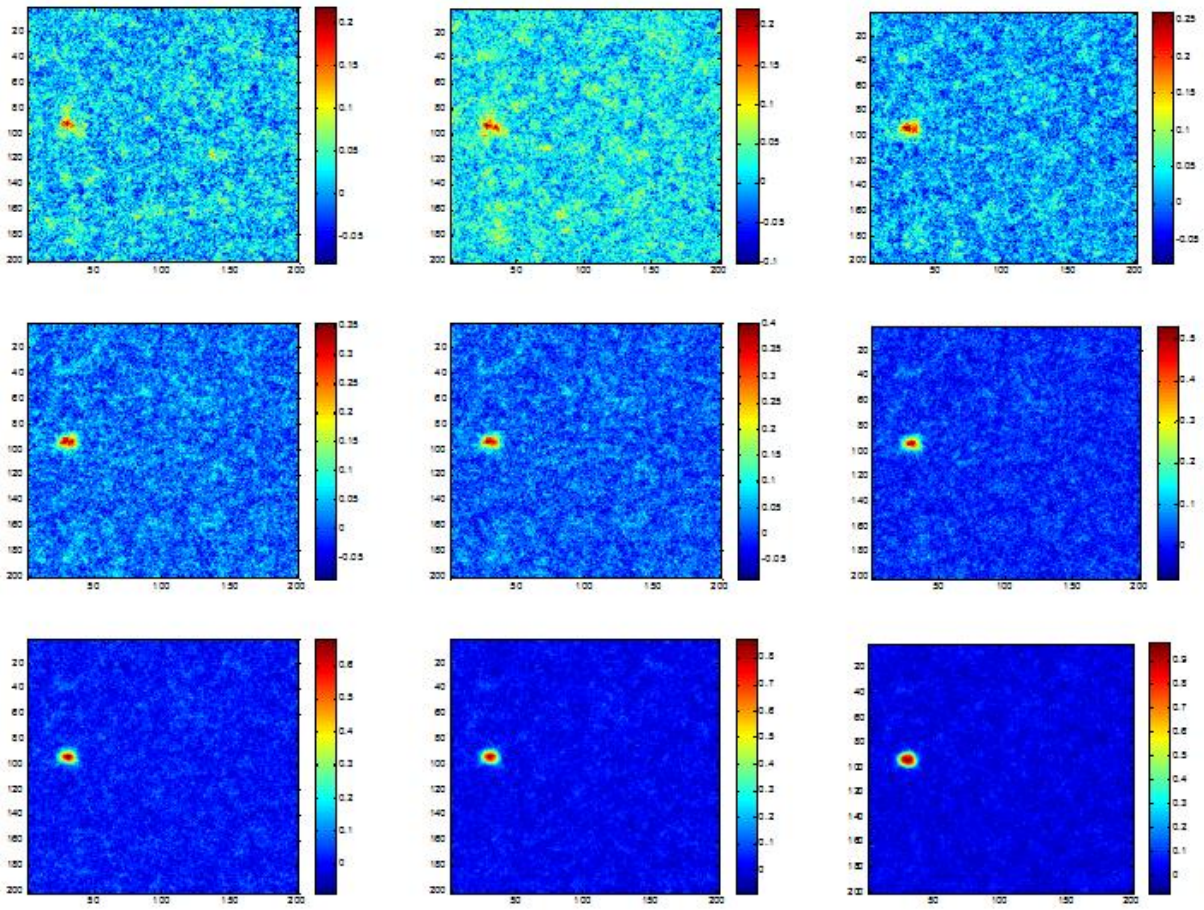

Fig. 3.1. Evolution of the isothermal system with a nucleus.

In Figure 3.2, the structures of the incipient nucleus in X- and Y- directions are presented.

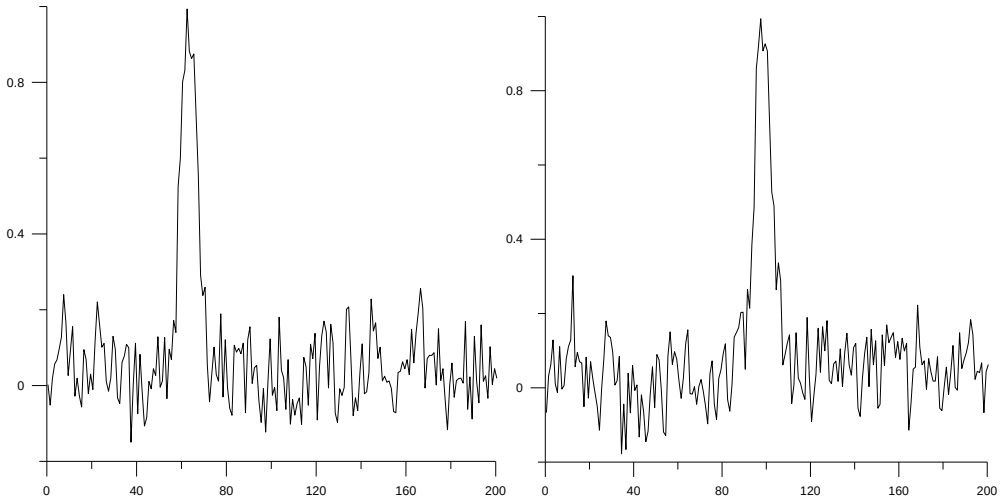

Fig. 3.2. Structure of the nucleus in X- and Y- directions.

Analysis of the simulations in the 2D system is currently underway.

Recommendations to Further Research

1. Reduction of the size of FIB-written carbon nanostructures

Now it is clear that the size of the carbon nanostructures is the major parameter determining their phase content and electronic properties. With the available FIB instrument we can reproducibly attain a 30 nm size. Occasionaly the size can be attained as small as 10 nm. This value, however, has been not measured directly but deduced from the electrical measurements of the nanodot chain structures. We believe that the carbon nanostructures made on diamond surface with an ion beam of a 10 nm diameter would posses much more pronounced nonlinear behavior. In particular the coulomb blockade is expected to be the main effect controlling charge carrier flow in the nanowire-nanodot structures even at room temperature. As such, with a 10 nm ion beam it will be possible to make in a reproducible way single electron devices (e.g. single electron transistors) operating at room temperature. Also our measurements reveal that carbon nanodot structures can operate as chemical sensors, which can outperform those made of nanowire. Thus the reduction of size of sensitive elements is a way to improve the sensor performance. We expect that the nanodot structures working in a coulomb blockade regime would possess very high chemical sensitivity.

2. Amorphous carbon nanofilms on diamond surface

Experiment. Conductive carbon nanofilms on diamond surface have been proved to be very promising for chemical sensor applications. If these films are grown at appropriate temperature-pressure conditions and treated in appropriate plasma, they exhibit considerable change in electrical conductance when exposed to gases and vapors of solvents. It is important that this response is quantitatively and qualitatively different for different chemical analytes. Thus carbon nanofilms on diamond may be used for development of selective chemical sensors. The combination of sensing amorphous carbon film and diamond substrate is unique in terms of development of all-carbon sensors, which could be of particular interest for biological and medical applications. However, in order to achieve maximum performance of the carbon-diamond sensors, the mechanisms of formation carbon nanofilm of diamond surface at high temperature in different atmospheres must be systematically studied. We assume that the increase of the growth temperature over 1600C may result in formation of high quality carbon films, atomic structure of which will be that of graphene, and the electronic properties of such films will superior to those of the carbon films grown at a conventional temperature of 1200C. In order to perform the growth of carbon nanofilms on diamond surface at very high temperatures in different atmospheres, we have to considerably redesign the existing graphite furnace and perform systematic studies of the temperature-induced graphitization of different crystallographic planes of diamond.

Theory. We plan to develop a theory of the thermally activated graphitization of the diamond substrates. Our hypothesis is that this process causes growth of the conductive nanofilms on the diamond surfaces. This theory will be based on the continuum theory of carbon phases, which was developed earlier as a part of the present project. We will use the data on the transformation barrier heights that were obtained in the theory. The new significant element of the theory will be inclusion of the kinetics of the thermally activated process into the model. The continuum theory provides a solid framework for that. We also are planning to include effects of stress that develops in the nanofilm during growth. We are planning to explain the rate of growth of the films at different temperatures and more complicated heating-cooling cycles. We will also try to analyze the changes in the charge hopping mechanism of conductivity.

3. Growth of graphene on insulating substrates

Experiment. In term of practical applications, development of the direct method of growing uniform graphene films on quartz is the most important result of the finished project. This project has potential to be transformative in the field of carbon nanoelectronics. Although so far we have demonstrated growth of a few millimeter thick uniform graphene films on small substrates, there are no limitations preventing application of this method to substrates of any size. We are confident that we will be able to demonstrate in the nearest future the growth of uniform single layer graphene on large-area quartz wafers. Besides, we plan to perform systematic studies of the direct growth of graphene films on sapphire and silicon substrates and to attempt to fabricate silicon-graphene heterostructures. Also, we are going to focus our research on the growth of graphene films at lower temperatures, which could be as low as 600C. The purpose of the development of the method of low-temperature growth is to make the graphene growth technology compatible with the existing silicon device technology.

Theory. The purpose of this project will be developing theory and conducting computer simulations of the 2-dimensional process of nucleation and growth of the islands of graphene on different substrates. We will capitalize on our experience with the 3-dimensional systems in the last leg of the finished project and develop a theoretical/computational model that includes properties of the carbon phases into the nucleation process. The Kosterlit/Thouless effect will be an important part of the model. Results of the modeling will help experimenters to grow more uniform graphene films of greater fidelity.